University of California
Santa Barbara

Dimensionality in dipolar quantum systems

A dissertation submitted in partial satisfaction
of the requirements for the degree

Doctor of Philosophy
in
Physics

by

Simon Alexander Meynell

Committee in charge:

Professor Ania C. Bleszynski Jayich, Chair
Professor Andrea Young
Professor Leon Balents

December 2023

The Dissertation of Simon Alexander Meynell is approved.

Professor Andrea Young

Professor Leon Balents

Professor Ania C. Bleszynski Jayich, Committee Chair

December 2023

Dimensionality in dipolar quantum systems

by

Simon Alexander Meynell

To those who keep asking the hard questions

Acknowledgements

All graduate students must eventually face the impossible task of adequately thanking the many people who have contributed to the success of their Ph.D. I now, too, face this impossible task. Though, in the slim pages of a thesis acknowledgments section, I may not be able to hope to properly thank the people I've met over the course of this degree, I do hope to enjoy many future years of friendship and fruitful discussions with the colleagues I've found here.

Firstly and foremost, I want to thank Ania for acting as such an amazing advisor over the past six years. I'll look back very fondly on the many times I've wandered into Ania's office with some crazy idea or another, and (despite the oft infeasibility of these ideas) she's entertained them anyway. Our discussions are always so much fun and intellectually fruitful for me. Truly, I can say with certainty that discussing physics with Ania has been the highlight of my professional career. I love the breadth of Ania's interests - I feel just as at home discussing history, world events, or art as I do discussing physics with Ania. I very much admire her ability to remain ever-solution-oriented, pragmatic, and efficient at all stages throughout a project or experiment. Perhaps most of all, I admire her dedication to truly understanding the basics of a problem at every stage in the scientific process. I can't count the number of times when we would be in the midst of a discussion amongst a roomful of people (all of whom think they understand the topic at hand), and then Ania would ask some foundational question that revealed we had been very much lost all along. Then, with the assistance of Ania, we'd all be brought back to the discussion now on much firmer footing. I think it is Ania's commitment to a deep understanding of physics that allows her to see these gaps in understanding where all others have missed them. Any future students reading this would be very wise to follow Ania's example here and build their understanding of physics on a rocky foundation.

Ania, your mentorship has been of incalculable value to me. When I think back to where I was at the start of my Ph.D. and reflect upon the growth afforded to me by your guidance, I am so grateful. I hope to have many exciting discussions with you about physics (and anything else) in the years to come.

I've been lucky enough to enjoy several wonderful mentors over the course of my Ph.D. I had the pleasure of working with Paz extensively over two years in pursuit of the scanning experiments. I was very fortunate to learn much about NV centers and solid-state qubit manipulation from him, and I greatly enjoyed his company. His ability to take a new idea and get it up and running in only a few hours was truly remarkable. I'm certain I'll make extensive use of what he taught me about optics, quantum systems, and experimental science in any scientific endeavors to come. Whenever I align an optical system in the future, I am certain that it will be Paz and the lesson he taught that will pop into my mind. Claire acted as a warm and insightful graduate student mentor in my early years in Ania's lab. While she taught me all the basics of NVs and CVD growth, she also showed me the ropes in navigating the lab. She made me feel welcomed into the group, and her integrity and commitment to good science were a fantastic influence. Alec and Susanne were also essential to my integration into the group during my early days. Their hard work, guidance in scanning measurements, and patience with me as I learned lessons (often the hard way) were amazing. I feel it was a real treat that I had the opportunity to learn from them. Maxime was another great person from whom I had the chance to learn. His skill with optical systems, I think, was unparalleled throughout my time here. I remember during the depths of COVID, Maxime would always make time to pop in and say hi as I was assembling LTSPM2, and I think there were probably months during COVID when he was the only person I talked to in the US - for this, I'll be forever grateful.

I've received much in the way of useful advice from a number of professors during my

time here. Learning from Kunal Mukherjee has been great. His expertise in everything to do with crystal growth and his ability to (nearly instantaneously) find the solution to a materials problem is astounding. I think our knowledge and understanding of diamond as material would be well-behind where it is now without his input. I think our collaboration with Kunal is phenomenally valuable. Norman Yao is certainly another of my favorite collaborators. His approach to science is wonderfully exciting, and it's always so much fun when I get to listen to Norm explain a concept. I owe my current love of many-body quantum physics to Norm and his generosity in including me in his weekly group meeting. Dan Gianola is another professor with whom I've greatly enjoyed working. Discussing magnetism with him and problems in the field of magnetic materials was a lot of fun - I certainly wish I'd had more opportunities. David Weld is another great UCSB professor from whom I always find myself learning a great deal whenever I have the chance to hear him explain a topic in quantum mechanics. I often find myself wanting to sit in and eavesdrop whenever I see him teaching a class or explaining a topic.

My committee members, Andrea Young and Leon Balents, have also been fantastic sources for discussion. I recall spending many hours with Andrea working on the monolayer graphene paper (which is, perhaps, my favorite project I've worked on). While I've certainly learned much in the way of condensed matter physics from Andrea, the methods for figure generation that he taught me over the course of working on that paper has been one of the most often used pieces of knowledge over my Ph.D. - I think my current figure workflow is almost entirely what I learned from Andrea in his office while working on that paper. Leon Balents was a great sounding board for many ideas in my skyrmion work over my Ph.D. His input was no doubt important in ensuring a reasonable theoretical underpinning for the Lorentz TEM paper. I want to thank them both for serving on my committee and especially for being so flexible with my very late-in-the-quarter date for a defense.

While I've found many excellent colleagues at UCSB, Shreyas and Lillian are undoubtedly two of my favorite people to work with. If Shreyas begins to tackle a problem, one can be sure that in a short time, he will have a remarkably keen insight into virtually every aspect of that problem. I think both when it comes to experimental technical skill in understanding an experiment and when it comes to theoretical insight into the underlying physics of an NV experiment in our lab, there aren't many other people I'd rather ask for help. I must admit that the aspect of graduate school I will miss the most is wandering over the Coral Tree Cafe with Shreyas to talk in-depth about some subtle nuance in NV physics. When I first began showing the ropes of CVD diamond growth to Lillian, it became clear almost immediately that her knowledge of growth and diamond materials science, in general, had quickly surpassed my own. There is no person I know of who has a greater (or deeper) understanding of the often intensely difficult material science questions surrounding diamond materials for quantum purposes. These days, I think every single talk coming out of Ania's group will include Lillian's name somewhere in the acknowledgments - a fact that speaks both the breadth of her interests as well as her intense competence across an apparently boundless set of systems and tasks. I do not doubt that both Shreyas and Lillian will find great success in whatever tasks they undertake in the future, and I look forward to seeing where they go.

While low-temperature scanning is not featured in this thesis, work on low-temperature scanning NV systems has comprised roughly two-thirds of my time at UCSB, so I make a special acknowledgment to that team. Daipeng, who now leads the scanning effort, has shown an exceptional amount of resilience and determination throughout his time at UCSB. He is extremely technically skilled and possesses the enviable quality of being able to keep trying at a problem until he inevitably solves it, no matter how difficult or challenging the problem is. Jeff and Sunghoon, being the newer generation of NV scanning scientists, will soon find themselves leading the effort in the group. I have no

doubt that they'll see a great amount of success. Jeff displays a sharp and often incisive insight into a wide array of physics - often quickly arriving at a correct conclusion that takes me many times longer to reach. In addition to theoretical sharpness, Jeff's skill at machining, building, and the nuts-and-bolts side of experimental physics is unmatched. Sunghoon is diligent and kind and possesses a huge array of knowledge about nearly every topic. Like Ania, Sunghoon is great at always having a sure foundation upon which to build his knowledge, and I find that whenever Sunghoon says something is true, you can bet nearly 100% of the time that it is certainly true. Being the newest member of the team, I have not had a great deal of time to work with Aaron. Nevertheless, even in that short time, he has made a great impression, already improved many aspects of the system, and made tremendous progress. I feel I can rest easy knowing the scanning experiments are in such capable hands, and I look forward to witnessing the exciting assortment of work that will undoubtedly come from this team.

The new many-body thrust in Ania's lab that has begun over the past year or so is quite dear to my heart (and does feature heavily in this thesis). Haopu, being perhaps the founding member of this thrust, was an undergraduate student whom I had the great pleasure of mentoring. I was constantly amazed by Haopu's experimental ability and the speed at which he was able to get things up and running, as well as his good cheer and enthusiasm for science. I'm very excited to see where his career takes him. Jason is a newer student but, like Aaron, has already made exceptional progress in the group and in understanding physics, which has taken me years to comprehend. I admire the theoretical depth to which he seeks to understand our problems and the way in which he is fully capable of diving into every corner of the difficult theoretical topics that underpin many-body physics - I anticipate that he will find a huge amount of success in solving problems in many-body physics. Taylor and Zhiran (who also lead their own separate thrust) bring a wealth of information and technical knowledge to the many-body team. Zhiran, who

joined at the same time as me (and so I think I share a resulting kinship with), is one of my favorite people to discuss physics with. Taylor deserves special recognition for tackling an exceptionally challenging problem at one of the most inconvenient times in history (COVID-19). The fact that Taylor managed to construct one of the best confocal systems in the group while learning everything about NV operation under conditions of extreme isolation due to COVID-19 is mind-blowing (and, to boot, he managed to make that system low-temperature).

While the spin-phonon subgroup is certainly the one I've interacted with the least, that is only due to bandwidth limitations on my part, and I wish that I had had more time to become involved with this team. I always enjoy my discussions with Viraj about physics - he has a keen desire to understand the essential mechanisms of the system he is working with, which is the hallmark of a good scientist. While most of my discussions with Carl have probably revolved around safety inspection logistical issues, I very much wish I had talked more with him about physics. Carl is great at explaining concepts clearly and is one of those scientists whose statements I implicitly trust. Certainly, if I could have, I would have liked to have spent many hours with Viraj and Carl in the cleanroom, learning about dilution refrigeration and the exciting experiments they are planning. Hyunseok is exceptionally adept at all things to do with fabrication, and he can work miracles in the cleanroom (or in 4207) using remarkably little, a fact which, I think, shows his resourcefulness. Though I'll miss his upcoming wedding to Eunseo, I wish them both all the best in their many exciting coming years. Perhaps my biggest regret in my Ph.D. is that I did not get more time to work with Jaya. Though she's just joined, she has already become an essential part of the lab and offers a combination of common-sense input and profound theoretical insight into every problem she's tackled. Jaya displays intense independent leadership and direction, qualities that can be extremely rare, and I hope to one day read about a Jaya Venkatraman Research Group in the papers.

One of the great joys of working at UCSB is the excellent undergraduate student researchers. This school is full of hardworking, intelligent undergrads who constantly impress me with their abilities. Haopu, whom I've already discussed earlier in the acknowledgments, joined the group late in his undergraduate work but profoundly impacted the group in only a short time. He refined our XRD methods and developed (and built) an ultra-high-resolution microscope. He's independent, self-motivated, intelligent, and always willing to roll up his sleeves and put in the hard work required for good science. Chang is another undergraduate student who I greatly enjoyed working with. I found him always willing to engage in lengthy theoretical discussions, and I fondly remember one day when we sat down in the office and went through and carefully derived together on the board the result for a many-body dynamics problem in a paper we were writing. As I come to the end of my degree, I find it is this type of memory that I most cherish. Yuanqi is another example of an exceptional undergraduate student at UCSB. His skill at theoretical physics was unparalleled and his improvements to the software architecture in our experiments is one of the most valuable changes I've seen during my time in this group. The pulse sequence visualizer in particular, is so great that I struggle to understand how we were able to function before its implementation. Katya is another phenomenal undergraduate student who displays an impressive work ethic. Nearly any time of day or night, I can be sure to find her working away in PSB doing NV measurements, and I think this diligence has resulted in her now being the most knowledgeable member of the group for the Cage and RTQI setups. Though we overlapped for only a year, I think it is hard to overstate the importance of Dolev's impact on the group. His incredible success has been awe-inspiring to witness and I am very glad that I got to discuss physics with Dolev over that year. Keqin is an undergrad who joined over the summer and displayed an amazing amount of competence and progress in such a short time - my only complaint is that I wish we could have kept her in the group longer.

My family is, without a doubt, the reason I am in physics to begin with. My mother's love of analysis, logic, and mathematics pushed me toward the sciences, and it was her very good advice that persuaded me to try a class in physics. My father's love of knowledge and learning is undoubtedly a major part of why I decided to pursue graduate school, and his love of systems and mechanics which he conveyed to me at an early age, is something I see echoed every day in my physics work. My aunt Letitia and my uncle Andrew inspired in me a love of academia by conveying at an early age that there is something uniquely noble about the pursuit of knowledge for knowledge's sake - a pursuit that only the academy allows. My brother has shown perseverance in the face of many overwhelming trials, is always seeking new and unique ways to understand the world, and always tries to understand perspectives that are very different than his own - these are all attributes that I greatly admire and seek to emulate in myself.

Finally, I wish to thank Ania again. While I thanked her at the start of this section for being such an incredible advisor, I wish to now thank her for being an incredible friend. Ania and Andrew showed me exceptional kindness during one of my life's bleakest and most difficult moments. While this moment shook me, with their help, I eventually got back on my feet. Without Ania's kind intervention, I am doubtful that any part of this document would have been written. And so, it is in many more ways than one that I thank Ania for the fact that today I am submitting my thesis.

Curriculum Vitæ

Simon Alexander Meynell

Education

2023	Ph.D. in Physics (Expected), University of California, Santa Barbara.
2017	M.Sc. in Physics, Dalhousie University.
2015	B.Sc in Physics, University of King's College.

Publications

S. A. Meynell*[1], W. K. Schenken*, F. Machado, B. Ye, C. A. McLellan, M. Joos, V. V. Dobrovitski, N. Y. Yao, A. C. B. Jayich. Long-lived coherences in strongly interacting spin ensembles. arXiv:2309.15444 [quant-ph] (2023)

L. V. H. Rodgers, S. T. Nguyen, J. H. Cox, K. Zervas, Z. Yuan, S. Sangtawesin, A. Stacey, Ch. Jaye, C. Weiland, A. Pershin, A. Gali, L. Thomsen, **S. A. Meynell**, L. B. Hughes, A. C. Bleszynski Jayich, X. Gui, R. J. Cava, R. R. Knowles, N. P. de Leon. Diamond Surface Functionalization via Visible Light-Driven C-H Activation for Nanoscale Quantum Sensing. arXiv:2309.07354 [cond-mat.mtrl-sci] (2023)

S. A. Meynell*, Y. M. Eggeler*, J. D. Bocarsly, D. A. Kitchaev, B. E. Rhodes, T. M. Pollock, S. D. Wilson, A. Van der Ven, R. Seshadri, M. De Graef, A. B. Jayich, and D. S. Gianola. Inducing skyrmion flop transitions in $Co_8Zn_8Mn_4$ at room temperature. Phys. Rev. Materials **7**, 044401 (2023)

L. B. Hughes, Z. Zhang, C. Jin, **S. A. Meynell**, B. Ye, W. Wu, Z. Wang, E. J. Davis, T. E. Mates, N. Y. Yao, K. Mukherjee, and A. C. B. Jayich. Two-dimensional spin systems in PECVD-grown diamond with tunable density and long coherence for enhanced quantum sensing and simulation. APL Mater. **11**, 021101 (2023)

E. J. Davis, B. Ye, F. Machado, **S. A. Meynell**, T. Mittiga, W. Schenken, M. Joos, B. Kobrin, Y. Lyu, D. Bluvstein, S. Choi, C. Zu, A. C. Bleszynski Jayich, N. Y. Yao. Probing many-body noise in a strongly interacting two-dimensional dipolar spin system. Nature Physics **19**, 836–844 (2023)

A. Jenkins, S. Baumann, H. Zhou, **S. A. Meynell**, D. Yang, K. Watanabe, T. Taniguchi, A. Lucas, A. F. Young, and A. C. Bleszynski Jayich. Imaging the breakdown of ohmic

[1] * represents equal contribution

transport in graphene. Phys. Rev. Lett. **129**, 087701 (2022)

S. A. Meynell, C. A. McLellan, L. B. Hughes, W. Wang, T. E. Mates, K. Mukherjee, and A. C. Bleszynski Jayich. Engineering quantum-coherent defects: The role of substrate miscut in chemical vapor deposition diamond growth. Appl. Phys. Lett. **117**, 194001 (2020)

J. M. Smith, **S. A. Meynell**, A. C. Bleszynski Jayich, and J. Meijer. Colour centre generation in diamond for quantum technologies. Nanophotonics **8**-11, (2019)

S. A. Meynell, M. N. Wilson, K. L. Krycka, B. J. Kirby, H. Fritzsche, and T. L. Monchesky. Neutron study of in-plane skyrmions in MnSi thin films. Phys. Rev. B **94**, 054402. (2017)

S. A. Meynell, A. Spitzig, B. Edwards, M. D. Robertson, D. Kalliecharan, L. Kreplak, and T. L. Monchesky. Structure of MnSi on SiC(0001). Phys. Rev. B **94**, 184416. (2016)

S. A. Meynell, M. N. Wilson, J. C. Loudon, A. Spitzig, F. N. Rybakov, and T. L. Monchesky. Probing chiral magnetic thin films with Hall effect measurements and transmission electron microscopy. Phys. Rev. B **90**, 224419. (2014)

S. A. Meynell, M. N. Wilson, H. Frietzsche, A. N. Bogdanov, and T. L. Monchesky. Surface twist instabilities and skyrmion states in chiral ferromagnets. Phys. Rev. B **90**, 014406. (2014)

M. N. Wilson, E. A. Karhu, D. P. Lake, A. S. Quigley, **S. Meynell**, A. N. Bogdanov, H. Fritzsche, U. K. Rößler, and T. L. Monchesky. Discrete helicoidal states in chiral magnetic thin films. Phys. Rev. B **88**, 214420. (2013)

Abstract

Dimensionality in dipolar quantum systems

by

Simon Alexander Meynell

Engineered quantum systems are a powerful tool for quantum sensing and simulating otherwise intractable many-body quantum systems. Defects in the solid-state have emerged as one particularly useful class of platforms for tackling these goals, and the nitrogen-vacancy (NV) center in diamond is an especially noteworthy example owing to its ease of addressability and functionality across a broad range of conditions. However, engineering the system dimensionality and the underlying Hamiltonian is required to achieve good sensitivity and effective simulation. In this thesis, we will discuss systems of disordered interacting spins across three, two, and one dimensions. A special focus will be on methods for engineering these systems, and, especially in Chapters 3 and 4, we will discuss some of the interesting physics one can probe using confinement (in 1 and 2D) and periodic drive (in 3D). The methods of engineering we will explore are primarily chemical vapor deposition (CVD)-based, and we will also discuss the primal role of miscut in determining the quality of CVD growth. For three-dimensional ensembles, we will highlight a new sequence, ϵ-CPMG, and discuss the way in which this sequence can be used to characterize competing interactions in disordered dipolar ensembles. For two-dimensional systems, we will discuss how to generate 2D confinement and the many-body physics one can study using a careful analysis of decoherence profiles. Step bunches and hillocks will be considered as two possible methods for patterning low-dimensional geometries of spins, and, in the case of the step bunch, we will highlight some interesting physics that arises from the patterned one-dimensional structure.

Permission and attributions

Chapter 1: Shreyas Parthasarathy provides the Bloch sphere representations of qubit states. Example data for ODMR, Rabi oscillations, and spin echo decay were taken in collaboration with Haopu Yang, Shreyas Parthasarathy, and Jason Chen.

Chapter 2: Data and figures were previously published in Ref[1]. Permission was obtained from Applied Physics Letters to publish reproductions of these figures in this thesis. MicroSIMS data was taken by Lillian Hughes. The work presented in this chapter is the result of a collaboration between myself, Claire McLellan, Lillian Hughes, Wenbo Wang, Tom Mates, Kunal Mukherjee, and Ania Bleszynski Jayich.

Chapter 3: Data and figures were published in Ref[2]. Data were taken jointly by William Schenken and me. Numerical analysis is the result of work by Francisco Machado. Theoretical analysis is the result of work by myself, William Schenken, Francisco Machado, and Bingtian Ye. The work presented in this chapter is the result of a collaboration between myself, William Schenken, Francisco Machado, Bingtian Ye, Claire McLellan, Maxime Joos, V. V. Dobrovitski, Norman Yao, and Ania Bleszynski Jayich.

Chapter 4: One-dimensional decoherence data were taken jointly by myself, Haopu Yang, Shreyas Parthasarathy, and Jason Chen. GSD measurements were taken by myself, Haopu Yang, and Paz London. NanoSIMS data was taken by Eveline Postelnicu. The tri-layer sample, L043, was grown by Lillian Hughes. The one-dimensional experiments are the result of a collaboration between myself, Haopu Yang, Shreyas Parthasarathy, Jason Chen, Lillian Hughes, Eveline Postelnicu, Paz London, Emily Davis, Bingtian Ye, Francisco Machado, Weijie Wu, Zilin Wang, Kunal Mukherjee, Norman Yao and Ania Bleszynski Jayich. Two-dimensional the-

ory and data are the result of a collaboration between myself, Emily Davis, Bingtian Ye, Francisco Machado, Weijie Wu, Thomas Mittiga, William Schenken, Maxime Joos, Bryce Kobrin, Yuanqi Lyu, Zilin Wang, Dolev Bluvstein, Soonwon Choi, Chong Zu, Ania Bleszynski Jayich and Norman Yao.

Contents

Chapter 1

The nitrogen-vacancy center in diamond

For nearly 80 years, humans have made widespread use of devices whose design principles rely on predictions from quantum mechanics. Some particularly ubiquitous examples from this period include the transistor[3], the laser[4], and the light-emitting diode[5]. However, while this "quantum revolution" has produced a plethora of useful technologies, until very recently, most of these would utilize only "incoherent" quantum mechanics. A second class of quantum devices has emerged over the past two decades: those that seek to exploit coherent state manipulation. This "second quantum revolution"[6] offers fundamentally different types of devices: those that rely on the unusual physics associated with superposition and entanglement, giving rise to applications in chemistry[7, 8, 9, 10], sensing[11, 12, 13, 14, 15, 16, 17], and, famously, computing[18, 19, 20, 21, 22].

Coherence is at the heart of any quantum mechanical experiment utilizing superpositions or entanglement. Often, a qubit or system of qubits is characterized by a coherence time, the timescale over which the phase becomes scrambled. A system prepared in a superposition with a well-known phase will lose that phase over this timescale, which

can be described through statistical correlation functions like $g^{(1)}$, and often measured using a spin echo (or Hahn echo)[23]. Thus, what is usually meant by "quantum coherence" is phase coherence, that is, the extent to which the phase of a state is well-known to the experimenter. Quantum logic gates performed well after this timescale will generally be ineffective and so the total available time for any computational or sensing task by a qubit will be set by this coherence time. Physically, the exact mechanisms for coherence loss are not fully understood but are usually the result of interactions[24], thermalization[25, 26], and entanglement[27][1] with an uncontrolled environment. Despite the great importance[28] of the concept, in formal discussions such as those in textbooks, mentions of coherence are often conspicuously absent or limited to discussions about coherent light[29, 30].

The preservation of coherence and the remarkable strides humans have made over the past two decades in pushing towards ever-longer[31, 32] single-qubit coherence times and ever-larger quantum network sizes[33][2], coupled with remarkable advances in control[18] herald a large impact for the second quantum revolution. While many of the future applications for coherent quantum systems are still nascent, coherent sensing is already witnessing a boom in use cases. This is, in large part, due to many years of nuclear magnetic resonance (NMR) development and the requisite pulse sequence engineering for that development. Quantum sensors include scanning superconducting quantum inference devices (SQUIDs)[11, 13, 17, 34], quantum dots[35], trapped ions[15], Rydberg atom arrays[16], and solid-state defects, notably, the nitrogen-vacancy (NV) center in diamond[36, 37, 38, 39, 14, 40].

The NV center, which is the unifying topic of this thesis, has attracted an explosion of interest in recent years, resulting in at least two commercially available turnkey scanning

[1] These are not really three different sources of decoherence so much as they are different ways of describing the same fundamental mechanisms.

[2] Hour long coherence times and 1000 km channel lengths.

NV systems[41, 42]. While these systems are focused on *ex-situ* sensing[3], this thesis will discuss, primarily, the NV as an *in-situ* sensor. We will investigate the environment of the NVs and the mechanisms that contribute to their decoherence using two primary methods: pulse sequence engineering and dimensional confinement.

1.1 Solid-state defects

Solid-state defects[43] are a class of qubits consisting of a point defect in a larger, crystalline body. Ideally, the crystal provides a quiet[4] environment and the defect acts as a means to localize electronic states whose spin[44, 45], charge[46, 47], nuclear[48, 49], phononic[50, 51], or orbital[52] properties can be read out. Optical addressability is a chiefly desirable feature for any solid-state defect qubit, as well. The ability to interface with photonic degrees of freedom allows for convenient state readout and the possibility of entangling with photons[53] to mediate long-distance entanglement between nodes on a quantum network.

Diamond is an attractive host owing to its exceptionally large band gap (E_G = 5.5 eV)[54] and high Debye temperature (Θ_D = 2240 K)[55], leading to a very quiet environment. Diamond hosts the most well-studied solid-state defect, the nitrogen-vacancy (NV) center in diamond, consisting of a substitutional nitrogen adjacent to a vacancy. However, the NV is only one of many optically fluorescent point defects[5]

[3]That is, sensing an external target. In scanning NV systems, a probe containing an NV center is brought to some system of interest (often, though not necessarily, a condensed matter system of interest) and scanned over the target to form a spatially resolved map of (usually) magnetic fields.

[4]What I mean by quiet is free of fluctuating fields. Because the NV couples to electric, phononic, and magnetic degrees of freedom, we would like free charges, phonons, and fluctuating spins to be kept to as low a density as possible (except in the case of certain types of spins, as we will see later in this thesis, which can be deliberately introduced as a platform for exploring many-body spin physics).

[5]These are commonly referred to as color centers because of their quality of giving diamonds their color. Diamonds with a yellow color are rich in nitrogen[56], blue indicates high levels of boron[57], and pink is usually associated with plastic deformation[58] or (in the case of the very rare Golconda diamonds named from their historical origin of Golconda, India[59]) due to absorption by NV centers[60].

in diamond[61, 62]. Another spin-photon qubit candidate that has garnered significant interest is the silicon-vacancy (SiV) center. The SiV benefits from a strong spin-phonon coupling[63] and, notably in comparison to the NV center, a high probability of emission into the zero-phonon line[64, 65], making it especially well-suited for quantum information tasks. In addition to the SiV, there are the other (less well-studied) group-IV defects[66] such as the tin-vacancy (SnV)[67, 68], the germanium-vacancy (GeV)[69, 70], and the lead-vacancy (PbV)[71, 72]. These other group-IV defects are similar to the SiV but have larger ground state splittings due to the larger sizes of the constituent atom.

Silicon is another promising material for hosting solid-state spin defects that has emerged in recent years[73]. The T-center (Si-T)[74] in particular has attracted a great deal of interest owing to its long coherence times[75] and demonstrated compatibility with silicon-on-insulator chips[76, 74]. In addition to the T-center, the G-center[77, 78] and W-center[79] are also under active investigation. The largest advantage for silicon-based defects is the wealth of resources available for on-chip photonic circuit generation. Silicon fabrication has undergone decades of refinement and integrated photonic circuits have reached a point of maturity - integrating spin defects into a photonic circuit allows for scalable generation[80] of devices for quantum information tasks.

Monolayers of hexagonal boron nitride (hBN) make an unusual host for solid state defects owing to their fundamentally 2D nature. Recently, Gong *et al.*[81] demonstrated coherent manipulation of vacancy-related defects in hBN with coherence times of $\sim$ 70 ns. Carbon-related defects[82] in hBN are also expected to be potentially powerful spin defects, though research into these defects is still in a young state. Silicon carbide (SiC)-based defects[83] offer another route to scalable[84] solid-state qubit networks, but SiC photonic circuits are still in the research phase of development[85, 86], and it will still be many years before industrial foundry production of all-SiC photonic circuits.

1.2 The NV center

That the nitrogen-vacancy (NV) center in diamond is the most well-studied[6] quantum solid-state defect, there can be no doubt[7]. A more interesting question, then, is why? What is it about the NV center that has resulted in it garnering such a colossal amount of interest compared to the other solid-state defects? It is tempting to state that it is simply because so many of the intensely challenging materials challenges have already been worked out. Materials barriers such as optimal creation methods[87, 88, 89, 1, 90], proper surface termination[91, 92], (charge) state dynamics[46, 47, 93], and integration with nanostructures[14, 94, 95] are, if not completely solved, demonstrably surmountable challenges for the NV. However, this answer is sort of kicking the question down the road[8]. So then, is the remarkable success of the NV simply a historical accident? Or is it due to some special features that the NV possesses? I will argue that the prominence of the NV is not because of historical fiat but rather due to two important attributes: ease of generation and ease of measurement[9]. The importance of these two factors is made clear through a brief diversion into the history of the NV center.

Like many impactful discoveries in physics, the study of the NV center has rather humble beginnings. Researchers have studied the defect since at least 1965 when it was first described in the Ph.D. thesis of L. du Preez[96] at University of the Witwatersrand in Johannesburg, South Africa[10]. At this time, the composition of the NV was not

[6] As of writing.

[7] The next leading candidate, the SiV, is probably an order of magnitude less studied. Though certainly not the most reliable metric, a quick search on Google Scholar gives ~ 10000 results for *"NV center" diamond* and only ~ 900 for *"SiV center" diamond*.

[8] Because we can always ask why have these been worked out so early for the NV in contrast to other candidates. This answer is a bit tautological as well - these materials challenges have been overcome *because* the NV is so well-studied.

[9] Long coherence times did not hamper excitement either, though, I think even if NV coherence were limited to 100s of nanoseconds (rather than ms), the NV would still be very popular.

[10] This thesis is not available online and, so far as I can tell, there is only one copy of this document in the world (available only at University of the Witwatersrand). So, to any NV enthusiasts who find themselves in Johannesburg: I think it might be a fun field trip to track down this historical document.

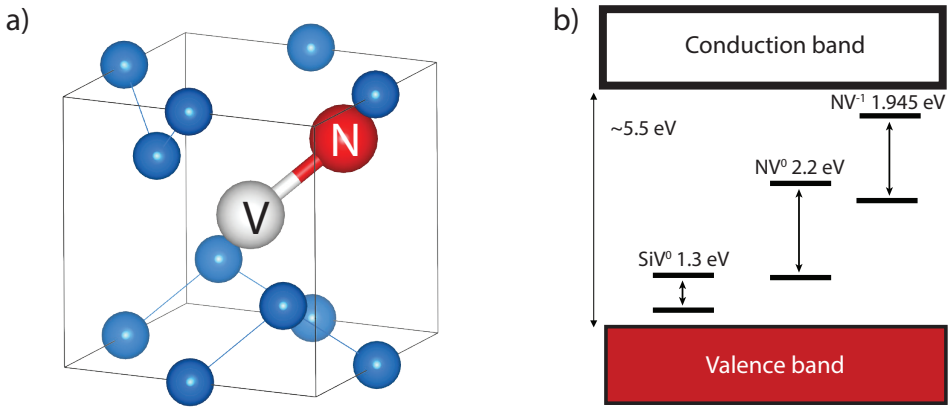

Figure 1.1: a) A ball and stick diagram of the nitrogen-vacancy (NV) center in diamond. The NV consists of a substitutional nitrogen adjacent to a carbon vacancy. b) The location of the NV^- center in the larger band structure of diamond relative to other important defects (see Ref. [101]).

known and the defect was referred to as simply, the 1.945 eV vibronic band in diamond. In his thesis, du Preez had (remarkably) already worked out an optimal method for generating NV centers. The du Preez recipe, which is nearly identical to the one we use at UCSB today, was to find a diamond containing isolated substitutional nitrogen, irradiate the diamond with electrons, and then anneal at temperatures above 900 K. After the discovery by du Preez, the study of this defect was carried out in large part by researchers in the United Kingdom. Clark *et al.*[97] have the first published results building on du Preez's 1965 discovery. These results were followed shortly by substantial progress made by G. Davies *et al.*[98, 99], who, using a clever annealing experiment, stress measurements, and symmetry arguments, quickly identified a single possible candidate for the 1.945 eV vibronic band. The candidate structure that Davies identified in 1976, which we now understand to be wholly correct, was a substitutional nitrogen adjacent to a vacancy[100] (shown in Figure 1.1 a)).

Figure 1.1 b) shows the band structure of diamond and where the NV center sits

relative to some other common defects[101]. The 1.945 eV transition that had piqued the interest of Clark, Davies, and du Preez was the NV^- electronic transition between two orbital states. The pair of nitrogen and vacancy has two primary charge states, the neutral NV (NV^0) and the negatively charged variant (NV^-, that has the 1.945 eV transition), hereafter referred to as the "NV"[11].

Following the discovery of the NV structure in 1976, research into the spin states of the NV would be immediately forthcoming. In 1977, Loubser *et al.*[103] would bring Johannesburg back to the forefront of NV research with an ESR study into the electronic structure. Loubser incorrectly concluded that an excited state triplet with a ground state singlet was responsible for their ESR measurements. In 1983, Collins *et al.*[104] would measure the excited state lifetime to be a shockingly short, 13 ns, giving the first hint that the Loubser explanation was not correct. In December of 1991, the level structure for the NV[12] would be conclusively shown by Michigander researchers Redman *et al.*[105] to be two spin-triplets with a dark intersystem[106] crossing. The electronic level structure of the NV has remained largely unchanged[13] since the 1991 Redman result[105].

The NV electronic level structure[108] is shown in Figure 1.2 a). The ground state triplet manifold (often referred to as the $^3A_2$ state), consists of an $m_s = 0$ ground state with two degenerate[14] $m_s = \pm 1$ excited states. Contrary to many spinful systems, there is a large zero-field splitting. The degeneracy between the $m_s = 0$ and $m_s = \pm 1$ states is lifted due to a large spin-spin coupling that gives rise to a crystal field, $D = 2.87$ GHz[109]. Upon excitation with a green laser, the orbital state will be pumped to the same spin-

[11]Though NV charge state manipulation can be useful in some measurement environments (notably spin-to-charge readout[102] is extremely efficient for *long* measurement schemes), the vast majority of NV work uses the NV^- charge state. Throughout most of the literature and this thesis, unless explicitly stated otherwise, the term "NV" refers to the negatively charged variant.

[12]By this time, the (not-very-catchy) name 1.945 eV vibronic band was discarded and the Davies structure was firmly agreed upon. From this point onward, the NV is called either the NV or the N-V (as is the case in the Redman 1991 paper).

[13]Details of the excited state structure[107] and dark intersystem[106] crossing were filled out later.

[14]In the absence of a field.

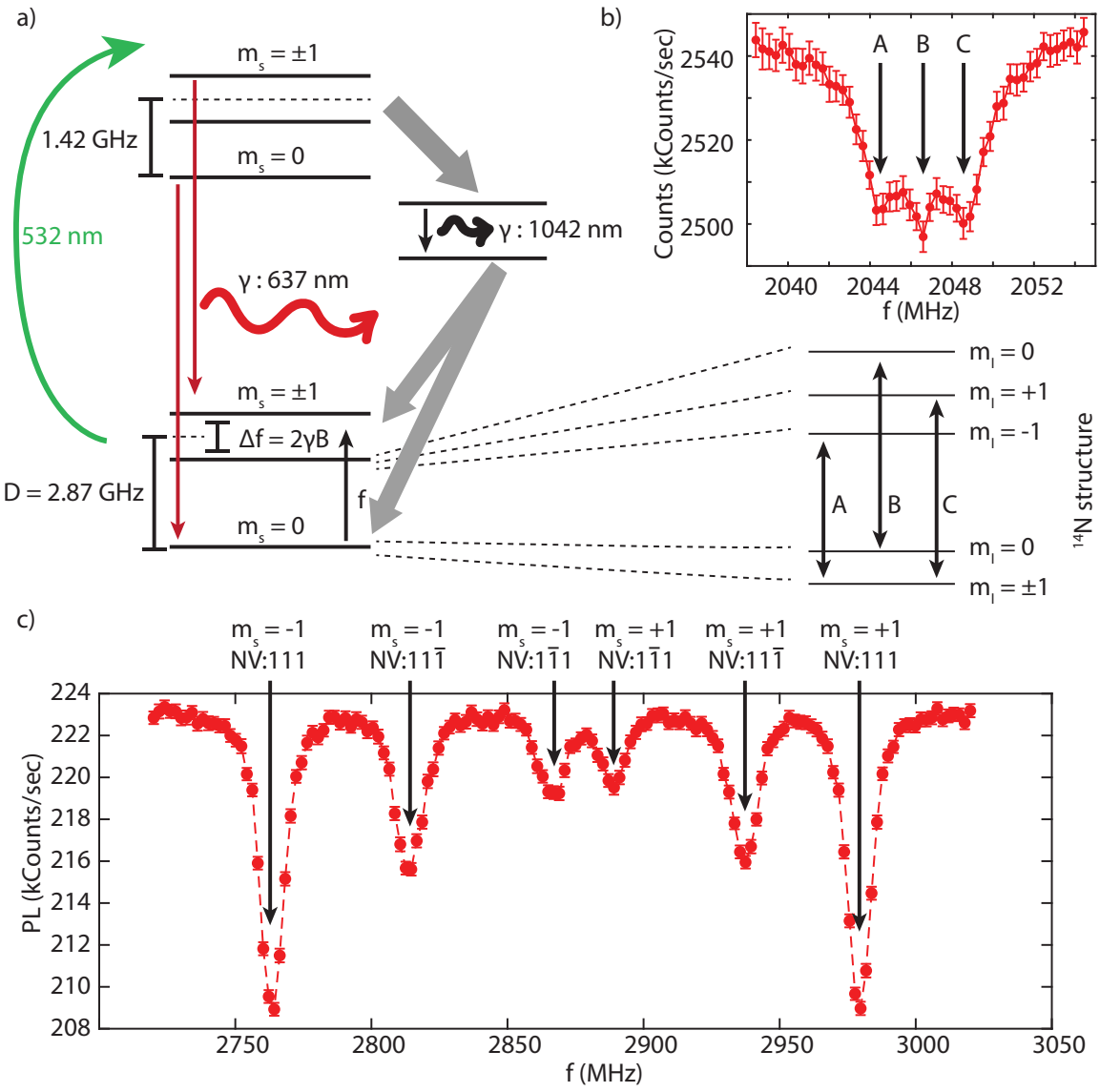

Figure 1.2: a) The electronic level structure of the NV center. A green laser pumps the system to the excited state where it decays either radiatively (small downward pointing arrows) or non-radiatively (large grey arrows). The selectivity of the non-radiative decay to the spin state allows for optically detected magnetic resonance (ODMR). b) ODMR of an NV center with the corresponding (^{14}N) hyperfine transitions illustrated below. c) ODMR of an NV ensemble across a wide frequency range. Pairs of peaks indicate pairs of electronic $m_s = 0 \leftrightarrow m_s = \pm 1$ transitions. The multiple pairs are due to the multiple possible orientations the NV can take.

state in the excited manifold. After a period of $\sim$ 13 ns[104], the system will decay to the ground state, releasing a 1.945 eV photon. However, approximately $\sim$ 30% of the time[15], should the NV be pumped to one of the $m_s = \pm 1$ states in the excited manifold, it will decay non-radiatively[16] through two singlet states, ^{1}A$_1$ and ^{1}E. After traversing the dark path, the electronic state will decay into either the $m_s = 0$ ground state or the $m_s = \pm 1$ states[108]. There are two essentially important elements to this structure: first, the photoluminescence (PL) of the NV center depends on the spin state (and so the spin state can be read out optically), and second, continuous repumping via a 532 nm laser is *guaranteed* to initialize the NV into the $m_s = 0$ state. These two elements result in an easy-to-address spin and make possible optically detected magnetic resonance (ODMR)[111] along with more complicated pulse sequences.

In 1997 Gruber *et al.*[111] observed ODMR on NVs for the first time. Through an application of a magnetic field, they were able to show that the resonant frequencies of the $m_s = 0 \leftrightarrow m_s = \pm 1$ transitions could be detected using *only* a confocal microscope and an RF generator. This demonstration heralded the widespread study of NV centers, made possible through the inexpensive and relatively easy-to-build confocal microscope. Figure 1.2 b) shows an example of ODMR on an NV at room temperature in ambient conditions. The three peaks here correspond to hyperfine transitions. Figure 1.2 c) shows a wide spectrum of NV peaks, with an applied magnetic field of $\approx$ 40 G. The transitions shown here come in pairs, where each element in the pair corresponds to either the $m_s = 0 \leftrightarrow +1$ or $0 \leftrightarrow -1$ transition. The splitting between the two peaks corresponds to the projection of the magnetic field along the NV-axis (the NV axis can point along

[15] Actually, it is only the difference in decay paths for the $m_s = \pm 1$ transitions and the $m_s = 0$ transitions that is $\approx 30\%$. There is a non-negligible branching ratio for the $m_s = 0$ transition. See Table XIII in Ref. [110].

[16] Actually, this is only mostly non-radiative. The ^{1}A$_1 \rightarrow ^1$ E decay releases a far infrared photon[106] which is usually filtered out.

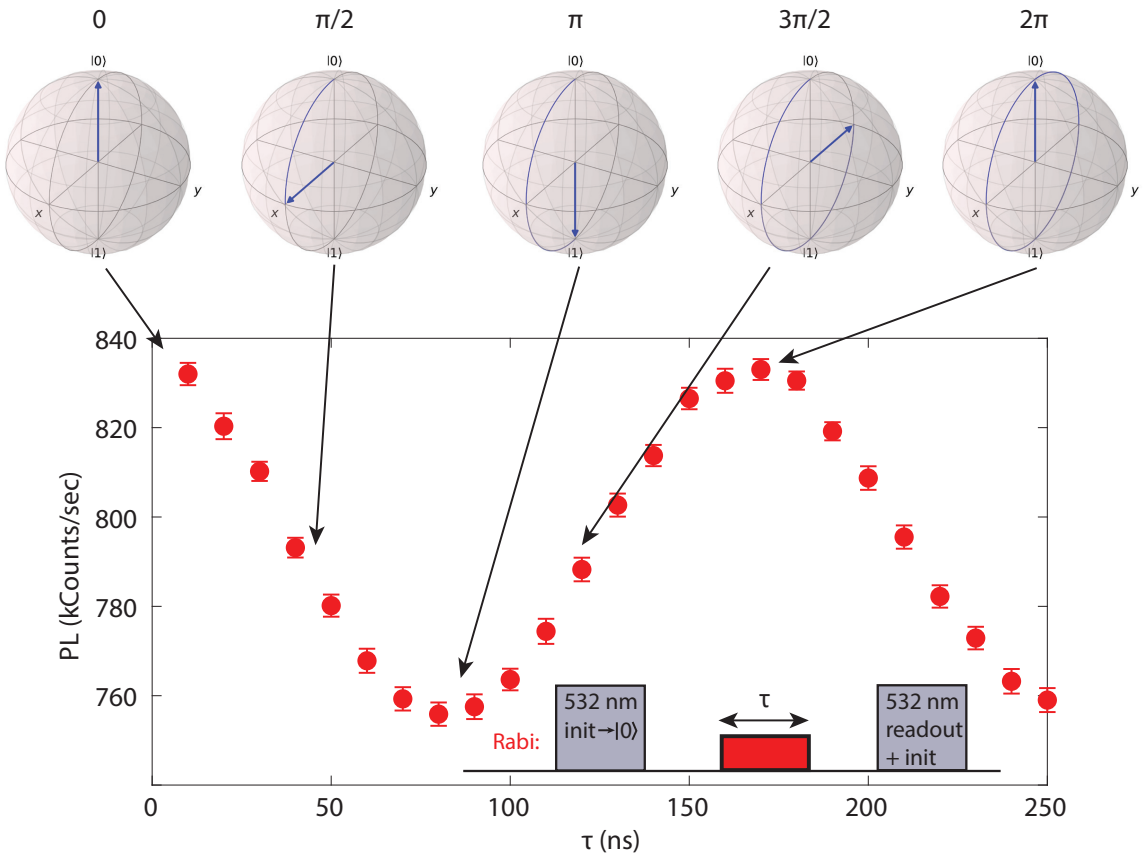

Figure 1.3: Rabi oscillations for an ensemble of NV centers. Bloch sphere representations of the state, along with arrows pointing (approximately) to the corresponding part of the Rabi oscillation are listed along the top.

the set of $\langle 111 \rangle$)[17].

By the early 2000s, all-optical, coherent manipulation of NV centers had already reached an advanced stage. Early experiments by Jelezko *et al.*[112] and Childress *et al.*[113] would demonstrate coherent interactions between NV centers and nearby nuclear spins. Controlled entanglement between electronic spins and proximal nuclear spins hints towards the exciting possibility of coupling the spin-photon interface of the NV center (and its high sensitivity) with the long quantum memories of the nucleus. Coherent ma-

[17]While 6 peaks are shown in this figure, we expect 8 in total. The extra two are probably overlapping with two of the others.

nipulation, as in these demonstrations requires the Rabi protocol[114, 19], a fundamental building block for quantum control. Figure 1.3 shows an example of a Rabi oscillation in an ensemble of NV centers. An NV Rabi sequence consists of a green initialization into the $|0\rangle$ state followed by an RF pulse of length τ at a frequency equal to the transition of the qubit basis states one is hoping to use (in our example, we will say we are driving the transition $|0\rangle \leftrightarrow |1\rangle$). Under the application of the RF, the state will proceed along the Bloch sphere[19] at a constant rate, called the Rabi frequency, Ω. The qubit will travel along a great circle that includes the states $|0\rangle$, $|1\rangle$, and two points along the equator (called $|\pm x\rangle$). By choosing a set time to keep the RF on, an experimenter can prepare any arbitrary state along the Bloch sphere, as shown in Figure 1.3. In this thesis (and the extended literature), when we refer to a π-pulse or a $\pi/2$-pulse (or π-gates), this is what we mean. The RF is on for a set time, τ, such that $2\pi\tau\Omega = \pi$ or $\pi/2$.

As NV center experimental methodology and practices matured, sensing would begin to occupy an increasingly large portion of the field. Early, proof-of-concept experiments would increasingly give way to experiments where the NV would act as a tool to study some "other" physics, rather than acting as the object of study itself. Most of these sensing tasks would take the form of magnetic field sensing, though the NV can sense a variety of fields including electric, temperature, and strain. Though ensembles of NVs can be used for sensing tasks[115, 116], the most dramatic advance in NV sensing would come with the advent of single NV magnetometry. Single NV magnetometry refers to experiments where a shallow, single NV is interrogated while proximal to a target of interest that acts on the NV in some way, changing its observable properties. The fundamentally atomic nature of the NV ensures that the best possible achievable spatial resolution is, fundamentally, atomic[18]. In the early 2010s, two different modes of single

[18]In practice, spatial resolution for scanning NVs is far from atomic. The limit to the spatial resolution comes from how close you can bring the NV to the target of interest. Usually, this works out to be $\sim 50 - 100$ nm.

NV sensing would arrive. The first type, appearing in 2011 by Grinolds *et al.*[117], uses fixed shallow NVs and a target that is attached to a scanning probe. In this scheme, the NVs sit in a bulk diamond and the sample is scanned over top. The main disadvantage of this scheme is that it must be possible to affix the sensing target to the scanning probe, fundamentally limiting the accessible pool of sensing targets. The second scheme, introduced by Maletinsky *et al.*[37] in 2012, uses a fabricated diamond nanopillar with a single NV at the apex. Scanning this tip over the sample (or, more commonly, scanning the sample beneath the tip), allows the experimenter to build an image over an arbitrary sensing target, allowing for a much broader set of possible experiments.

While the early examples of scanning NV magnetometry were room-temperature, in 2016, scanning NV magnetometry would be extended to the low temperature and ultra-high vacuum regime by Pelliccione *et al.*[14]. Low-temperature NV magnetometry opened up the possible systems available for sensing to a wide range of temperatures and pressures (mK $\rightarrow\sim 600\,\mathrm{K}$[118, 119] and UHV $\rightarrow\sim 100\,\mathrm{GPa}$[14, 120, 121, 122]).

While most of the early examples of scanning NV magnetometry were DC-sensing (in the case of CWESR, a fundamentally incoherent mode), coherent sensing remains an attractive prospect for scanning NV sensors. AC sensing sequences offer field sensitivities $2-10\times$ higher than the DC counterpart[110, 123]. These sequences are often either spin echoes[23] or more complicated sequences[124] built around the central idea that Erwin Hahn proposed in 1950. A spin echo (or sometimes, Hahn echo) is a pulse sequence initially developed for NMR, whose primary function is to remove random DC magnetic fields that result in uncontrolled dephasing.

An ensemble[19] of equatorial NVs will begin to acquire random uncontrolled phases. These uncontrolled phases are due to slightly different B-fields acting on each NV in

[19]Either a time ensemble (i.e., averaging the same NV over many different instances) or a space ensemble (i.e., a single (or many) instance(s) of averaging many different NVs distributed over space).

the ensemble; because the rate of phase accumulation is proportional to these random fields, the distribution of phases will grow over time until the ensemble has completely dephased. Erwin Hahn's insight was that a π-pulse would reverse the sign of each of the B-fields in the ensemble and, thus, reverse the rate of phase accumulation. Hahn found that if the π-pulse was sandwiched between two waiting times, τ, the spins would spontaneously *re*phase due to the exact cancellation of these random magnetic fields across the ensemble - he called this rephasing an "echo".

Figure 1.4 shows a schematic for a spin echo, the pulse sequence, and data on an NV ensemble that will be discussed later in Section 4.3. An NV spin echo consists of a green initialization pulse to prepare the $|0\rangle$ state followed by a $\pi/2$-pulse to rotate the NV onto the equator of the Bloch sphere. After an evolution of time, τ, we perform a π-pulse and then allow the system to accumulate phase for another time, τ. Finally, we perform a $\pi/2$-pulse and a green laser pulse for state readout. This sequence is useful in a sensing context because, while it perfectly cancels all DC components, it amplifies the signal at a frequency, $f = 1/2\tau$.

Not only can spin echo-based sequences be used to sense *ex-situ* targets, but so too can they be used to sense targets within the diamond itself to explore fundamental many-body physics. The NV is currently a prime candidate for exploring topics in many-body quantum physics[125]. Alongside the push towards sensing at the start of the 2010s, the prospect of shifting from exploring NV-specific physics to using the well-understood NVs to study fundamental physics started to become feasible. By 2013 and 2014, Cai *et al.*[126], and Ju *et al.*[127] had made serious proposals for NV center quantum simulation. Today, many groups are pursuing NV center ensembles as a means of gaining insight into otherwise intractable problems in many-body quantum physics. This topic will form the central point of discussion for this thesis.

In the following pages, we will discuss methods for engineering ensembles of NV

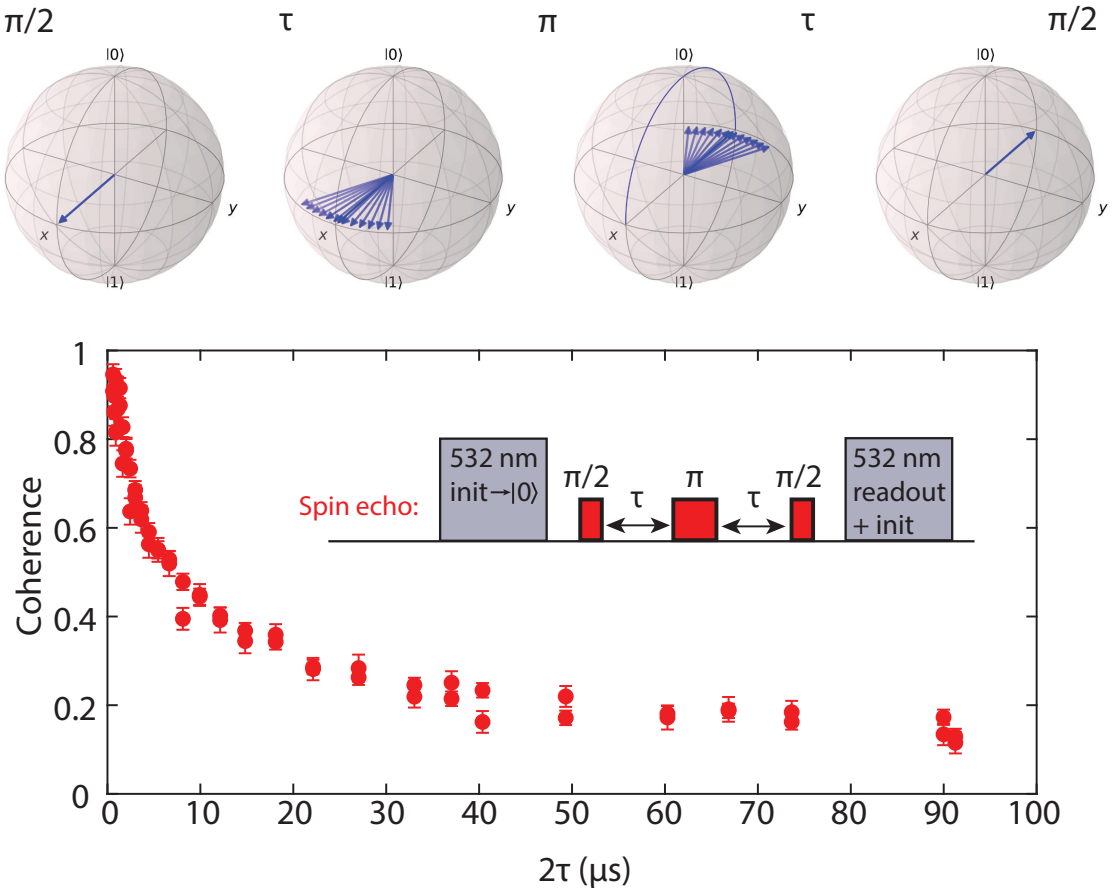

Figure 1.4: An example of a spin echo measurement on an ensemble of NV centers. Along the top are Bloch sphere representations of the ensemble state (with the multiple arrows representing multiple instances within the ensemble). A refocusing π-pulse results in a coherence "echo". The data depicts the coherence of a state as the time between the initial and final $\pi/2$-pulses and the central π-pulse is varied. The "$1/e$ time", that is, the time at which the coherence reaches $1/e$, is commonly called the T_2. The decay depicted here is for a 1D ensemble, as described later in Section 4.3 and follows a stretched exponential form. The detail of this decay provides a window into the many-body dynamics of the system.

centers with a focus on the role that dimensionality plays in many-body quantum physics. We will discuss how dimensionality, that is, the confinement of a quantum many-body system to lower dimensional spaces, gives rise to unusual physics unobtainable in higher dimensions. We will cover methods for engineering systems in 3D, 2D, and 1D, as well as methods utilizing periodic drive to generate long-lived coherent ensembles, generate modified Hamiltonians, and probe the material environment. Finally, we will discuss a method for coherence extension: confinement to a 1D chain, where the small interaction boundary limits the rate of decoherence and results in finite coherence $\sim 100\times$ longer than T_2.

I now return to the question posed at the start of this section: what is it about the NV center that has resulted in it garnering such a colossal amount of interest? I do not think it is an accident that the NV recipe developed by du Preez in 1965, before anybody even understood what the NV was, has remained almost intact to the present day. The NV is remarkably easy to create, easy to measure, and easy to keep around[20]. While I do not wish to claim state-of-the-art NV center measurements are easy - anybody who has attempted low-temperature scanning NV magnetometry can surely confirm that they are not - I do wish to underscore the profound accessibility of the NV center.

The compatibility of the NV with conventional confocal microscopy and coherent operation in virtually any environment means that the NV is eminently accessible. I can think of no other qubit platform where a person can go from an empty lab and $\sim$ \$10k USD to bonafide, coherent qubit manipulation in only a few weeks. Discussions on the NV center as a pedagogical tool for teaching quantum mechanics have become more common[128, 129] (even appearing at the Quantum Foundry in UCSB), and I do not

[20]While it is, unfortunately, possible to lose a good NV sample, it is almost impossible to destroy a good diamond sample (owing to the robustness of the host material). Barring destruction due to burning the diamond, there is very little that will result in the death of a deep NV. Even shallow NVs, which can be charge-destabilized due to fluctuations from a noisy surface, are often recoverable through retermination and/or cleaning of the surface.

think it is unrealistic to hope that one day, experimental demonstrations of superposition and entanglement may become commonplace in the high school classroom.

I recall one winter afternoon, as I was giving a tour of the UCSB Quantum Foundry facilities, I stopped outside of our diamond growth tools to explain some of the principles of quantum mechanics. As I was describing the concept of a superposition, one of the students asked, incredulously, whether I had ever created such a state. "Every day," was my reply. Perhaps, one day, that reply will be met with less surprise.

Chapter 2

Diamond growth and the role of substrate miscut

Since the discovery that diamond consists only of carbon in 1772 by the French chemist Antoine Lavoisier[130, 131, 132], the tantalizing idea that diamond could be synthesized has gripped early chemists and materials scientists [1]. By the 1940s, serious efforts in the United States began to create the first reproducible synthetic diamonds. On the morning of December 16th, 1954, after most of the researchers in the General Electric (GE) laboratories had already left for Christmas vacation, American chemist Howard Tracy Hall began his final test of a high pressure (5 GPa) and high temperature (1250°C) chamber[133]. After the test, when Hall broke apart the dusty crucible within his chamber, he found many sparkling tiny particles amongst the soot. These would turn out to be the first ever reported [2] reproducible synthetic diamonds - the technique used

[1] Antoine Lavoisier was a pioneering chemist in the field of combustion. It was well known that diamond could resist heat in a vacuum but would burn when exposed to air. Lavoisier used his theory of combustion to show that upon burning diamond, the only byproduct was carbon dioxide - an experiment (unfortunately) sometimes replicated by graduate students during material processing.

[2] Actually, the first known synthetic diamonds produced were in Stockholm in 1953 by the company ASEA (Allmänna Svenska Elektriska Aktiebolaget), nearly a year before Howard Tracy Hall [134]. However, the board at ASEA did not believe anybody else was close to achieving repeatable synthetic

in these proof-of-concept experiments is very similar to what we would eventually call high-pressure, high-temperature (HPHT) diamond growth. However, these early demonstrations were not industrially scalable and did not result in gem-quality crystals. It would still be many years and require several breakthroughs before commercially viable synthetic diamonds entered the market.

The breakthrough that finally allowed gem-quality, commercially viable synthetic diamonds was chemical vapor deposition (CVD), which will be the main subject of this chapter. Chemical vapor deposition is a non-equilibrium technique that proceeds in a low-pressure environment using a seed substrate held at an elevated temperature. Hydrogen and methane gas are introduced into the chamber, and the hydrogen is energized using one of a few possible methods. The two most common methods are hot-filament CVD (HFCVD) and plasma-enhanced CVD (PECVD) [135]. For HFCVD, a hot filament is placed close to the seed substrate, producing atomic hydrogen close to the substrate. PECVD produces atomic hydrogen using a microwave-driven plasma at frequencies usually ranging from 100s of MHz to ~ 2.5 GHz.

Though CVD diamond growth was patented in 1958[136], it was not until the 1980s that the process would be sufficiently refined to produce gem-quality diamond [135, 137]. It took even longer for this process to become commercially viable and did so primarily due to the availability of cost-effective microwave sources[135]. Today, the growth of synthetic diamond has become an increasingly significant global endeavor for several applications ranging from wide bandgap semiconductors for devices with better energy efficiency [138], quantum sensing and simulation applications (the focus of this thesis) and, notably, jewelry.

The methods and details of the CVD growth employed in this thesis can be found in

diamond creation, so they did not come forward to patent or publicize their results and instead opted for secrecy. Because of this, today, most credit GE and Hall as the first to create synthetic diamond.

the theses and work of Kenichi Ohno[139], Bryan Myers[140], and Claire McLellan[141]. In this chapter, we will briefly summarize the methods we use for CVD growth and NV creation (primarily developed by the authors listed above). Most of the chapter will focus on the physics of step flow growth and how substrate miscut plays a significant determining role in that physics. The discussions in this chapter will form the basis for the discussion in Chapter 4 - we will find that substrate miscut can lead to inhomogeneous incorporation and low dimensional systems.

2.1 Introduction to CVD diamond growth

The main antagonist to a diamond grower is that diamond is not the equilibrium state of carbon at standard temperatures and pressures [3] - but rather, graphite is the ground state for carbon [142, 143]. Consequently, a synthesizer of the diamond must fabricate an environment far from standard conditions and then provide a seed substrate from which the growth may proceed. Sufficiently high temperatures and high pressures can mimic the conditions found in the earth's upper mantle, where diamond forms naturally. Another way to generate out-of-equilibrium conditions is to create a plasma around a diamond seed substrate. The ionizing plasma creates highly reactive species that readily incorporate onto the seed substrate. Figure 2.1 a) shows a phase diagram for carbon adapted from Ref. [143]. CVD growth of diamond usually occurs at temperatures of $\sim 800°C$.

CVD growth is attractive because it allows for good control of impurity concentration relative to HPHT growth[4]. CVD-grown diamond can, with relative ease, achieve

[3] In contrast to, for example, silicon, which does not require out-of-equilibrium chemistry to form the diamond-lattice phase.

[4] Although, especially in recent years, HPHT growth's high concentration of nitrogen impurities has become a selling point in the NV center community. Still, for the best control over impurities, CVD is not matched. As of now, HPHT can only be used to create large 3D ensembles of dense nitrogen

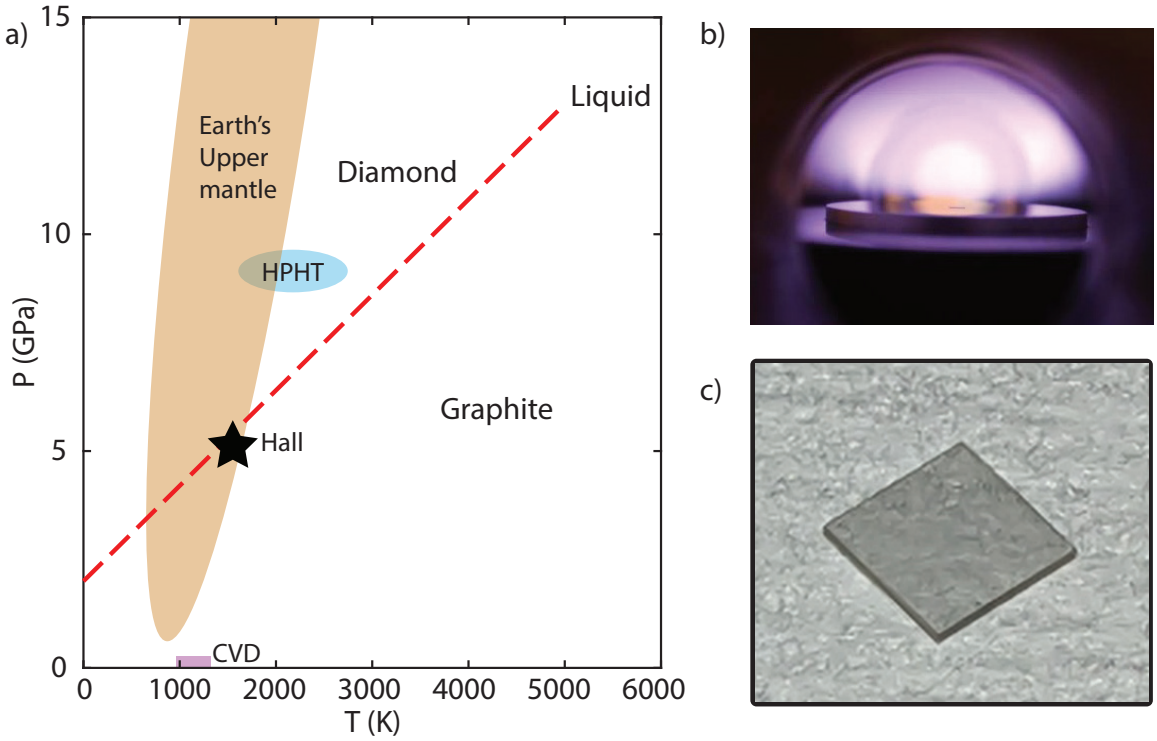

Figure 2.1: a) Phase diagram for carbon (adapted from Ref. [143]). The red dashed line indicates the phase boundary between diamond and graphite. For low pressures, carbon tends to form graphite preferentially. The temperatures of CVD growth are shown on the bottom, though CVD generally occurs at low pressures - the size of the box has been exaggerated for clarity. The star indicates the temperature and pressure conditions where Howard Tracy Hall first synthesized diamond in 1954. b) Image showing a diamond sample undergoing PECVD crystal growth. c) Photograph of a grown diamond sample (S001).

impurity concentrations of $\lesssim$ ppb, and so in applications where precision in the depth and concentration of dopants is important, CVD is the better choice. The purity of the gases used can limit the impurity concentration in CVD growth, whether the gas lines are leak-tight, impurities that may have aggregated on the chamber walls, or the purity of the seed substrate or sample holder[5].

and can not be used for the localization required for probe fabrication or 2D layers, as will be discussed elsewhere in the text.

[5]Etching and redeposition of the seed substrate can result in higher impurity concentration if the seed substrate has high impurity concentration.

2.1.1 Diamond growth recipe

For details on the optimization of the growth parameters below, I will refer the reader to Kenichi Ohno's thesis[139] and Ref. [88]. For the growths described in this section, we used a SEKI AX6300 PECVD tool. Figure 2.1 b) shows a photograph of a sample inside the chamber during growth. For a detailed description of the growth, I refer to Claire McLellan's and Kenichi Ohno's theses[141, 139]. We will briefly summarize the steps for growth below.

- Load sample and pump down overnight (to $\lesssim 1e-8$ Torr)
- Start the hydrogen plasma (3 Torr, 25 sccm hydrogen, 450 W microwave RF power).
- Raise the plasma to 25 Torr and 400 sccm hydrogen. Set the RF power to 750 W while tuning the microwave impedance.
- Raise the sample temperature to 800 °C and wait for 15 minutes. During this step, the hydrogen plasma will etch the surface slightly.
- Introduce methane at a flow rate from 0.1 sccm to 0.3 sccm[6]. This is the buffer layer that separates the high-quality grown diamond from the disordered substrate.
- If one wants to dope with nitrogen, we introduce nitrogen gas for doping at a flow rate of 0.1 sccm or higher. High flowrates of nitrogen can destabilize 001 growth.
- Turn off the nitrogen and grow an undoped capping layer[7]. Figure 2.1 c) shows an photograph of a (2×2 mm) grown sample (S001).

[6] I have found that higher methane flow rates result in highly abnormal growths.

[7] This capping layer can be made small if near-surface NVs are desired. For experiments that do not require interfacing with a surface, it's generally best to grow the thickest capping layer possible to remove surface noise from the NV layer.

2.2 Step flow and miscut

One of the major difficulties in diamond growth (and crystal growth in general) is the profoundly large parameter space one needs to optimize over. Temperature[144, 145, 146, 147], pressure[144, 148], gas phase composition[149, 148], gas flow rate[150, 151, 152], the presence of nitrogen dopants[153, 154] , microwave power[155], substrate position within the plasma[156], and many, many more parameters all effect the morphology and quality of growth in dramatic and often difficult-to-predict ways. Our goal is to maintain good coherence and properties for our qubits which require very high-quality films; a goal we approach using our low-growth-rate recipe. In this section (and the rest of the chapter) we will explore the effect of a single intrinsically important parameter in growth: the density of step edges (controlled via the substrate miscut).

In layer-by-layer deposition schemes, high-quality crystal growth often begins with step flow growth. Because during the polishing process, the (001) plane of the diamond is never perfectly parallel to the polishing plane, there always exists some finite density of atomic steps with a step density, n_s equal to,

$$n_s = \sin(\theta)/a, \tag{2.1}$$

where a is the atomic height of the step and θ is the polar miscut angle, defined by,

$$\arccos(001 \cdot \hat{n}) = \theta, \tag{2.2}$$

where, $\hat{n}$ is the surface normal vector.

Figure 2.2a) shows a schematic depiction of step flow growth. Here, the methane is radicalized by the plasma and reacts on the surface, creating carbon adatoms. These

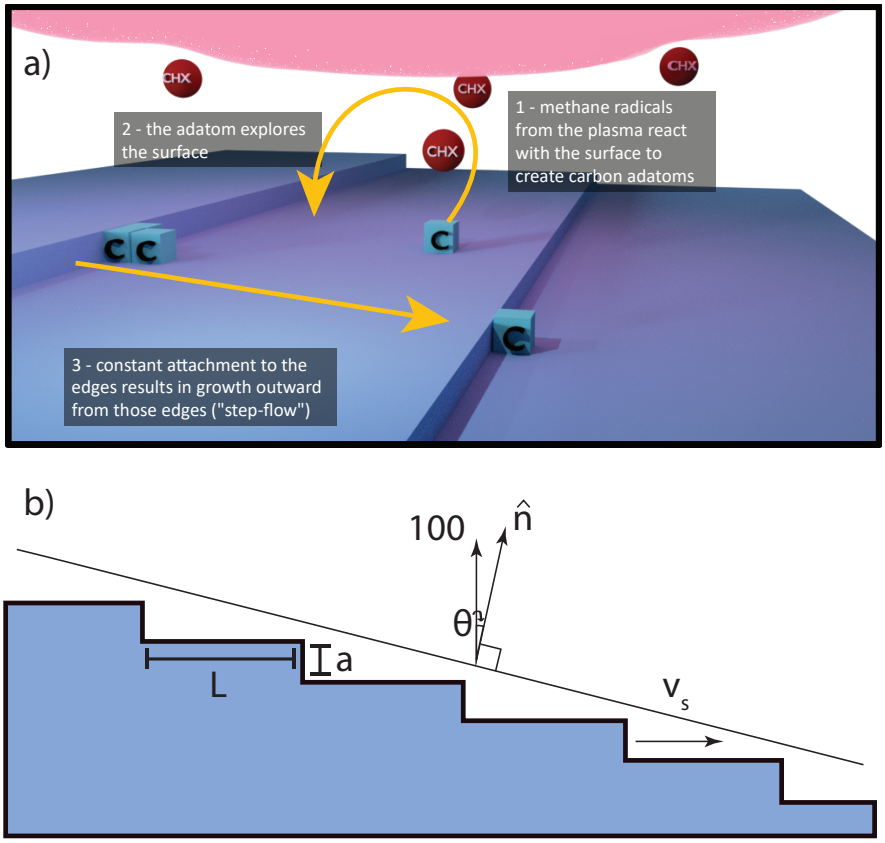

Figure 2.2: Diagram of CVD step flow growth. a) During growth, adatoms arrive on the surface due to interactions between the hydrogen plasma and the methane. The hydrogen creates reactive methane groups that land on the surface, creating a hydrogen adatom. These adatoms sample the surface stochastically. Because the coordination is highest at the step edges, the carbon adatoms incorporate most easily there. As more and more adatoms incorporate at the step edges, these edges will tend to "flow" outward, resulting in so-called step flow growth. b) A diagram of a vicinal surface. The miscut is defined as the deviation of the surface normal from the desired crystallographic direction.

adatoms explore[8] the surface of the seed substrate until they encounter a step edge, where they tend to stick because the higher coordination makes incorporation energetically favorable. As more and more adatoms stick to the step edges, the step edges will tend to "flow" outwards, building a single crystal surface one atomic layer at a time[160, 139]. To achieve well-ordered step flow, which generally results in a well-ordered crystal free of too many defects, a slow adatom arrival rate must be achieved. This slow arrival rate is required because if the adatoms arrive too quickly, they will tend to find other adatoms before finding a step - this results in other, disordered, growth modes[9]. One such disordered growth mode is the hillock defect, which will be discussed in a later section.

The step velocity (and hence, the adatom arrival rate) can be determined by measuring the growth rate as a function of miscut. This is made clear by the relationship between the growth rate along the surface normal v_g and the growth rate along the step direction, v_s,

$$v_g = v_s \sin\theta \approx v_s\theta. \tag{2.3}$$

2.2.1 Measuring miscut via X-ray diffraction

The importance of miscut in determining the morphology, growth rate, defect incorporation and surface quality in CVD growth is, therefore, well-founded, and so we will

[8]I will note that the mechanism behind the surface exploration is not entirely clear. There was some controversy in the mid-90s about the mechanism behind step flow[157, 158, 159]. There are two main mechanisms that I am aware of: chemically mediated diffusion as proposed by Frenklach *et al.* and hydrogen mediated etching and redeposition. I know of no convincing experimental demonstration of the sole dominance of either mechanism, and for the purposes of this thesis, we can treat the adatoms as stochastically sampling the seed substrate surface by one mechanism or another. I bring it up as a footnote because, as far as I am aware, it is an interesting puzzle that has yet to be convincingly solved.

[9]See Tsao's Chapter 6 in Materials Fundamentals of Molecular Beam Epitaxy[161] for a discussion on morphology's relationship to growth modes. The text itself is focused on MBE instead of CVD, but nevertheless, much of the step flow MBE intuition and insight also applies to step flow in CVD.

spend some small time discussing the principles behind how we measure the miscut. The miscut is defined as the angle between the surface normal and the crystal lattice, and so both the vector corresponding to the surface normal and the vector corresponding to a lattice direction must be co-determined accurately.

Figure 2.3a) shows a schematic diagram of the miscut measurement. We accomplish this using X-ray diffraction (XRD) for the lattice and X-ray reflection for the surface normal. At low angles, a clean and well-polished diamond surface is mirror-like for X-rays, so the surface reflection can align the surface normal to the lab z-axis set by the instrument. First, the source and detector beam axes must meet at the surface of the diamond. This can be ensured by aligning the source and detector beam axes to the lab x-axis set by the instrument and then gradually raising the diamond sample. Because diamond is semi-transparent to the beam, extra care must be had during this step relative to a more typical XRD procedure. Figure 2.3b) shows an illustration of typical data obtained during this step and the correct z-position to place the sample. Next, two steps must be performed iteratively until good alignment of $\hat{n}$ is achieved. The first step is a rocking curve about a shallow angle ($\lesssim 1^\circ$) where the source angle is kept constant, and the detector angle is swept - the maximum count rate indicates the position where the X-ray source and detector make equal angles with respect to the surface normal. The second step is to set your detectors to the maximum found in the first step and then rotate the angle about the x-axis - the maximum here is the point where $\hat{n}$ is best aligned to $\hat{z}$ in the zy-plane.

The $\hat{n}$ alignment procedure is summarized below:

- Set the beam and detector axes to run along the lab x-axis, i.e., set them to $\omega = 0$ such that both axes are perfectly horizontal.

- Raise the sample while monitoring the intensity. There should be two notable

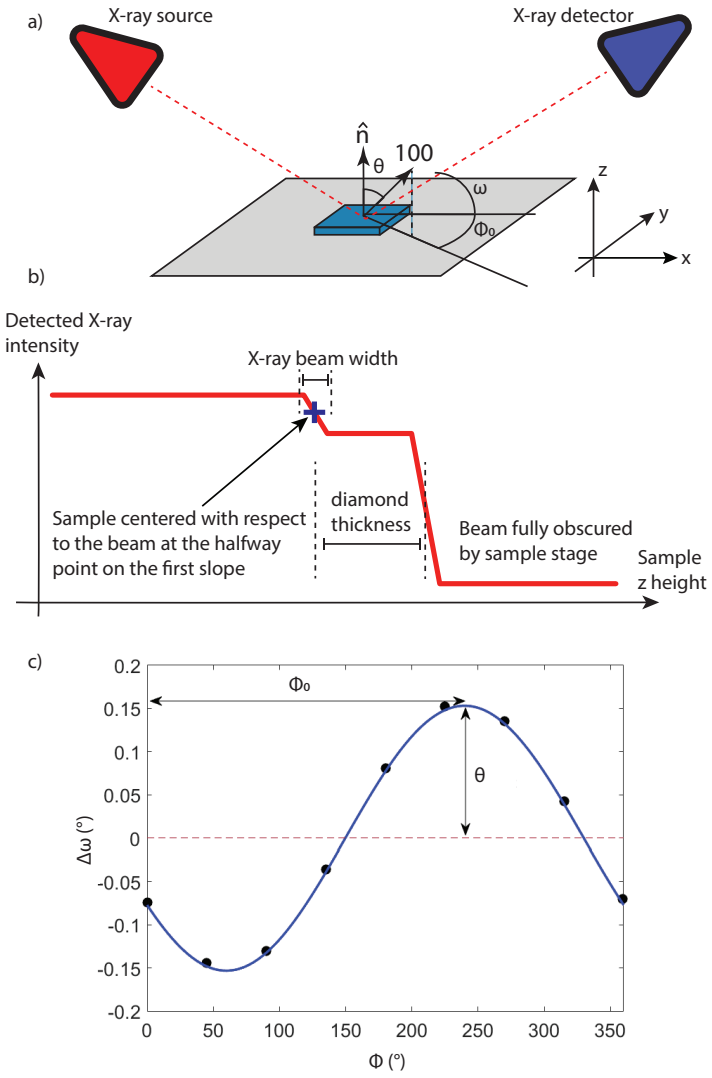

Figure 2.3: a) A schematic of the experimental setup for measuring the miscut using an X-ray diffractometer. b) An illustration showing how to align the z-position of the sample within the apparatus. The purple "+" shows the position where the X-ray beam should be centered. This is different from usual X-ray alignment and requires manual input since the diamond is semi-transparent. c) An example of data used to infer the direction of the miscut. The deviation of the Bragg peak from the expected location (assuming zero miscut) as a function of the azimuthal angle, ϕ shows a cosinusoidal dependence. The amplitude of the cosine indicates the magnitude of the polar angle, and the phase indicates the in-plane direction of the miscut.

drops in the intensity vs z - the first drop corresponds to the upper surface of the diamond.

- When the intensity drops to the midpoint between the intensity when the diamond fully obscures the beam and when the beam is unblocked, this means the beam is half-occluded and thus centered on the sample surface.

- Iterate over the next two steps:

- Perform a shallow angle rocking curve ($\omega \lesssim 1^\circ$)

- Optimize counts at this angle by rotating the sample about the x-axis (often called χ in XRD instruments)

Following this, the vector $\hat{n}$ will be well-aligned to the laboratory z-axis.

Next, we need to determine the direction of the 001 crystallographic direction. This is accomplished using the usual Bragg criterion[162]. We perform rocking curves[163] about the 004[10] (fixing the source axis to the expected peak location and sweeping the detector axis). The location of the maximum intensity as the detector axis is swept will not be exactly at the expected position but instead will have a slight deviation $\Delta\omega$. This deviation corresponds to the angular deviation in the projection of the 001 axis on the plane formed by the source and detector axes (the zx-plane). By rotating the sample and repeating the alignments above, we obtain the projected polar deviation as a function of the azimuthal angle, ϕ, which will (for small miscuts) have the form,

$$\Delta\omega = \theta \cos(\phi + \phi_0), \tag{2.4}$$

where θ is the polar miscut and ϕ_0 indicates the direction of the miscut with respect

[10]Because 004 is the first peak that is not destroyed by interference

to the in-plane crystal axes (e.g. 110). An example of one of these measurements is shown in Fig.2.3c).

2.2.2 Varying miscut

Crystal growth is, in general, a complicated affair, and inferring statistical trends can be difficult. A single sample can represent weeks of work; each growth corresponds to at least one day of growth with a few days in preparation before growth, and the characterizing measurements post-growth can, also, take many days to perform. Therefore, acquiring large enough numbers of statistics to infer meaningful trends can take a very long time. To make matters more complicated, day-to-day variations introduce confounding variables[11]. Because of the time cost associated with sample growth, there is always the temptation to vary multiple parameters at the same time, and indeed, when one looks back to try and tease out a trend from years of samples, many of the parameters *were* intentionally varied. Because the control space for growth is so large, finding a series of samples where every possible control variable is kept constant except for one is often extremely difficult. To combat this problem, one can attempt to vary a single control parameter within a single growth, which can eliminate many of the systematic errors introduced by day-to-day variation. By measuring the miscut using XRD and indicating the in-plane direction, when we send the samples to Syntek for polishing[164], we ask for polishing along a specific direction at an angle. Their accuracy is usually extremely good, and they are able to generate specific miscut angles with an accuracy of $\delta\theta < 0.05°$.

To test the effects of miscut, we accomplished this "single-sample" variation by intro-

[11]I will not discuss all of these but will list a few: the position of the sample within the chamber, sample temperature (which we can control), the cleanliness of the chamber (which degrades on a several-month scale), the cleanliness of the sample before loading into the chamber, the relative concentration and purity of the gases.

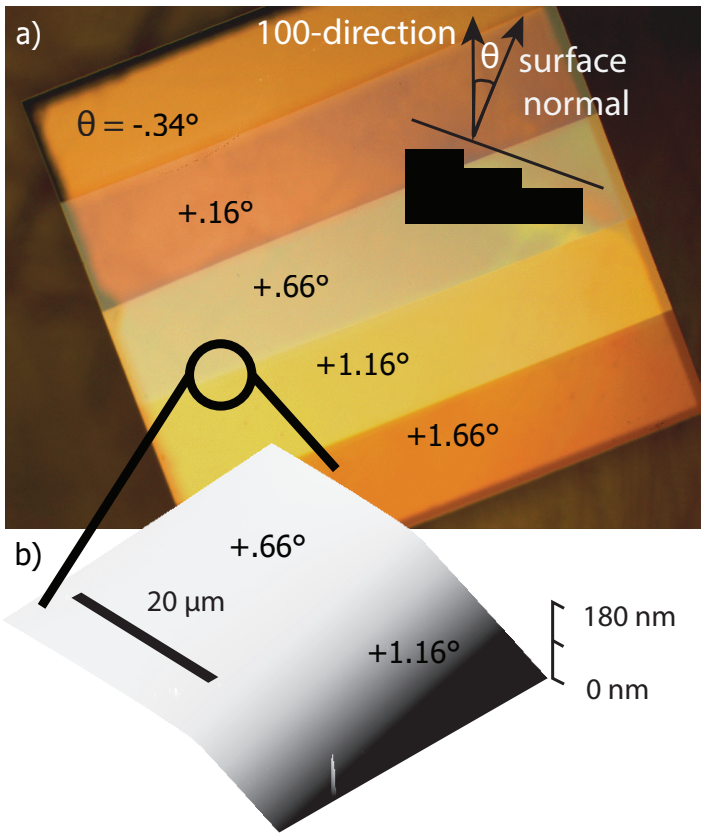

Figure 2.4: Sample S014, which was polished with five different miscuts, each 0.5° different from each other, to systematically study the effect of miscut within a single growth. a) Optical image of S014 where the different miscut regions are visible. b) Atomic force microscopy (AFM) image close to a boundary region.

ducing multiple miscut regions on a single sample, each separated by 0.5°. Figure 2.4a) shows an optical image of this sample, called S014, with the various miscuts[12] noted. Figure 2.4b) shows an atomic force microscopy (AFM) image of the sample close to a boundary, confirming the 0.5° miscut difference.

Sample S014 was grown with the following recipe:

- 0.1 sccm 99.999% ^{12}C isotopically enriched methane and 400 sccm H_2
- Nitrogen doping used 5 sccm 98% purified ^{15}N

[12]When performing the XRD measurement of S014, you can actually detect all five miscuts in a single sweep during the $\hat{n}$-alignment step.

- A three-hour nitrogen-free diamond buffer layer
- A six-hour nitrogen-doped layer
- A four-hour nitrogen-free capping layer

2.2.3 Nitrogen incorporation, growth rate and miscut

Next, we analyze the carbon incorporation (through the growth rate dependence) and the nitrogen incorporation as a function of miscut. We measure both aspects primarily through secondary-ion mass spectroscopy (SIMS). SIMS is a destructive technique where an ion beam (Cs, in this case) ablates the surface of the sample, producing a secondary beam of ions from the ablated material. Mass spectroscopy is performed on the ablated material to analyze the material composition, and as more material is ablated away, deeper parts of the sample are probed. Measuring the composition as a function of time for a fixed ablation rate results in a composition as a function of depth.

First, we consider the isotopically purified carbon layer (composed primarily of ^{12}C). We measure the content of the ^{13}C, which has a natural abundance of 1.1% but is substantially lower in the grown layers, although it should be noted that the concentration is far from what would be expected for the 99.999% isotopically purified methane used. Figure 2.5a) shows the concentration of ^{13}C as a function of depth for the five different miscut regions with the curves offset from each other for clarity. Curiously, there is a dip in ^{13}C concentration during the doping step at around halfway through the grown layer and at the very start of growth [13]. We do not observe any dependence on the isotopic

[13]These dips in concentration provide hints at what may be causing the increased level of ^{13}C relative to the source gas. Further hints at the cause of the enhanced level come from the observation that the isotopic purity improves with larger methane flow rates. This indicates that the enhanced level of ^{13}C is not due to enhanced impurities in the source gas or leaks in the methane lines but instead originates from some other source, possibly either the seed substrate itself or aggregate carbon on the walls of the chamber. An estimate from the impurity concentration relative to the source gas gives an effective background impurity flow rate of 0.02 sccm.

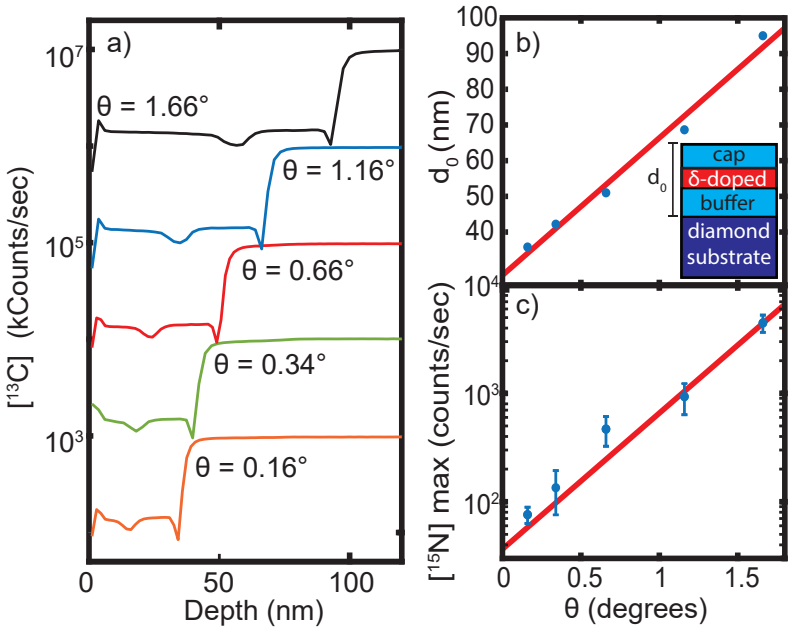

Figure 2.5: Secondary-ion mass spectroscopy data (SIMS) for various miscuts. a) The concentration of ^{13}C over a grown layer for each of the five miscuts. Curves are each offset for clarity. b). The regions with lower levels of ^{13} are the grown layers, from this we can gauge the layer thickness and hence, the growth rate. b) The layer thickness as a function of miscut. The linear dependence indicates a site-limited type of growth, which is only possible if surface diffusion is playing a minor role. c) The incorporation of nitrogen as a function of miscut. Note that the y-axis is log-scale, indicating an exponential increase in incorporation. This is suggestive of a non-linear incorporation mechanism.

purity with miscut, but we can readily see that the layer size is greatest for higher miscuts - indicating that the growth rate is higher for larger miscuts. This is evidence that we are in the step flow regime of growth and are limited by available sites (as opposed to purely limited by available adatoms, which is the case for conventional MBE). The observation of site-limited physics indicates a surface exploration mechanism other than simple MBE-like surface diffusion. If the adatoms explore the surface via continuous removal and redeposition, this would result in a scaling like the one observed in Figure 2.5b), whereas a model where adatoms stick and randomly walk until they hit a site, results in an adatom-limited regime. One can understand why this must be so with a simple argument: if every surface adatom *eventually* encounters a step edge, then the growth cannot be limited by available sites and rather must be limited only by available adatoms. However, continuous removal and redeposition of adatoms would result in the linear scaling with miscut that we observe.

The nitrogen incorporation also increases with miscut but, interestingly, increases superlinearly as opposed to linearly, as in the case of carbon incorporation. The superlinear dependence of nitrogen incorporation with miscut indicates mechanisms alternative to simple step incorporation is playing an important role. As discussed in later sections, step bunches become more important at higher miscuts, resulting in rough, defective surfaces. A possible explanation for the superlinear dependence of nitrogen incorporation could be nitrogen's preferential incorporation at sites with a high density of defects.

2.3 Morphology and miscut

Morphological features on the sample can play a large role in determining many aspects of NV center physics. Because the NV is sensitive to lattice strain[165], and crystal defects are well-known to induce lattice strain[166], crystal defects will impact the prop-

erties of NVs[94]. For ensembles of NV centers, the effect of severe strain inhomogeneity is most likely to manifest in the form of broadened ESR lines (large T_2^*) due to the fact that each individual NV experiences a slightly different strain environment, which shifts the lines for each NV. In this section, we will examine the important role that miscut plays in determining the morphology of the growth and the effects of morphological features on NV center ensembles. In addition, we will discuss a model for hillock formation in relationship to step flow and show how high miscuts can suppress hillock formation altogether.

2.3.1 Hillocks and unepitaxial defects

Hillock defects are a type of growth defect so named because they resemble the distinctive mesa-like grassy hills common in Great Britain. These crystal defects are pyramid-like with flat tops (though occasionally they can have points as well)[14]. An AFM image of a hillock is shown in Figure 2.6a) showing a flat-topped hillock.

Figure 2.6b) shows a schematic cross-section of a hillock's structure. The sides of the hillocks are regions of high step density and, based on the argument in the previous section, will have enhanced nitrogen incorporation. Because of the hillock's faster growth rate than the bulk material, nitrogen layers within the hillock will appear at a lower depth than layers outside. The star represents the point-like origin of the hillock. Possible candidates for the origin of the hillock could be screw dislocations as seen in GaN films[167], point defects in the form of contaminants controlled by the plasma as suggested by Tallaire *et al.*[168], or possibly a twin-mediated defect origin where the hillock is nucleated at a twinned crystal formed via a mechanism similar to that seen in silicon growth[169] by the Wagner, Hamilton Seidenstick (WHS)[170, 171] mechanism.

[14]Most often, all the hillocks of a particular growth will look similar. So it is not often that one has flat-topped and pointed hillocks in the same growth.

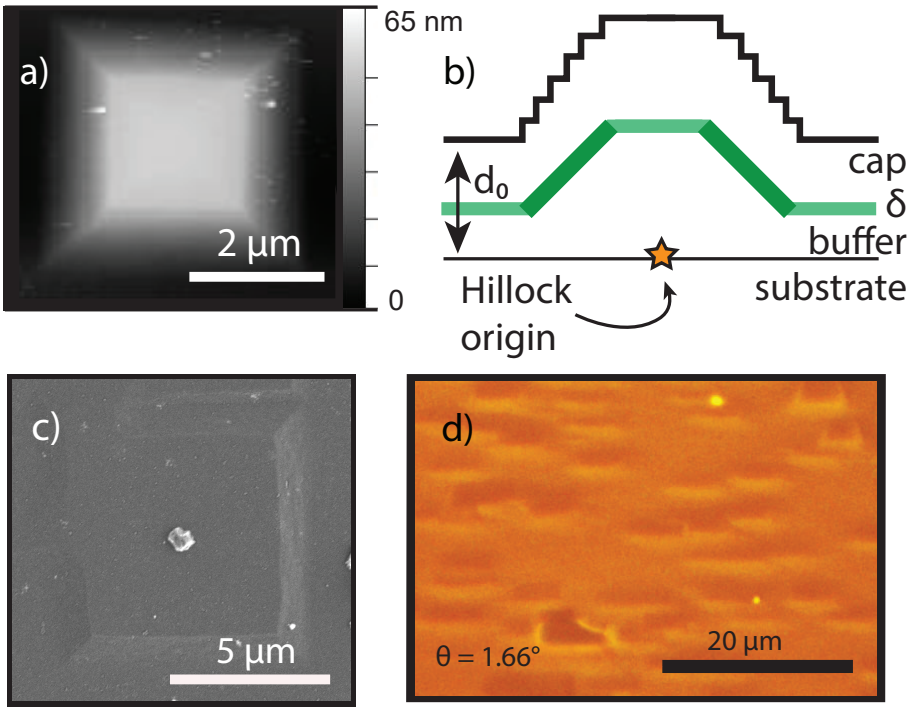

Figure 2.6: a) An AFM of a flat-topped hillock showing a high degree of symmetry. b) Schematic diagram of a hillock. The nominal layer thickness d_0 is different within the hillock due to the faster growth rate. Hillocks likely originate at point-like defects in the diamond, indicated by the star. c) SEM image of a hillock with an unepitaxial defect at the hillock's center. These two defects almost certainly originated from the same point-like origin. d) Optical image showing the morphological features of a high-miscut region of the sample. Step-bunch-like features have developed, resulting in an uncontrolled and rough surface.

An unepitaxial defect is a crystal of diamond that has no set epitaxial relationship with the underlying substrate. These defects are often (roughly) spherical in their proportions and grow much more rapidly than the surrounding epilayer. Evidence supporting the Tallaire[168] mechanism for hillock formation, can be found in the fact that many of the hillock defects have unepitaxial defects at their centers. A scanning electron microscopy image of an unepitaxial defect at the center of one of the hillocks is shown in Figure 2.6c).

One final class of morphological defects that we will discuss are the long, step-bunch-type defect shown in Figure 2.6d). These tend to occur on samples with exceptionally high miscut $\gtrsim 1.5°$. Step bunches will be discussed in a later chapter but are distinct in character from the defects shown here, which appear as a cross between bunches and hillocks. There are still hillocks in this high miscut image (upper right); however, these hillocks have a highly anisotropic appearance due to the high miscut, resulting in material "piling up" on one side of the hillock.

Figure 2.7a) and b) show optical images of a grown diamond sample for two different miscuts. The higher miscut region has a lower density of hillocks. Figure 2.7c) shows the hillock density as a function of miscut for multiple samples.

To explain the dependence of hillock density on miscut, we can invoke a simple model. First, let us assume that hillocks take some time to form into a stable configuration that will grow without bound and let us call this time, T_H. Next, we will assume that hillocks may only form on the flat regions between adjacent steps. This distance between steps is L. If the step has sufficient time to reach the hillock before the hillock can stably form, then the hillock site will be covered by the step, and step flow will proceed normally. However, if the hillock has time to fully form into a stable configuration, it will persist indefinitely because it has a higher growth rate than the surrounding crystal.

If the hillock origin sites are randomly distributed across the step, then the probability

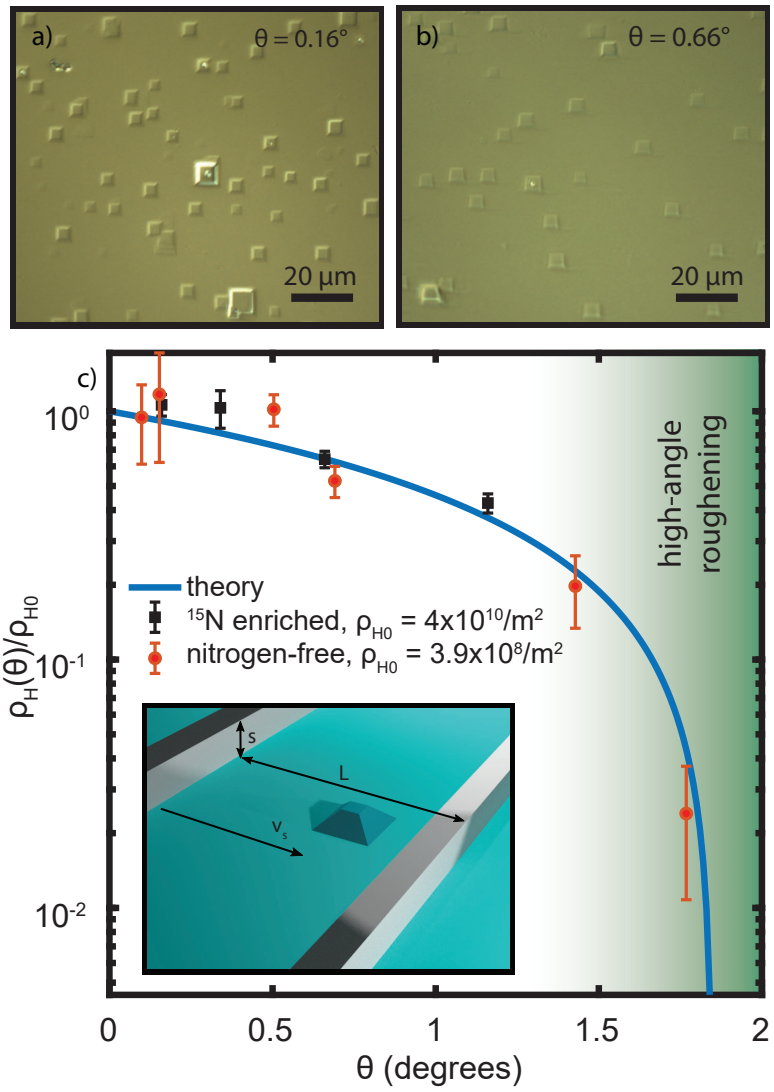

Figure 2.7: Hillock density is intimately related to miscut. a) and b) show optical images of two regions with different miscuts. The lower angle miscuts have a higher density of hillocks. c) The density of hillocks as a function of the miscut. This follows a linear relationship. The inset depicts schematically the reason for the linear relationship; as adjacent steps become closer together (as is the case in high miscut samples), the hillocks no longer have sufficient time to fully form.

that the hillock will form will be given by,

$$P = 1 - \frac{v_s T_H \theta}{s}, \tag{2.5}$$

where s is the step height and v_s is the step velocity. Whether the hillock origin sites appear before growth begins or are the result of particulate matter landing on the surface during growth is only relevant for an overall prefactor [15]. The total density of hillocks, ρ_H, will be given by,

$$\rho_H = \rho_{H,0}(1 - \frac{v_s T_H \theta}{s}), \tag{2.6}$$

where $\rho_{H,0}$ is the total hillock nucleation site areal density.

Interestingly, there is a critical angle at which no hillocks have sufficient time to form. This angle is related to the step velocity, the hillock formation time, and the distance between steps as,

$$\theta_C = \frac{s}{v_s T_h} \tag{2.7}$$

Our data suggests a critical angle of $\sim 1.85°$. Using the step velocity[16] extracted from Figure 2.5b), we obtain a hillock formation time of $\sim 100\,\text{ms}$.

[15] This may not be true for heavily step bunched samples. Time-dependent physics may begin to play an important role because during step bunching, steps tend to aggregate into larger clusters, leaving more space between them. This will result in a larger L as a function of time. However, T_H is only well-defined for a given value of s - i.e., larger values of s result in larger values of T_H. You may think these two competing effects will cancel each other out exactly (because if two steps bunch, L gets twice as big, but so does s). They do not cancel exactly, though, because of the hillock's much faster growth rate relative to the bulk substrate. In summary, I expect that as step bunching becomes a more important effect, higher miscut samples will tend to have more hillocks than expected using the model in this section.

[16] A better estimate for the step velocity could be obtained via a study without nitrogen and a constant growth rate throughout the entire growth. Given the nitrogen apparently affected the growth rate, this estimate may be off by factors of a few. This is intended to be illustrative of the method and to give an order of magnitude estimation.

2.3.2 Nitrogen and NVs in defects

As evidence in figure 2.5c), nitrogen tends to preferentially incorporate along step edges. Because hillocks have an extremely high density of steps around their edges, it is natural to expect that nitrogen incorporation will be enhanced within hillock edges. Figure 2.8a) shows SIMS data on the $\theta = 0.66°$ section of the diamond surface. Two Gaussian peaks are visible. We attribute the first peak to the intentionally doped layer in the bulk. The second peak we attribute to hillock-incorporated nitrogen. Because SIMS averages over an area of $100 \times 100\mu m^2$, we will inevitably have some hillocks within any given scan region. The hillock nitrogen appears deeper than the intentionally doped nitrogen because of the hillock's much larger growth rate relative to the bulk. Despite the hillocks occupying a small area compared to the bulk surface, the peak from defect-incorporated nitrogen is far larger than the intentionally doped peak, suggesting that the incorporation at hillocks is substantially higher than what can be achieved in the bulk. We confirm this using spatially resolved microSIMS co-localized with an optical image of hillocks. In nanoSIMS, the dopant concentration is measured as a function of not just z but also x and y, giving a full 3D map of the constituent materials. Figure 2.8b) shows nanoSIMS data (left) co-localized with an optical image of four hillocks (right). The concentration of nitrogen is substantially higher at the hillocks.

Finally, we consider the properties of NV ensembles within the hillocks. Figure 2.9 shows a confocal image (right) with a co-localized optical image (inset) and optically detected magnetic resonance (ODMR) measurements on three different regions (left). Remarkably, the linewidths within the hillock are comparable to the linewidths of the single NVs in the surrounding area. However, the spectrum of the NVs within an un-epitaxial defect is significantly broadened and disordered, resulting in no clear spectral lines.

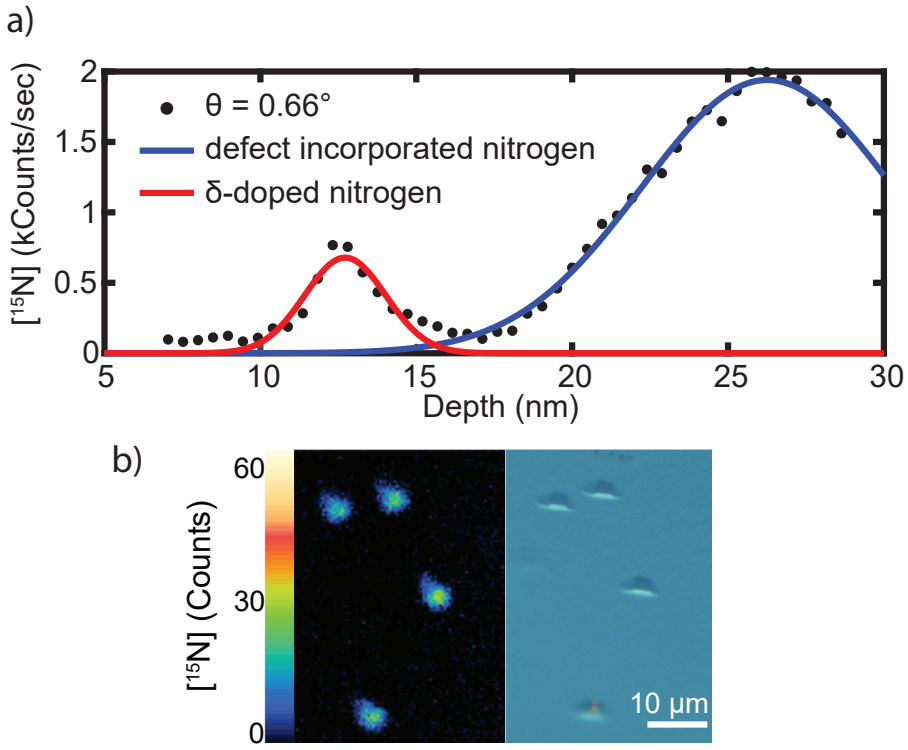

Figure 2.8: a) A SIMS depth profile in the $\theta = 0.66°$ region. The first Gaussian peak is due to intentionally doped nitrogen and the second peak is due to incorporation in defects (mostly hillocks). b) Spatially resolved nanoSIMS data (left) with a co-localized optical image (right). The hillocks have increased levels of nitrogen incorporation relative to the bulk, corroborating the hypothesis that the second, large peak in the depth profile is primarily due to hillock-related incorporation.

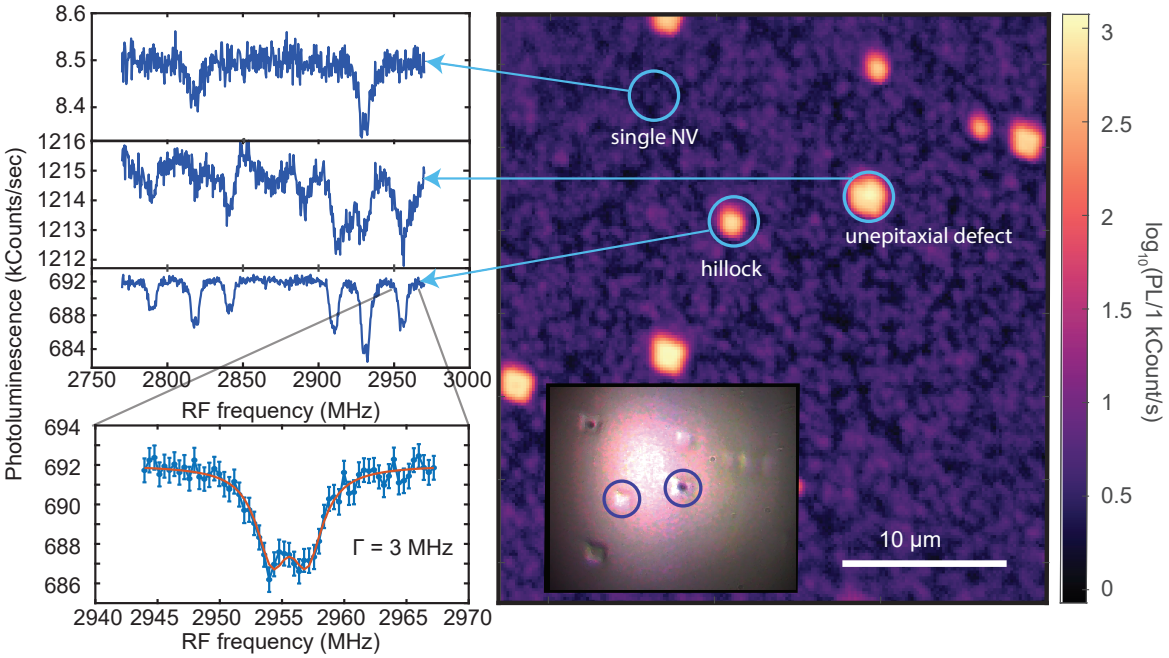

Figure 2.9: Measurements of NV centers inside growth defects in comparison to NV centers grown in the epilayer outside of defective regions. The linewidth of NVs within the hillocks is comparable to the linewidth of single NVs. The NVs within unepitaxial defects show considerably broad and disordered peaks, likely due to an environment of considerable strain inhomogeneity.

Because the ODMR is suggestive of good properties within hillocks, and the density of NVs in hillocks is substantially higher than NVs in the bulk, this opens up the possibility of using hillocks as a means for achieving high-density ensembles of interacting NVs. The nitrogen tends to organize around the edges of the hillock, and so, for sufficiently dense ensembles, it may be possible to treat the "ring" of NV centers as a 1D system with periodic boundaries, opening up the possibility of testing exact theoretical predictions in many-body quantum mechanics for disordered systems. Moreover, confinement to lower dimensional systems leads to the dipolar interactions averaging to different values. For example, in 2D and 3D $\langle 100 \rangle$ grown samples, the dipolar interaction averages to 0, whereas in 1D $\langle 100 \rangle$ samples, in general, it does not (for an extended discussion on this topic, see Chapter 4).

2.4 Conclusions

"Patterned" arrangements of NV centers, even if patterned by nature instead of the experimenter, provide a platform for exploring physics outside of what is normally accessible with homogenous 2D or 3D arrangements. I find the prospect of using hillocks for this purpose to be an exciting one, especially as the system is brought to low temperatures where spin transport lengths may realistically approach the perimeter of a hillock. In a later chapter, we will discuss 1D systems of NV centers arranged along step bunches and the interesting spin-transport and decoherence physics that arises from this special arrangement, but I want to emphasize now that the hillock is not so different from the step bunch. Indeed, it is not unreasonable to imagine that a hillock is very much like a step bunch with periodic boundaries.

Given that, like hillocks, step bunches have enhanced nitrogen incorporation, and both can coexist on the same sample, building qubit networks out of hillock-step bunch

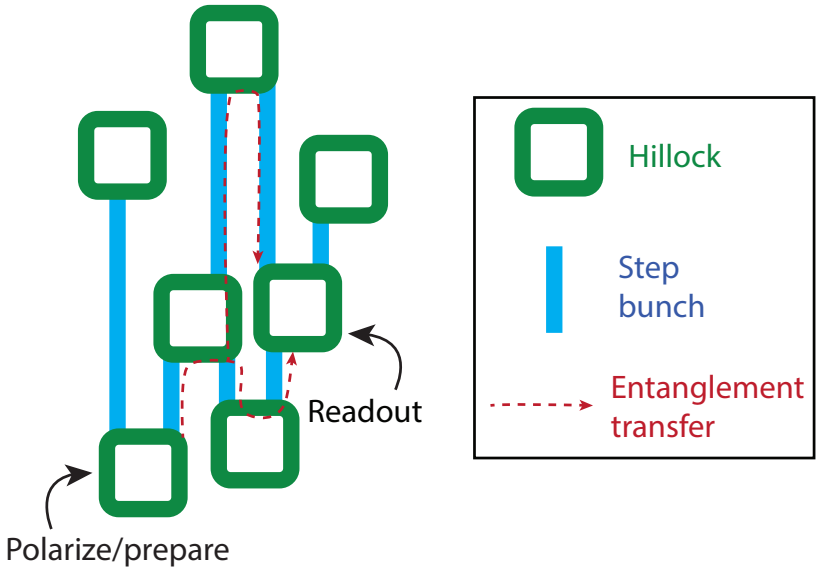

Figure 2.10: A proposal for a hillock-step bunch network. Individual collections of NVs patterned via the hillock edges can be interlinked via long coherence lengths in step bunches (as discussed in a later chapter). State preparation in one hillock (perhaps via hyperpolarization) could naturally transfer to adjacent hillocks via step bunch channels.

intersections seems like an interesting possibility. Figure 2.10 shows a schematic depiction of a possible experiment using this proposed geometry. In this scheme, the hillocks would act as vertices, and the step bunches would act as edges. The hillock NVs would be relatively easy to prepare and initialize into a specific common state; then, the experimenter could wait a set amount of time and measure a different hillock down the chain and infer the transfer of potentially coherent information.

There are some obstacles to realizing this in a grown NV system. First, for the length scales in this problem to be accessible, the hillock size must be small, and the hillock density must be large. Second, the NV density must be very high, and it would be useful to have aligned NVs. The dipole-dipole coupling, which relates the speed at which NVs can entangle with one another to the distance between NVs, is $\sim 52\,\mathrm{MHz\,nm^3}$. For two NVs that are 10 nm apart, this results in a state transfer time of 52 kHz. In

this scenario, for ballistic transfer, it would take 2 ms to entangle two NVs 1 µm apart. At low temperatures, T_1 timescales can approach seconds, so hillock networks are not completely outside the realm of possibility at low temperatures [17]. Moreover, one can also use nitrogen spins (P1 centers) as the medium for entanglement transfer. Nitrogen tends to be substantially more dense than NVs (due to the far-from-unity conversion rate of nitrogen to NV), so higher values of dipolar coupling are generally achieved.

There is an admittedly well-motivated temptation in crystal growth, and indeed, most experimental science, to eliminate phenomena that are hard to explain or control, ugly or otherwise outside of expectation. The hillock falls neatly into this category of "ugly" phenomena. I have presented in this chapter a general method to eliminate them: aiming for an intermediate miscut that is sufficiently high to suppress hillock formation but not so high that uncontrolled step bunching begins to overtake the growth. Indeed, for many applications, perfectly smooth surfaces are desired. For scanning probes assembled out of grown diamond, morphological features on the surface of the probe only serve to weaken the overall spatial resolution. For near-surface NVs designed to be interfaced with deposited spins, morphological features complicate an already exceptionally difficult engineering task. Still, I can't help but root for the hillock. Like the Giant's Causeway in Northern Ireland[172], Saturn's polar hexagon[173], planetary motion[174], or the spiral shell of an ammonite[175], the hillock is a beautiful example of symmetry and patterns arising out of a chaotic, energetic maelstrom (in this case, a plasma). Moreover, it may one day present itself as an underdog platform for yet unrealized configurations of spins, extremely high dopant densities, and nanostructures where the difficult engineering steps are performed by nature itself.

[17] At least for T_1-limited processes like polarization transfer. For coherent quantum state transfer, I think the question is more open. It depends on which channels are determinant in the decoherence - i.e., if all of the decoherence is coming from elements within the network, then it is not truly lost. If it is coming from other sources outside of the network, e.g., surfaces, then it is irrecoverable.

Chapter 3

Three-dimensional systems of NVs

In 1981, in a keynote lecture delivered at MIT at a conference on the *Physics of Computation*, Richard Feynman[176] proposed the idea of a quantum simulator. In this talk, later published as a lightly edited letter[177], Feynman outlines the basic problem of simulating quantum mechanical systems and proposes a solution: using a proxy quantum system (or a quantum computer) to simulate the otherwise intractable quantum system. The problem can be stated very simply; as any undergraduate physics student is well aware, the difficulty in solving the mechanics of a single qubit is manifestly simpler than solving the mechanics of two interacting qubits. As we move to systems of size N, the dimension of the matrix we have to diagonalize (if indeed, we wish to try diagonalization) scales like 2^N. For $N = 37$, the memory required to store the elements of a single Hamiltonian is around 1000 zettabytes[1]. While many-body complexity is certainly present in classical systems, the scaling is made especially heinous in quantum mechanics because of the exponential scaling of the Hilbert space's dimension. Feynman proposed a different approach: quantum computers. This natural yet profound insight spurred the effort to gain insight into natural quantum phenomena through proxy systems, called simulators.

[1]One ZB is 10^{21} bytes. 1000 ZB is probably $\sim 10\times$ more data than the entire internet as of 2020[178, 179], though this number is surprisingly difficult to estimate.

Eventually, experimental control would catch up to Feynman's prediction. These experimental realizations[180] have come in the form of (Rydberg) atoms[181, 182, 183, 20] and ions[184, 185], nuclear spins[186], electronic spins (as in quantum dots)[187], and superconducting circuits[188, 189]. The scope of problems available to quantum simulators is large and includes problems from condensed matter[190, 191, 192, 193, 194, 195, 196], subatomic many-body physics[197], open quantum systems[198, 199], and, notably[2], quantum chemistry[8, 10, 9].

However, an important point must be made about two different types of quantum simulators. The majority of the realizations listed above are performed using so-called "analog" quantum simulators. This class of simulators is close to what Feynman envisioned in his 1981 lecture when he said, "I want to talk about the possibility that there is to be an *exact* simulation, that the computer will do *exactly* the same as nature" [177]. In this mode of simulation, an easy-to-control analogous proxy system is used whose physics is governed by identical (or nearly identical) physics as the less-controlled system under question. This is in contrast to another (potentially easier to scale) type of quantum simulator, called a "programmable" or "digital" quantum computer. These types of quantum networks perform operations, often most easily represented by circuits[3], to simulate the evolution of some qubit or multi-qubit state under a preprogrammed Hamiltonian. The advantage of a digital simulator is that it is versatile relative to the analog variant. The disadvantage of digital simulation is that it is substantially more technically challenging and requires a large number of qubits within a programmable quantum computer.

[2]It seems to me that quantum simulation of problems in quantum chemistry is likely to be a particularly fruitful endeavor, though possibly one of the more technically demanding use cases as well. I say that it seems especially fruitful because a future workflow could be very straightforward. I can imagine future chemists widely using quantum simulation in the same way that DFT is used now. For this approach to be truly scalable, though, I suspect it must proceed via programmable quantum simulation, rather than the analog-based (that is, where one quantum system mimics another) approach.

[3]See Nielsen and Chuang[19] for more information.

In this chapter, we will discuss systems of NVs as platforms for analog quantum simulators. We will focus on 3D ensembles, that is, systems where the density of spins is roughly isotropic and homogeneous throughout the diamond. We will discuss how Floquet engineering can be used as a "control knob" for Hamiltonian engineering in the service of quantum simulation. Finally, we will demonstrate these techniques using a novel pulse sequence designed to characterize the relative abundances of material defects within the diamond.

3.1 Ensembles of NV centers as quantum simulators

The nitrogen-vacancy (NV) center has been used as a basic element in a quantum simulator as far back as 2013, where Cai *et al.*[126] used a network of interacting nuclear spins on the surface of a diamond as the simulated system with the NV centers below the surface as the control element. Since Cai's demonstration, there have been several[127, 200, 201] instances of explicit quantum simulation using the easy-to-prepare NV center as a control element acting as either (or both) a tool for initialization or/and readout.

In this thesis, I discuss two subtly distinct simulation schemes involving NV centers. These two schemes are shown schematically in Figure 3.1. The first scheme, which I call type A, is explicitly using the NV center bath as the simulation medium. In this type, interactions between NVs may be important and modify the NV's Hamiltonian directly. Spins external to the NV bath modify the dynamics of the NV in the form of an imposed, possibly time-dependent field along the z-axis. Type B NV simulation involves using a different spin bath as the simulator and the NV as the readout; in this thesis, the spin-1/2 substitutional nitrogen (P1 centers) will be the simulator bath. For this type, the NV is not intended to participate in the bath dynamics but rather to act as an observer of the dynamics in the "dark" bath of fluctuating spins.

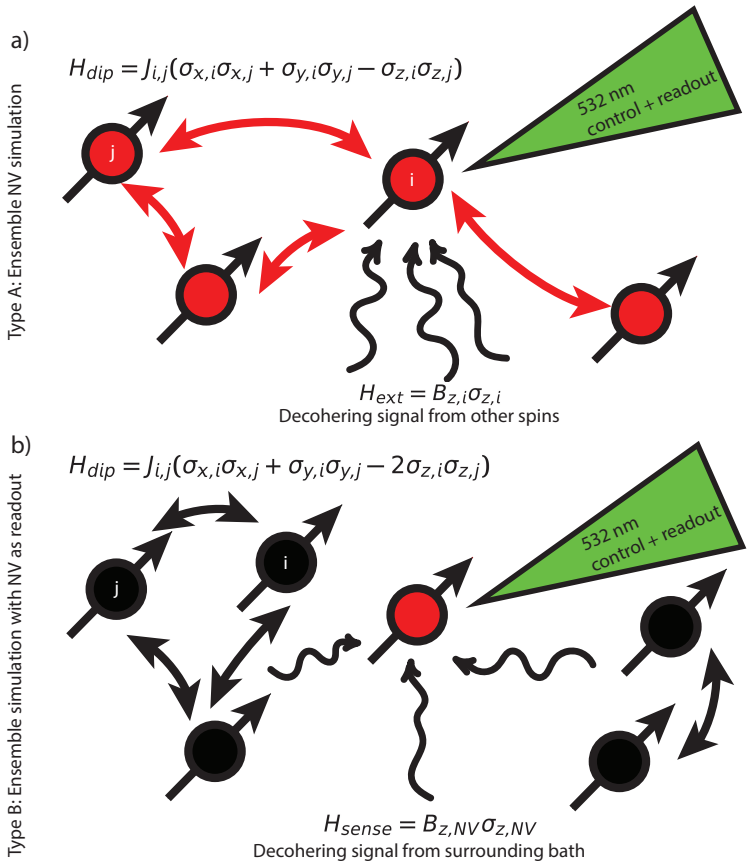

Figure 3.1: A schematic outlining two methods of quantum simulation utilizing ensemble NV centers. a) Type A simulation refers to simulation where the NV centers are both used for control and readout, but also are active participants in the simulation itself. b) Type B simulation refers to simulation where the NV centers act as only tools for control and readout and sense an external bath, which is the object of simulation.

The advantage of type A NV simulation is that the system can be, in principle, perfectly initialized, and global rotations on the bath can be perfectly[4] applied. The disadvantage of type A NV simulation is that the scope of available problems one can simulate is limited: only problems involving spin-1, disordered, and dipole coupled stochastically arranged spins are available, though as will be discussed later on, different arrangements of these spins through their dimensionality provides a surprisingly large array of interesting physics and Hamiltonian engineering can be used to generate a variety of Hamiltonians. Conversely, type B NV simulation provides the experimenter with a much broader array of systems to explore. For example, patterned spinful molecules on DNA origami[202, 203] on the surface of a diamond with shallow NVs would fall into this second type of simulation. The breadboard-like ability to arrange spins in arbitrary configurations opens up a wide range of possible lattice types and spin-spin couplings. In later chapters in this thesis, we will discuss type B simulation, though we will discuss it in the context of an ensemble of NV centers coupled to a bath of P1 centers. The advantage of studying a bath of P1 centers is mainly that the P1 centers are considerably denser than the NVs, and so allow for larger values of spin-spin couplings, J. This chapter will focus on type A NV simulation in the presence of a periodic[204] drive.

3.1.1 The suitability of NV ensemble quantum simulation

NV centers hold promise for quantum simulation because of their access to relatively large numbers of constituent qubits. Further, they are made accessible owing to the relative ease with which one can perform simulation - no vacuum chambers or low-temperature cryostats are required. On top of this, simulating open systems with ensembles of NVs is not only easy but virtually required (which can be an advantage or a disadvantage). NV ensemble quantum simulation is also mainly limited to tack-

[4]Or, as perfect as your pulse engineering allows.

ling problems where disorder plays a large role, although it is possible to engineer order through pulse sequencing. Additionally, as of writing, NV simulation is limited to analog quantum simulation rather than programmable or digital simulation.

3.1.2 The governing Hamiltonian for an ensemble of NV centers

We will derive the Hamiltonian for an ensemble of dipole-dipole coupled NV centers in the presence of a disordered bath of fluctuating external spins (that manifest as fluctuating local fields[5]). First, let us consider the interaction Hamiltonian between NVs. The dipole-dipole operator between spins $\vec{S}_i$ and $\vec{S}_j$ is given by,

$$\hat{H}_{\text{dip},i,j} = \frac{\mu_0 \gamma_i \gamma_j \hbar^2}{4\pi |\vec{r}_{i,j}|^3} [3(\vec{S}_i \cdot \hat{r}_{i,j})(\vec{S}_j \cdot \hat{r}_{i,j}) - \vec{S}_i \cdot \vec{S}_j], \tag{3.1}$$

where μ_0 is the permeability of free space, γ_i and γ_j are the gyromagnetic ratios of the two spins, and $\vec{r}_{i,j}$ is the vector connecting the two spins (and $\hat{r}_{i,j}$ is the corresponding unit vector). This expression is sometimes rewritten in the convenient "NMR Dipolar Alphabet" form with spherical coordinates (r, ϕ, θ), where ϕ is the azimuthal angle and θ is the polar angle. This "Alphabet" expression has the form,

$$\hat{H}_{\text{dip},i,j} = \frac{\mu_0 \gamma_i \gamma_j \hbar^2}{4\pi |\vec{r}_{i,j}|^3} [A + B + C + D + E + F], \tag{3.2}$$

where,

[5] I think it's reasonable to ask how appropriate it is to treat the (in principle) coherent coupling of P1s and NVs in the semi-classical fluctuating field picture discussed in this section. As we will see, this treatment does a good job for large numbers of spins and open systems. As the number of "dark" spins relative to NVs becomes small, or the system becomes highly confined (as we will see in the later 1D chapter), this treatment may be less reasonable.

$$
\begin{aligned}
A &= (1-3\cos^2\theta)S_{z,i}S_{z,j} \\
B &= -\frac{(1-3\cos^2\theta)}{4}(S_i^+S_j^- + S_i^-S_j^+) \\
C &= -\frac{3\sin\theta\cos\theta e^{i\phi}}{2}(S_i^+S_{j,z} + S_{i,z}S_j^+) \\
D &= -\frac{3\sin\theta\cos\theta e^{i\phi}}{2}(S_i^-S_{j,z} + S_{i,z}S_j^-) \\
E &= -\frac{3\sin^2\theta e^{-2i\phi}}{4}S_i^+S_j^+ \\
F &= -\frac{3\sin^2\theta e^{+2i\phi}}{4}S_i^-S_j^-.
\end{aligned}
\tag{3.3}
$$

This form is especially convenient because it allows us to immediately simplify as we invoke the secular approximation. Upon invoking the secular approximation, we can eliminate all the terms that do not commute with the total S_z operator, $S_{z,\text{tot}} = \sum S_{z,i}$. Upon inspection, this only leaves us with A and B. By using $S^+ = S_x + iS_y$ and $S^- = S_x - iS_y$, keeping only A and B, and simplifying Eqn. 3.1, we arrive at the modified dipole-dipole Hamiltonian under the secular approximation,

$$
\hat{H}_{\text{dip}} = \frac{\mu_0\gamma_i\gamma_j\hbar^2(3\cos^2\theta - 1)}{4\pi|\vec{r}_{i,j}|^3}(S_{x,i}S_{x,j} + S_{y,i}S_{y,j} - 2S_{z,i}S_{z,j}). \tag{3.4}
$$

This is sometimes written in the equivalent form,

$$
\hat{H}_{\text{dip}} = \frac{\mu_0\gamma_i\gamma_j\hbar^2(3\cos^2\theta - 1)}{4\pi|\vec{r}_{i,j}|^3}(\vec{S}_i\cdot\vec{S}_j - 3S_{z,i}S_{z,j}), \tag{3.5}
$$

where the $\vec{S}_i \cdot \vec{S}_j$ term is the Heisenberg Hamiltonian. Because the NV center is spin-1, this expression is modified slightly due to normalization factors within the spin-1 S^+ and S^- operators when we write the Hamiltonian in the reduced $m_s = +1$, $m_s = 0$ manifold. Since we are operating in the reduced manifolds, we use the usual spin-1/2

Pauli matrices going forward. These normalization factors (present for any non spin-1/2 system), change this expression in two ways: they change the overall normalization of the prefactor, and they change the relative strength of the $\sigma_{x,i}S_{x,j} + \sigma_{y,i}S_{y,j}$ terms relative to the $\sigma_{z,i}\sigma_{z,j}$ term. The prefactors in front of these two terms are often called J_z and $J_\perp$, such that $J_\perp(\sigma_{x,i}\sigma_{x,j}+\sigma_{y,i}\sigma_{y,j})+J_z(\sigma_{z,i}\sigma_{z,j})$. Thus, for spin-1/2, we have $J_z/J_\perp = -2$ and for spin-1, we have $J_z/J_\perp = -1$. Our NV interaction Hamiltonian can then be written as,

$$\hat{H}_{\mathrm{dip},i,j} = J_{i,j}(\sigma_{x,i}\sigma_{x,j} + \sigma_{y,i}\sigma_{y,j} - \sigma_{z,i}\sigma_{z,j}), \tag{3.6}$$

where $J_{i,j} = \mu_0\gamma_i\gamma_j\hbar^2(3\cos^2\theta - 1)/2\pi|\vec{r}_{i,j}|^3$.

The second part of the Hamiltonian is an on-site random fluctuating field at the NV due primarily to other spins in the lattice. In this treatment, we lump every field from every spin into a single time-varying term, $B_{i,z}(t)$ which is the z-component of the classical field at the position of the i^{th} NV. In this approximation, the dynamics present within the external spin bath are folded into a single correlation time, τ_c, and the field is calculated from summing over the classical dipolar field from an ensemble of spins that fluctuated on a timescale, τ_c. This term has the form,

$$\hat{H}_{\mathrm{dis},i} = B_{i,z}(t)\sigma_{z,i}. \tag{3.7}$$

Putting these together for the ensemble of K spins gives a total Hamiltonian of the form,

$$\hat{H} = \hat{H}_{dis} + \hat{H}_{dip} = \sum_{i}^{K} B_{i,z}(t)S_{z,i} + \sum_{i<j}^{K} J_{i,j}(\sigma_{x,i}\sigma_{x,j} + \sigma_{y,i}\sigma_{y,j} - \sigma_{z,i}\sigma_{z,j}), \tag{3.8}$$

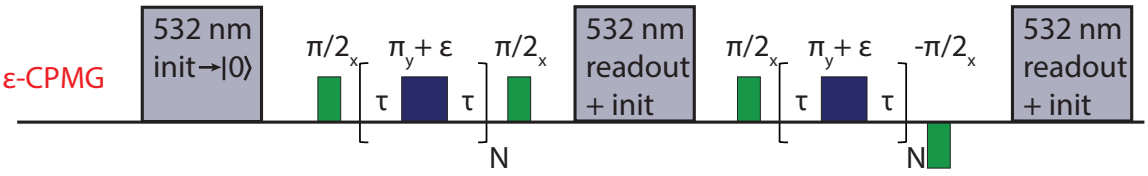

Figure 3.2: Schematic representation of the ϵ-CPMG sequence discussed in this chapter. A green laser is used to initialize the ensemble into a $|0\rangle$ state. Afterwards a $\pi/2$-pulse prepares a $|+y\rangle$ state. We next apply a series of $\pi/2 + \epsilon$-pulses along the y-axis, before mapping the the state on to a population difference with a final $\pi/2$-pulse and a projective green readout. This final readout acts as the initialization for the subsequent pulse sequence. We run the pulse sequence in pairs, with the second pulse sequence using a $-\pi/2$-pulse to measure the state differentially. The values for τ in the two sequences are usually symmetrized to keep the AOM duty cycle constant over an entire measurement (not pictured).

where $\sum_{i}^{K}$ denotes a sum over every spin in the ensemble and $\sum_{i<j}^{K}$ denotes the double sum over pairs of i, j while avoiding double counting. The first term in the total Hamiltonian, $\hat{H}_{\text{dis}} = \sum_i B_{i,z}(t) S_{z,i}$, we will refer to as the "disorder" part and the remaining term, $\hat{H}_{\text{dip}} = \sum_{i<j} J_{i,j}(\sigma_{x,i}\sigma_{x,j} + \sigma_{y,i}\sigma_{y,j} - \sigma_{z,i}\sigma_{z,j})$, we will call the "dipolar" part. For type A NV simulation, this is our native Hamiltonian. Type B simulations will be discussed in a later chapter.

3.2 The ϵ-CPMG sequence

In this section, we will discuss a modified version of the Carr-Purcell-Meiboom-Gill (CPMG) sequence called the ϵ-CPMG sequence and consider the effects of this sequence on an ensemble of NV centers. We will consider the system's evolution through the lens of average Hamiltonian theory (AHT), whereby an effective time-independent Hamiltonian replaces a time-dependent one.

The pulse sequence described in this chapter is called the ϵ-CPMG sequence and

is shown schematically in Figure 3.2. A 532 nm green laser pulse of $\sim 20\,\mu s$[6] is used to initialize the NV ensemble into the $|0\rangle_1 \otimes |0\rangle_2 \otimes ... \otimes |0\rangle_K$ state. Following the initialization, a $\pi/2$-pulse along the x-direction creates the $|+y\rangle_1 \otimes |+y\rangle_2 \otimes ... \otimes |+y\rangle_K$ state. With this y-state prepared, we apply a series of $\pi + \epsilon$-pulses along the y-direction. The rotation angle, modified through ϵ, is controlled by changing the length of the RF pulse; e.g., longer pulses result in larger rotation angles. For the special case where $\epsilon = 0$, this is the conventional Carr-Purcell-Meiboom-Gill sequence[207, 208], which is maximally effective at decoupling disorder. For $\epsilon = \pm\pi/2$, we obtain the Ostroff and Waugh sequence [209, 210]. The Ostroff and Waugh sequence is maximally effective at decoupling dipolar effects in the Hamiltonian. For cases where both dipolar effects and disordered on-site fields are important, we expect an intermediate ϵ to give optimal decoupling.

After the series of $\pi + \epsilon$-pulse, we apply a final $\pi/2$-pulse along the x-axis. Finally, we perform a projective readout with the green laser using a readout time of 400 ns. A copy of the sequence is then performed with the final $\pi/2$-pulse about the $-x$-axis instead to measure the coherence (this allows us to do a differential measurement). Usually, the second copy of the sequence is performed with a symmetrized τ, such that the total sequence time is held constant[7].

3.2.1 Long-lived coherences

We first examine the effects of ϵ-CPMG on an ensemble of NV centers in sample C041, a chemical vapor deposition (CVD)-grown diamond sample. This sample has a

[6]Ensembles typically require much longer initialization times compared to single NV centers. This is not, as is commonly believed, because of absorption in the dense ensemble of NV centers. The absorption cross-section for a single NV is incredibly small[205], and it is easy to check that absorption is playing a minimal role. Still, it is easy to check that ensembles require substantially longer initialization times. My hypothesis for why this is the case is because, for ensemble measurements, you are often still capturing photoluminescence from the wings of the Gaussian. These wings have lower laser power, and so require extra time to initialize. See Section II A in Ref[206] for a discussion of this effect.

[7]This is to keep the AOM duty cycle constant as a changing AOM duty cycle can cause systematic laser power fluctuations during an on-pulse.

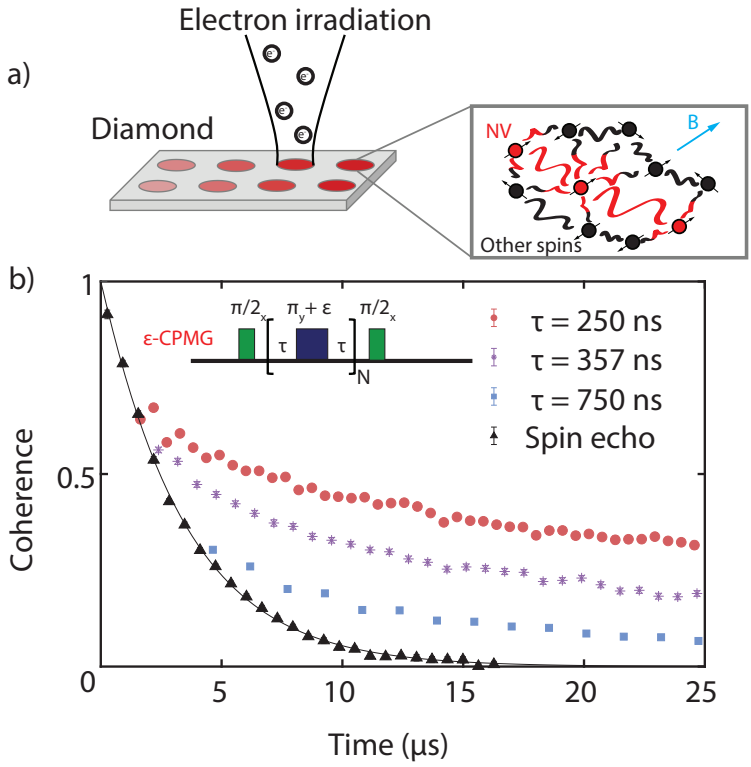

Figure 3.3: Long-lived coherences generated in NV ensembles using the ϵ-CPMG sequence. a) Schematic diagram of the sample, showing multiple electron irradiation spots with varying dosage. Within these spots, systems of coupled NVs and "dark" spins generate the dynamics described in the text. b) Coherence as a function of total sequence time for ϵ-CPMG with three different values of τ with a comparison to a spin echo for reference. In all measurements, $\epsilon = 0$ is targeted, but some amount of finite rotation offset is present and gives rise to the long-lived coherences.

$\sim$ 2 µm thick nitrogen-doped layer and was irradiated in several-µm-scale spots with electrons of varying dosage and energy. Electron irradiation can control the density of NV centers through the dosage of electrons[211, 212], which displace carbon atoms during irradiation, leaving behind vacancies. Upon annealing[8], the vacancies become mobile until they encounter a nitrogen atom (in our case, those within the delta-doped layer).

[8]The vacancies become mobile at $\sim 650°$C. We anneal at $> 800°$C in a forming gas mixture of argon and hydrogen to remove containment oxygen, which will etch the surface. The forming gas is essential (rather than pure argon) because the hydrogen combines with any trace oxygen that leaks in. Ultra-high vacuum annealing (with sufficiently low partial pressures of oxygen) will also result in unetched surfaces.

Spot	Dosage	Energy
A	10^{21} (e^-/cm^2)	200 keV
B	10^{20} (e^-/cm^2)	200 keV
L	10^{22} (e^-/cm^2)	145 keV

Table 3.1: Summary of spot dosages and energies investigated with ϵ-CPMG. We also investigate the background NVs outside of the irradiation spots.

We created several spots of varying NV density to control the strength of dipolar interactions within the same sample, as shown schematically in Figure 3.3 a). Table 3.1 shows electron irradiation dosages and energies for the different spots.

Figure 3.3 b) shows the results of the ϵ-CPMG sequence on spot A for $\epsilon = 0$ (e.g., a conventional CPMG). Varying values of τ are used with the coherence plotted against the total time, $2\tau N$. These are compared to the coherence of a conventional spin echo[23]. The coherence times for the ϵ-CPMG sequence are substantially longer than those for the spin echo. The rest of the chapter will be an in-depth discussion of the mechanisms responsible for the long-lived coherence observed.

Ensembles of NV centers under the ϵ-CPMG sequence have a substantially longer coherence time than those under a conventional spin echo. These long-lived coherences are the result of an ϵ-dependent effective field and will be discussed in detail later. The reasons for the long-lived coherence, even at a target of $\epsilon = 0$, are small uncontrolled errors arising from the following sources:

1. The π-pulse timing accuracy is $\sim 0.5\,\text{ns}$

2. Due to thermal drifts, over the course of a single experiment, the π-pulse time can vary by $0.5 - 1\,\text{ns}$

3. The π time varies over the size of a confocal spot because the RF field from the wirebond varies with distance. This can give a variation of $2\,\text{ns}$ over a confocal

spot.

4. Because our π-pulses have a finite duration, a rotation error of 4° will be introduced.

Given that our total π time for $\epsilon = 0$ is $\sim 46\,\text{ns}$, these four sources result in a total uncontrolled ϵ of $\pm 6^\circ$. Effects 2), 3), and 4) will cause random errors that result in behavior where the measurement is averaged over many values of ϵ distributed over a Gaussian of width 6°. A finite ϵ results in an effective field that points along the y-axis, proportional to ϵ as $\epsilon \to 0$. We will derive the ϵ-dependent effective field in a later section, but we illustrate first the importance of the finite ϵ by comparing ϵ-CPMG to another sequence, ϵ-alternating-phase CPMG (APCPMG).

Alternating-phase CPMG (APCPMG) is a sequence designed to eliminate the effects of rotation offsets by alternating the phase of the π-pulse train in CPMG[213] (that is, alternating between $+\pi$ and $-\pi$ rather than applying only one type). Though APCPMG has the same filter function as CPMG[214, 215, 216], the alternating sign of ϵ due to the alternating phase, negates any effect of accumulating ϵ. The two sequences, ϵ-CPMG and ϵ-APCPMG, are shown schematically in comparison in Figure 3.4 a).

A plot of the coherence as a function of total time is shown in Figure 3.4 b) with a spin echo for comparison. The CPMG coherence persists for substantially longer than during the APCPMG sequence, where it decays on a timescale similar to the spin echo. The similarity between APCPMG and the spin echo indicates that from the perspective of filter function formalism, in the absence of ϵ-related effects, the ϵ-CPMG sequence is identical to the spin echo (though the data indicates that they are dissimilar). Therefore, the extended coherence can not be the result of a narrower filter function because of the additional pulses relative to a spin echo. The inset of Figure 3.4 b) shows the trajectory of the state under rotations for the two sequences to illustrate how APCPMG cancels the effect of finite ϵ. For pulses under ϵ-CPMG, the finite rotation error accumulates

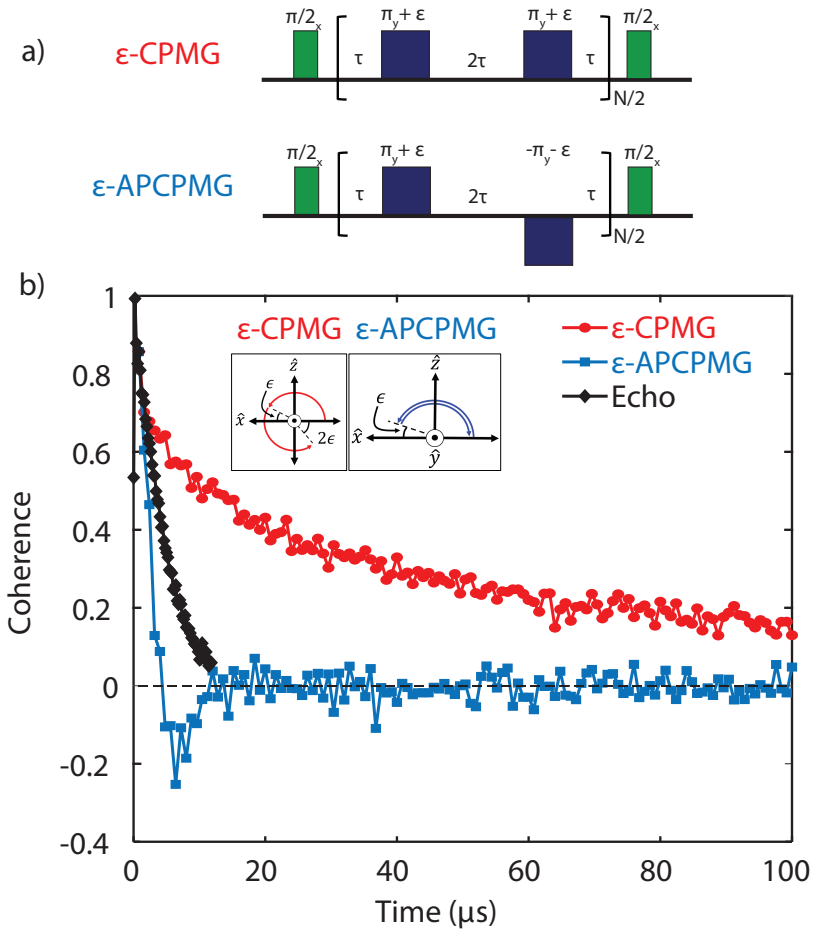

Figure 3.4: A demonstration of the importance of finite pulse rotation offset in the preservation of long-lived coherences with ϵ-CPMG. a) Schematic of the two sequences, ϵ-CPMG, and ϵ-APCPMG. The alternating phase in APCPMG is designed to cancel the accumulating pulse rotation offset, ϵ. b) Coherence as a function of total sequence time for ϵ-CPMG and ϵ-APCPMG compared to a spin echo. In all cases, $\epsilon = 0$ is targeted but some degree of rotation offset persists. The ϵ-APCPMG sequence decays on a similar timescale to the spin echo, indicating the importance of the finite rotation offset for the long-lived coherences in ϵ-CPMG.

with every pulse - for N pulses, there will be an accumulated "extra" phase of $N\epsilon$. For ϵ-APCPMG, for N-pulses, there will only be an accumulated "extra" phase of ϵ, regardless of the total number of pulses.

3.2.2 ϵ-dependence

We next consider the effect of an intentionally introduced finite ϵ and examine the effects of ϵ-CPMG on spots of varying density. Figure 3.5 a) shows confocal images of the three spots described in Table 3.1 and a confocal image of the background NV centers.

Figure 3.5 b) shows the coherence as a function of ϵ for $N = 10$ for each of the different spots and the background. A double-hump feature emerges at intermediate ϵ between 0 and 90°. This can be understood by considering the two limiting cases introduced earlier: the CPMG limit of $\epsilon = 0$ and the Ostroff and Waugh limit of $\epsilon = \pi/2$. Because $\epsilon = 0$ maximally decouples disorder and $\epsilon = \pi/2$ maximally decouples dipolar interactions, when both components are important, then intermediate values of ϵ tend to maximize the ensemble coherence. For the background NVs (BG), the maximum coherence is found at $\epsilon = 0$, as would be expected, given that the NV density is low. As the density of NVs is increased across the three spots, the maximum coherences move outward towards $\epsilon = \pm\pi/2$.

We confirm that the intermediate values of ϵ extend coherence even out to late time by measuring the coherence as a function of ϵ for a variety of values of N across each of the different spots. This data is shown for spot A in Figure 3.5 c). As N is varied, once the accumulated time becomes sufficiently large, the double-hump feature develops and persists. The position of the double hump is related to the relative strength of the dipolar interactions relative to the disorder, i.e., $\langle|J_{i,j}|\rangle/\langle|B_i|\rangle$. The strengths of both terms affect the timescale over which the ensemble decays. This suggests the possibility

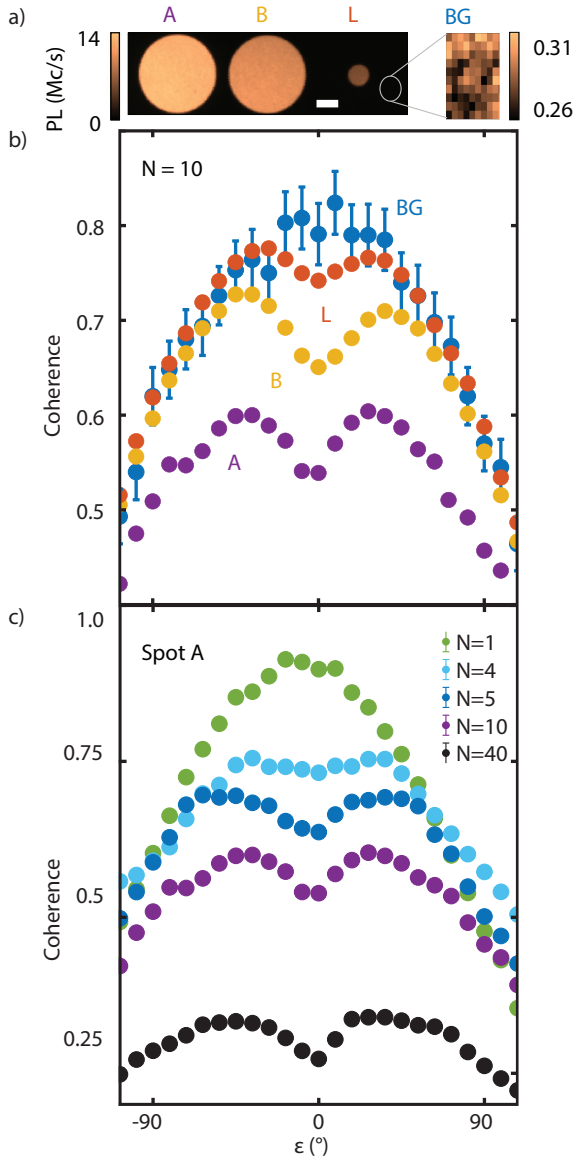

Figure 3.5: a) Confocal images showing the three irradiation spots studied with the background for reference. b) The coherence as a function of ϵ for each of the spots and the background. The double-hump feature emerges because of dipole-dipole interactions within the NV bath. Interpulse spacing is held constant at $\tau = 250\,\text{ns}$. c) Coherence as a function of epsilon for various values of N, showing the overall time dependence of the system. The system approaches the true thermal equilibrium (a fully mixed state) on the spin-locking timescale, $T_{1,\rho}$. Interpulse spacing is held constant at $\tau = 250\,\text{ns}$.

of using this sequence to measure the strength of these terms in the Hamiltonian (which we will discuss in the next section). By measuring the coherence as a function of both N and ϵ, both the relative strengths (through the epsilon dependence) and the overall strength (through the N dependence) can be uniquely determined.

3.2.3 Extracting materials parameters with ϵ-CPMG

In this section, we use the ϵ-CPMG sequence to measure the strength of terms in the Hamiltonian and infer the density of NV centers and other spinful defects (assumed to be P1 centers). While it is possible to quantitatively extract the densities of competing disordered and dipolar spin baths using other methods, a unique determination of these parameters using ϵ-CPMG harbors key advantages, such as technical simplicity, robustness to pulse errors in the form of rotation offsets, and the ability to simultaneously probe NV density and disorder without assuming one to be dominant.

We will briefly describe the other methods for measuring these terms before explaining the method through which we quantitatively extract the strength of the terms in the Hamiltonian. Double electron-electron resonance (DEER) is a widely used technique, developed by Russian chemists Milov *et al.*[217, 218] in the early 1980s that can be used to measure distributions of electron spins[212, 219, 220, 221]. DEER measures total disorder by addressing each individual bath spectrally, but it is hampered by inhomogeneous broadening and fast-varying noise. Because conventional (P1) DEER measures electron spin distances, it can be used to infer the disorder coupling in the NV bath. Measuring dipolar couplings via NV-NV DEER (as opposed to NV-P1) is also possible, but only for high-density ensembles, and requires significant engineering to control the alignment of RF fields with the different NV groups. Instantaneous diffusion (ID) refers to a phenomenon where ensembles of spins dephase faster than expected due to dipolar

couplings within the bath. The rate of diffusion can be used to measure the strength of the dipole-dipole interaction through an extension of T_2 under non-π-pulses. However, techniques relying on this phenomenon cannot easily measure disorder. Other decoupling techniques, such as XY8 or DROID [124], can also be used to measure the strengths of terms in the Hamiltonian but are technically complicated, require arbitrary wave generators and assumptions about the bath. These techniques are not robust to pulse errors in the same way that ϵ-CPMG is *naturally* robust because it exploits pulse errors.

Conversely, ϵ-CPMG does not require complex sequencing (only a string of π-pulses with the same phase) and allows for simultaneous determination of disorder and dipolar coupling. However, our technique does require numerical modeling for quantitative measurement.

The numerical method is summarized below:

- The NVs are initialized in the $|+y\rangle_1 \otimes |+y\rangle_2 \otimes ... \otimes |+y\rangle_K$ state
- The NVs are time-evolved according to the Hamiltonian in Eqn. 3.8. This dynamics are determined by three primary sources:

  1) Dipolar interactions between NVs ($J_{i,j}$)

  2) Larmor precession from local on-site fields determined by the spin-1/2 defects, which can be either +1/2 or -1/2 and have no coherent dynamics

  3) Periodic rotations about the y-axis by an angle of $\pi + \epsilon$ (the ϵ-CPMG sequence).

- Stochastically, with a characteristic correlation timescale, τ_c, each spin-1/2 defect is flipped. This timescale is determined by the density of the bath as described in Ref. [222]. These bath dynamics are crucial to the decoherence dynamics of the

Spot	$[NV]_{ID}$	$[P1]_{DEER}$	$[NV]_{\epsilon-CPMG}$	$[\text{spin-defect}]_{\epsilon-CPMG}$
A	2.7 ± 0.08 ppm	3.8 ± 0.2 ppm	2.1 ± 0.3 ppm	23.2 ± 0.5 ppm
B	2.2 ± 0.21 ppm	10.5 ± 0.2 ppm	1.3 ± 0.4 ppm	17.4 ± 0.9 ppm
L	1.0 ± 0.2 ppm	-	0.6 ± 0.3 ppm	16.1 ± 0.7 ppm

Table 3.2: Comparison of spin densities for spots A, B, and L as obtained from instantaneous diffusion (ID), DEER (Ref. [212]) and from ϵ-CPMG, showing good agreement in the NV density. The fact that the total spin-defect density extracted via ϵ-CPMG is higher than the P1 density extracted via DEER can be explained through the fact that the irradiation can introduce additional defects.

NV centers. Without dynamics, the effect of the spin bath can be exactly canceled for $\epsilon = 0$.

- Finite pulse duration is simulated through a finite $\pi + \epsilon$ rotation time, which is difficult to incorporate in theoretical analyses. For a detailed analysis of the effect of finite pulses, see Ref. [223]

Figures 3.6 a-c) show the data for spots A, B, and L with the numerics plotted with them. Plots of χ^2 for these fits are shown in Figures 3.6 d-e), with the region of best fit indicated by the red, dashed ellipse and the point of best fit indicated by the star. There exists a unique region that clearly minimizes the χ^2 metric. The two free parameters in the numerics are the density of NV centers and the density of spinful defects in the diamond, which control the strength of the dipolar and disorder terms, respectively. For each pair of parameters, we simulate the full coherence dynamics and calculate the χ^2 metric. We compare the dynamics only for $N : N > 3$ because for the first few cycles of the sequence, the details of the initialization are expected to matter - imperfect initialization is not considered in these simulations. Averaging over many spatial configurations of the NV and bath ensemble is essential [224, 225]; otherwise, the dynamics can be heavily influenced by close pairs of NV and spin-1/2 defects.

To benchmark this technique, we compare densities extracted from the numerics in

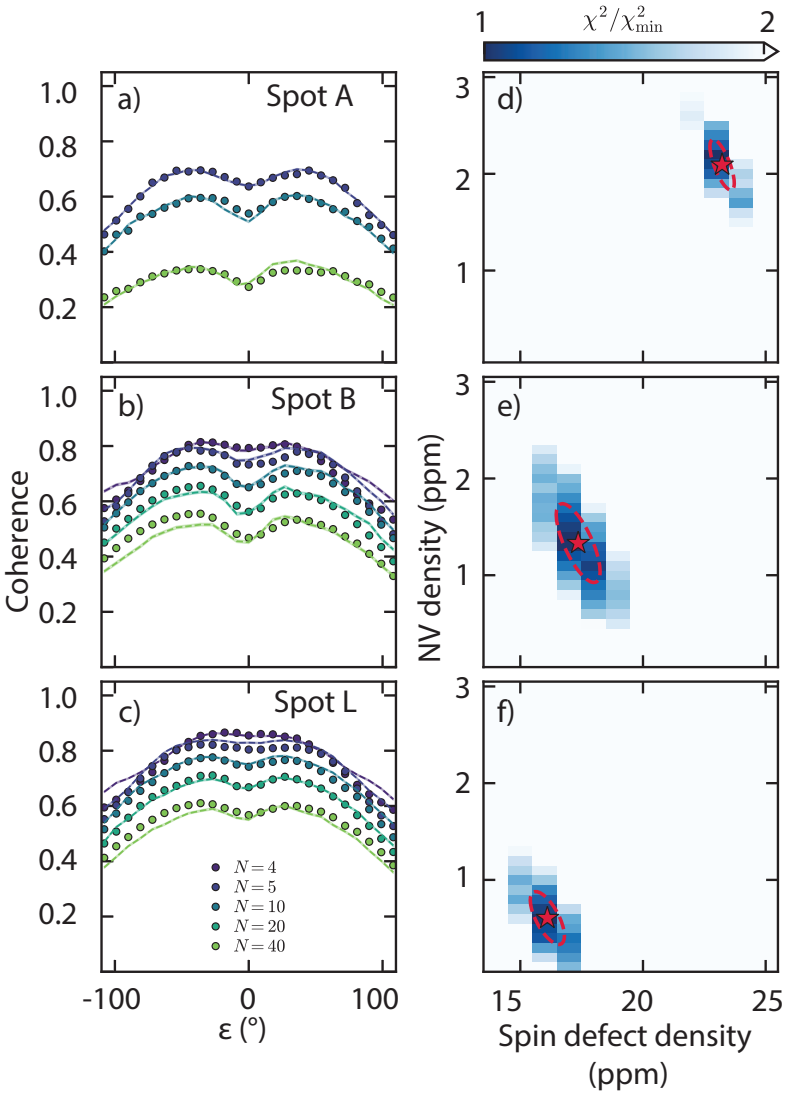

Figure 3.6: Simulations of long-lived coherences. a), b), c): Plots of the coherence as a function of ϵ for spots A, B, and L, each with differing densities. Different values of N are shown. Circles indicate the experimental data and dashed lines are the numerics for the parameters $\{\rho_{NV}, \rho_{\text{bath}}\}$ that minimized χ^2. d), e), f): χ^2 contour plots as a function of ρ_{NV} and ρ_{bath}. The dashed circle shows the region of good fit, and the star indicates the set of parameters used for the dashed lines in a), b), and c).

table 3.2 to those extracted on the same spots with DEER and instantaneous diffusion from Ref. [212]. The NV densities extracted using ϵ-CPMG fall within 1 or 2 standard deviations. The spin defect densities measured via ϵ-CPMG are larger than those measured with DEER on P1 centers, as is expected because ϵ-CPMG measures the total number of spinful defects, whereas DEER is capable of only measuring a specific species. This difference is especially noteworthy in the spot with the highest irradiation dosage, spot A. We confirm the hypothesis that the difference in density can be explained from the presence of other spinful by examining the DEER spectrum for spot A. The spectrum is shown in Figure 3.7. The 1/8 and 3/8 labels indicate groups of ^{15}N P1 centers (there are two nuclear spin states and four Jahn-Teller distortion groups, making 8 species). Labels A and B in Figure 3.7 denote two species with a g-factor of ~ 2, indicating an electronic spin without large hyperfine couplings. The large $g = 2$ peak can only be fit using two Lorentzians, indicating that there are at least two groups of electronic spins affecting the dynamics. Because these peaks are similar in size to the P1 peaks, it is likely that spin-defect density extracted via P1 DEER decoherence would be a large underestimate of the total density (as measured by ϵ-CPMG). These extra spin-defects may be the result of the high irradiation dosage.

3.2.4 Average Hamiltonian for ϵ-CPMG

In this section, we will discuss the qualitative shape of the coherence vs. ϵ and present an analytical treatment using average Hamiltonian theory. The aim of this section is to construct a model described by a single parameter that relates the relative strength of $\langle J_{i,j}^2 \rangle$ and $\langle B_i^2 \rangle$. Extracting the quantitative value for spin densities and NV densities is beyond the scope of the analytic treatment and is best suited for numerics; here we will only obtain the relative strengths. We will fit each of the three spots with the

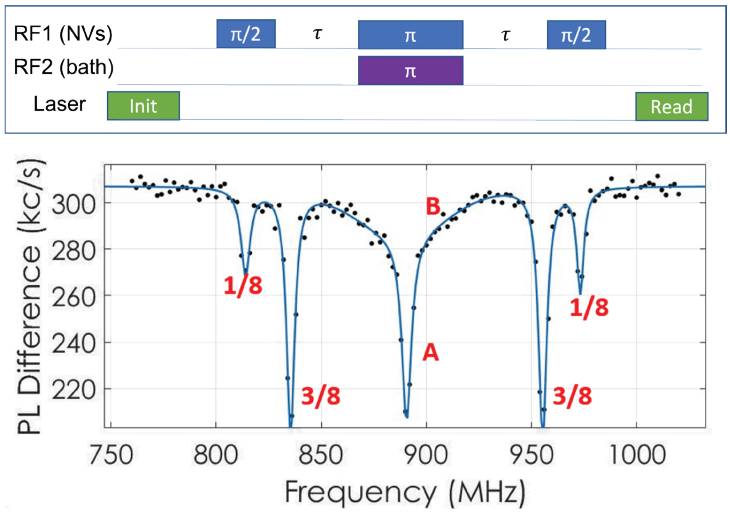

Figure 3.7: Double electron-electron resonance data for spot A. Above shows the sequence for generating the data, and below shows the DEER spectrum. The peaks labeled 1/8 and 3/8 correspond to P1 resonances. The central peaks correspond to $g = 2$ Larmor precession. This peak can only be fit using two Lorentzians and so corresponds to at least two different types of spinful defects. This data corroborates the explanation for the discrepancy in the spinful defect and the P1 densities listed in Table 3.2.

model derived in this section, and we will find the strength of the dip close to $\epsilon = 0$ strongly on the strength of the dipole-dipole coupling, $\langle J_{i,j}^2 \rangle$. We derive an effective, time-independent Hamiltonian by considering the evolution over two cycles. Appendix A discusses two other theoretical approaches, one which considers the evolution over many cycles and derives many terms in the Magnus expansion[226, 227] and another method using the Lindblad formalism[228, 229].

We examine the time-evolution operator over two cycles for the native Hamiltonian in Eqn. 3.8. The time evolution operator consists of the usual time-evolution under a Hamiltonian, $\hat{H}$ for a time τ, where in this case, 2τ is the time between pulses. Each pulse is modeled via a conventional rotation operator, $\hat{R}_y(\theta)$ along the y-axis with an angle $\theta = \pi + \epsilon$. Thus, we write the time evolution for two cycles as,

$$\hat{U}^2 = e^{-i\hat{H}\tau}\hat{R}_y(\pi+\epsilon)e^{-2i\hat{H}\tau}\hat{R}_y(\pi+\epsilon)e^{-i\hat{H}\tau} \tag{3.9}$$

$$= e^{-i\hat{H}\tau}\hat{R}_y(\epsilon)e^{-2i\tilde{H}\tau}\hat{R}_y(\epsilon)e^{-i\hat{H}\tau}, \tag{3.10}$$

where $\tilde{H} = \hat{R}_y(\pi)\hat{H}\hat{R}_y(\pi) = -\hat{H}_{\rm dis} + \hat{H}_{\rm dip}$. The on-site field, B_i^z, is the magnetic field for spin i and, unlike the numerical treatment, is assumed to be time-independent. We use the Magnus expansion[226, 227] and expand about $\epsilon = 0$, because this is the regime where dipolar effects are most pronounced.

The first two terms in the Magnus expansion are given by,

$$\begin{aligned} \bar{H}_{\rm eff}^{(0)} &= \frac{1}{N}\sum_{m=0}^{N-1}\hat{H}_m, \\ \bar{H}_{\rm eff}^{(1)} &= -\frac{\mathtt{i}\tau}{2N}\sum_{m<n}^{N-1}[\hat{H}_m, \hat{H}_n], \end{aligned} \tag{3.11}$$

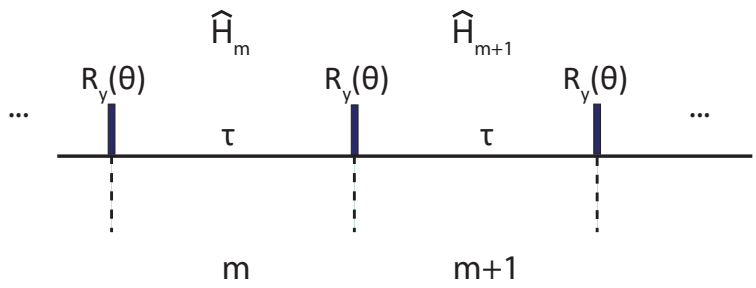

Figure 3.8:

where `i` is the imaginary unit, N is the total number of pulses, m and n are the evolution period index, and $\hat{H}_m$ is the Hamiltonian during the m^{th} evolution period. A schematic showing this for ϵ-CPMG is shown in Figure 3.8.

Our zeroth order term will be given by,

$$\bar{H}_{\text{eff}}^{(0)} = \frac{2\epsilon \sum \sigma_i^y}{4\tau} + \hat{H}_{\text{dip}} = B_{\text{eff}} \sum_i^M \sigma_i^y + \hat{H}_{\text{dip}}. \tag{3.12}$$

Higher order terms will be generated by the commutators between $\hat{H}$, $\frac{\epsilon\sigma^y}{\tau}$, and $\tilde{H}$.

We compute the average coherence along the y-direction for K addressed NV centers. After equilibrating, the coherence, C, will be given by,

$$\begin{aligned} C = \frac{1}{M}\langle \sum_i^M \sigma_i^y \rangle &= \frac{1}{M} \text{tr} \left[\sum_i^M \sigma_i^y e^{-\beta \bar{H}_{\text{eff}}} \right] / Z \\ &\approx \frac{-\beta}{MZ} \text{tr} \left[\sum_i^M \sigma_i^y \bar{H}_{\text{eff}} \right] = \frac{-\beta B_{\text{eff}}}{Z}. \end{aligned} \tag{3.13}$$

We use, $\rho = e^{-\beta \bar{H}_{\text{eff}}}/Z$, where Z is the partition function and β is given by an effective spin-temperature, $\beta = 1/k_B T$. We make the assumption $\beta \bar{H}_{\text{eff}} \ll 1$, that is, the spin temperature is large. The temperature is determined by the initial value of the y magnetization. We relate the initial and final energies through,

$$\sum_{i}^{K} B_{\text{eff}} = \langle \bar{H}_{\text{eff}} \rangle \approx \frac{-\beta}{Z} \text{tr}\left[\bar{H}_{\text{eff}}^2\right]. \tag{3.14}$$

Using Eqn. 3.13 and 3.14, we arrive at the expression,

$$C = \frac{K B_{\text{eff}}^2}{\text{tr}\left[\bar{H}_{\text{eff}}^2\right]}. \tag{3.15}$$

Finally, to arrive at an expression for $\text{tr}\left[H_{\text{eff}}^2\right]$, we examine lowest order terms and expand about $\epsilon = 0$. This results in the following expression,

$$\begin{aligned} \text{tr}\left[\hat{H}_{\text{eff}}^2\right] &= \text{tr}\left[\hat{H}_{\text{dip}}^2\right] + \text{tr}\left[\sum_{i}^{K} (B_{\text{eff}}\sigma_i^y)^2\right] + \\ &\qquad \text{higher order terms} \\ &= K(J^2 + B_{\text{eff}}^2) + \text{higher order terms} \\ &= K(J^2 + D_1^2\epsilon^2 + D_2^2\epsilon^4 + D_3^2\epsilon^6), \end{aligned} \tag{3.16}$$

where $D_{1,2,3}$ are fit coefficients. Using Eqn. 3.15 and 3.16 and simplifying in terms of unique fit parameters, we have:

$$C = \frac{A\epsilon^2}{(J/D_1)^2 + \epsilon^2 + (D_2/D_1)^2\epsilon^4 + (D_3/D_1)^2\epsilon^6}. \tag{3.17}$$

The value of the dipolar coupling $J_{i,j}$, as defined in Eqn. 3.16, diverges for a truly homogeneous ensemble because the spin-spin spacing is allowed to go to zero. In reality, the spin-spin spacing cannot go to zero because the lattice sets a minimum lower bound. While the carbon-carbon spacing might be considered an absolute lower bound (since the

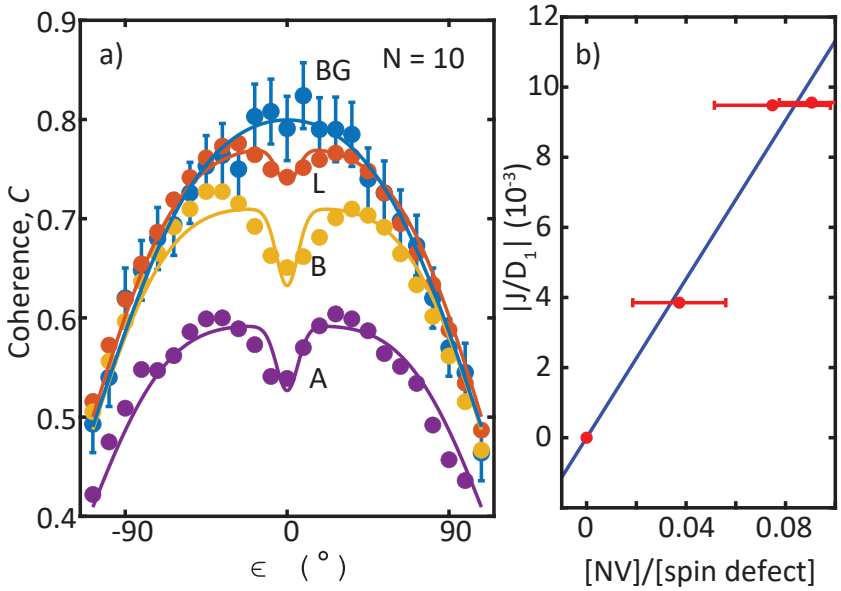

Figure 3.9: a) The coherence as a function of ϵ across different spots, as in Figure 3.5 b). This data is compared to an analytical model (solid line) that parameterizes the curves in terms of J. b) The value of J over another parameter that describes the strength of other terms in the average Hamiltonian (such as disorder), D_1. A comparison of the fit parameter J/D_1 to the ratio of the NV density to the spin defect density obtained via numerical modeling (ϵ-CPMG) in the main text. These have the expected linear relationship.

two spins are not permitted to sit on the same site), the bound is actually higher; when two defects become close on the scale of the lattice, effects from strain, orbital overlap, and charge instability lead to deviations from normal behavior (usually in the form of charge state destabilization or level structure changes). If we impose a $J_{i,j}$ frequency cutoff, these problems are resolved[230, 231, 224, 225].

The fits using the average Hamiltonian model are shown in Fig. 3.9 a) for each of the four regions studied. A Gaussian smoothing with a width of $\sigma = 6°$ to account for the random uncertainties discussed earlier in this chapter smooths the function and leads to a non-zero coherence at $\epsilon = 0$. The parameter (J/D_1) relates the strength of the dipolar contribution to other terms, including B_{eff} and we compare it to the numerically extracted ratio of NV density to spin defect density from ϵ-CPMG. We find that the two

have the expected linear relationship.

Finally, I will spend some amount of time discussing how the time dependence of the analytical treatment fits into the assumptions of thermal equilibrium. Implicit in the treatment above is the assumption that the system has come to thermal equilibrium, but the data clearly depends on N (and thus, time), so, how do we reconcile this? It is not entirely easy. The true thermal equilibrium is a mixed state with zero remaining coherence. We assume the system reaches this true equilibrium on a $T_{1,\rho}$ timescale (the spin locking timescale). However, in the above analysis, we assume that the system reaches a prethermal equilibrium on a T_2 timescale. This can be seen in Figure 3.3 b), where the system decays quickly like the spin echo data until it reaches the long-lived portion where it decays like $T_{1,\rho}$. We assume that the prethermal equilibrium state is the one that the density matrix, $\rho = e^{-\beta \bar{H}_{\text{eff}}}/Z$, describes[9]. At this point, the system is said to depend only on the initial state in the sense that the initial energy depends on the initial state, but all other details are "forgotten". Because time evolution is not taken into account for the analytical treatment, it would not be appropriate to try and fit a single surface across multiple values of N using the techniques presented in this section; we fit only for $N = 10$. Perhaps the thermalization could be treated by using a time-dependent temperature[10], but this is beyond the scope of the present work.

[9]This definition is somewhat circular. We invoke thermal equilibrium when introducing the density matrix in this way but then say that thermal equilibrium is when this density matrix describes the system.

[10]For example, the system of NVs is prepared at an initial temperature, T_{initial} and coupled to an external bath of unprepared NVs at temperature T_{final}. On a timescale of $T_{1,\rho}$, the system approaches thermal equilibrium. For sufficiently fast T_2, the system may be considered at all times to be in prethermal equilibrium.

3.3 Conclusions

I began this chapter with a discussion on quantum simulation in the context of many-body ensembles of spins, and I have ended it with a prescription for determining the densities of various defects in diamond. A reader could be forgiven for wondering about the connection between these two concepts and why I made the deliberate choice to discuss quantum simulation at the start of the chapter instead of, say, an introduction to methods for determining defect densities or some other more materials-focused introduction. I want to clarify that here before moving on to my closing thoughts on the sequence demonstrated in this chapter.

While the ϵ-CPMG sequence provides an easy-to-use method for determining densities of defects, my perspective is that the especially exciting part of the results presented in this chapter are the tests of many-body quantum mechanics theory. At present, there are no methods to analytically or computationally solve the dynamics for thousands of disordered spins, all of which may be coupled to each other - the Hilbert space is simply too large. Because of this, theoretical technique development is required to understand the evolution of real systems and how these systems approach thermal (or prethermal) equilibrium. Moreover, these theoretical techniques all require simplifying assumptions to be made tractable, and so, these assumptions require tests against experiments. Requisite control over quantum systems with large numbers of constituent qubits is very recent, so the space for testing many-body quantum mechanics is ripe. The techniques and results presented here are only a small step toward answering how to predict many-body quantum behavior in a large (and growing) community. We have tested and benchmarked two different approaches for predicting the behavior of disordered quantum systems, both a semi-classical numerical treatment and a thermal analytical treatment.

Additionally, the ϵ-CPMG sequence (like many Floquet sequences) allows the ex-

perimenter to engineer the Hamiltonian. In our case, we can introduce a field along the y-direction controlled via a single, simple parameter in an XXZ-type Hamiltonian. Here, the applications for quantum simulation are made clear. As more pulse sequences are developed, so too is the space of available Hamiltonians made larger. Using systems of NVs (or other spins) as test beds for many-body dynamics under specific Hamiltonians will become increasingly accessible as the appropriate theoretical treatments and pulse sequence engineering are further developed. For example, one can add additional parameters to the ϵ-CPMG sequence, such as pulses along both x and y with correspondingly different values of ϵ, i.e., ϵ_x and ϵ_y or, as will be discussed in the next chapter, via dimensional engineering, geometric constraints can be placed on spin ensembles allowing for the creation of entirely new phases.

Chapter 4

Lower dimensional systems of NVs

Though the term "arrow of time" was coined in 1927 by Arthur Eddington[232], the relationship between the time-reversal symmetric laws of classical physics and the apparent time-reversal-symmetry breaking of natural systems (and thermodynamic theories) was well-understood before then. The answer to the question of how microscopically time-reversible mechanisms give rise to macroscopically time-irreversible phenomena came with the development of the *particularly* beautiful theory of thermostatistical mechanics[233], developed in large part by James Clerk Maxwell[234, 235] and Ludwig Boltzmann[236, 237][1]. The ergodic hypothesis, that is, the amount of time that a system spends in some region of a phase space is proportional to the volume of that region, is key to how time irreversible phenomena emerge. At long times, for ergodic systems, every microstate of the system will be explored equally often.

However, there is a corollary here: non-ergodic systems may defy thermalization.

[1]I do not mean to discount the contributions of other pioneering physicists in the field of statistical and thermal physics, like William Thomson (Lord Kelvin), and Josiah Gibbs. Rather, in this section, I wish to draw special attention to Maxwell and Boltzmann because both were especially concerned with answering the question of how macroscopic time irreversibility emerges from microscopically reversible laws. Boltzmann, in particular, spent a great deal of time on this question and has a series of lectures published late in his life that answer the question in a clear and cogent manner[236]. See the sections in chapter VII, especially section 89: *Relation to the second law of thermodynamics*.

One particularly striking example of a non-ergodic[2] system is a permanent magnet, i.e., a ferromagnet. Ferromagnets[3] are kept from ergodically exploring their full phase space by large energy barriers.

Quantum systems also obey fundamentally time-reversible laws[4], and so a natural question to ask is whether it's possible to engineer quantum systems that resist thermalization. The means by which quantum systems approach thermalization is itself a rich area of study[238, 239, 240], but beyond the scope of this section. Instead, I will briefly discuss one method to achieve athermal behavior: many-body localization. In 1952, American physicist Philip Anderson proposed a disorder-mediated mechanism[241] through which quantum systems would never thermalize. Anderson proposed that transport on a disordered lattice could be halted entirely; this would later become known as Anderson localization. In contrast to periodic potentials, which give rise to Bloch functions[242] as their solution, low-density, disordered lattices permit only highly localized electronic states. Figure 4.1a) and b) show a comparison between a periodic lattice and a Bloch state that has a periodic character. In contrast, for a disordered lattice, as shown in b), the electron occupies only a single site (and the probability of finding that electron away from the site decays exponentially.

In Anderson's seminal paper[241], he mapped the problem of a particle wandering on a disordered lattice to spins diffusing in a disordered, dipolar system. This problem is usually distinguished from the problem of low-density particle problem through the term "many-body localization" (MBL)[243, 244, 245, 246, 247, 248, 249, 250, 251]. MBL is a phenomenon highly related to conventional, low-density Anderson localization. Rather

[2]Not ergodic on human timescales.

[3]There is a deep connection between the spontaneous time-reversal symmetry breaking of ferromagnets and their non-ergodicity.

[4]A little bit of care is appropriate here. Wavefunction collapse, as in the Copenhagen interpretation, is not time reversible. An Everett interpretation would state that measurement is only apparently irreversible. In any case, unitary Hamiltonian evolution sans measurement is reversible.

than treating a single particle navigating around a disordered landscape, we can instead consider spin excitations in an interacting dipolar ensemble[250]. Figure 4.1 c) shows a 1D chain of spins. In this example, spins i and j will be coupled like $J_{i,j}\hat{\sigma}_i\hat{\sigma}_j$ such that the total Hamiltonian is given by,

$$\hat{H} = \sum_{i<j} \delta_{j-1,i} J_{i,j} \hat{\sigma}_i \hat{\sigma}_j, \tag{4.1}$$

where the Kronecker delta, $\delta_{j,i}$, is included to ensure only nearest neighbor couplings are counted[5]. The energy associated with flipping spin i, $\hat{\sigma}_i^-$, will be, $\Delta E = 2(J_{i-1,i} + J_{i,i+1})$. Suppose we prepare all the other spins into the state $|\uparrow\rangle$ and introduce a single excitation, $|\downarrow\rangle$ at site i. In that case, that excitation can diffuse left and right only through the operators, $\hat{\sigma}_i^+\hat{\sigma}_i^- - 1$ or $\hat{\sigma}_i^+\hat{\sigma}_i^- + 1$. These will have an energy cost of $\Delta E = 2(J_{i-2,i-1} + J_{i,i+1})$ or $2(J_{i-1,i} + J_{i+1,i+2})$ respectively. Suppose the elements $J_{i,j}$ are drawn from a random distribution. In that case, the spin excitation can be treated as though it is traversing a disordered energy landscape whose local energies are set by the nearest neighbor J-couplings.

Dimensionality plays an important role in spin systems, an idea that goes as far back as Ernst Ising's now legendary thesis, published (in part) as a short article[252] in 1925. Ising showed that no phase transition or spontaneous ferromagnetism can exist for spin systems in one dimension. Much later, in 1944, Lars Onsager would exactly solve the Ising model in two-dimensions[253] and show that for 2D systems, Ising's model *did* yield a phase transition. Localization is also strongly affected by dimensionality[254]. True Anderson localization is prohibited in systems of dimension larger than two[248]. Because interactions are strongly affected by dimensionality, mechanisms for decoherence

[5]Though Anderson considered dipolar $1/r^3$ interactions, he found that in the $1/r^3$ limit transport was slow, though could still occur. For interactions falling off faster than $1/r^3$, however, he found that localization could occur.

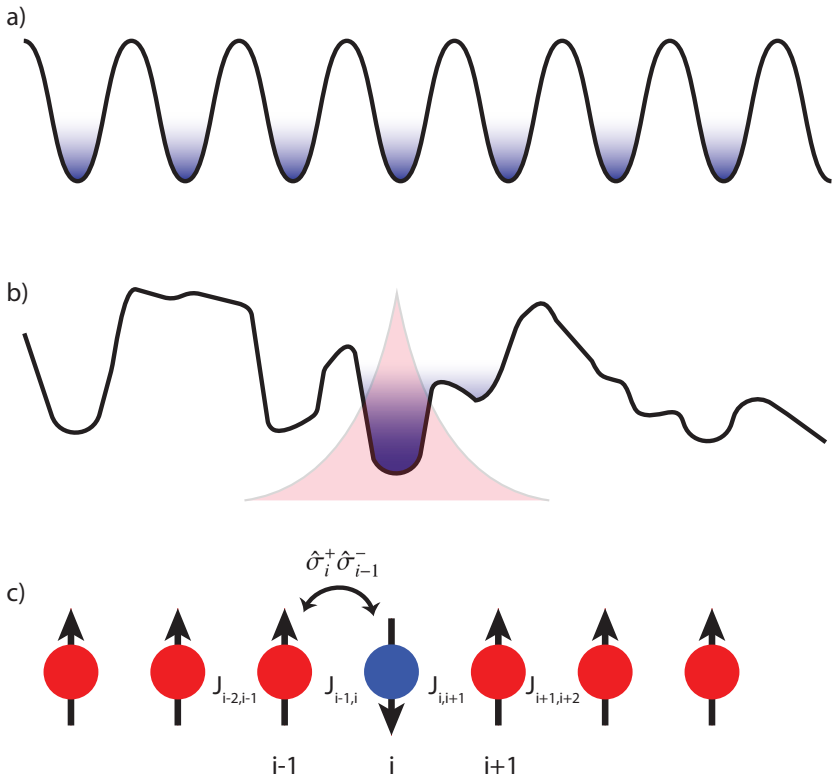

Figure 4.1: a) A periodic potential results in periodic wavefunctions known as Bloch states of the form $\psi(\vec{r}) = e^{i\vec{k}\cdot\vec{r}}u(\vec{r})$, where $u(\vec{r})$ is a periodic function of position, $\vec{r}$, where the function has the same periodicity as the lattice. b) In potential landscapes that are disordered, for systems with a low density of particles, electronic wavefunctions may become localized. c) Many body localization can occur in disordered dipolar systems. In this case, spin excitations traversing the dipolar system behave like a particle traversing a disordered energy landscape.

are similarly strongly affected[255, 256]. Additionally, the confinement of spin ensembles to lower dimensions can open up new phases[257, 258] because, for example, the expected value of the dipolar interaction can change dramatically across different dimensionalities. Consider two classical magnetic dipoles in an isotropic 3D bath, $\vec{m}_1 = \vec{m}_2 = m(0, 0, 1)$ connected by an arbitrary vector, $\vec{r} = r\hat{r} = r(\cos\phi \sin\theta, \sin\phi \sin\theta, \cos\theta)$. Figure 4.2 a) shows a schematic illustration of this. In the examples discussed here, every spin points along the same axis because this is realistic for the ensembles discussed in this thesis, as the externally applied magnetic field will set the quantization axis. The energy of these two spins will be given by,

$$U(r, \theta, \phi) = -\frac{\mu_0}{4\pi r^3}(3(\vec{m}_1 \cdot \hat{r})(\vec{m}_2 \cdot \hat{r}) - \vec{m}_1 \cdot \vec{m}_2) = f(r)(3\cos^2\theta - 1), \tag{4.2}$$

where $f(r) = -\mu_0 m^2/4\pi r^3$ is introduced for notational simplicity.

Taking the integral over 4π steradians gives,

$$\int_0^{2\pi} \int_0^{\pi} f(r)(3\cos^2\theta - 1)\sin\theta \; d\theta d\phi = 0. \tag{4.3}$$

We next examine the case of a 2D ensemble of spins organized in the xy-plane. For NVs in 001 diamond, all of these spins will point along the $[1, 1, 1]$ axis in the coordinate system shown in Figure 4.2 b). Here, our dipolar energy will be given by,

$$U(r, \phi) = f(r)((\cos\phi + \sin\phi)^2 - 1), \tag{4.4}$$

and integrating it over 4π steradians, we find,

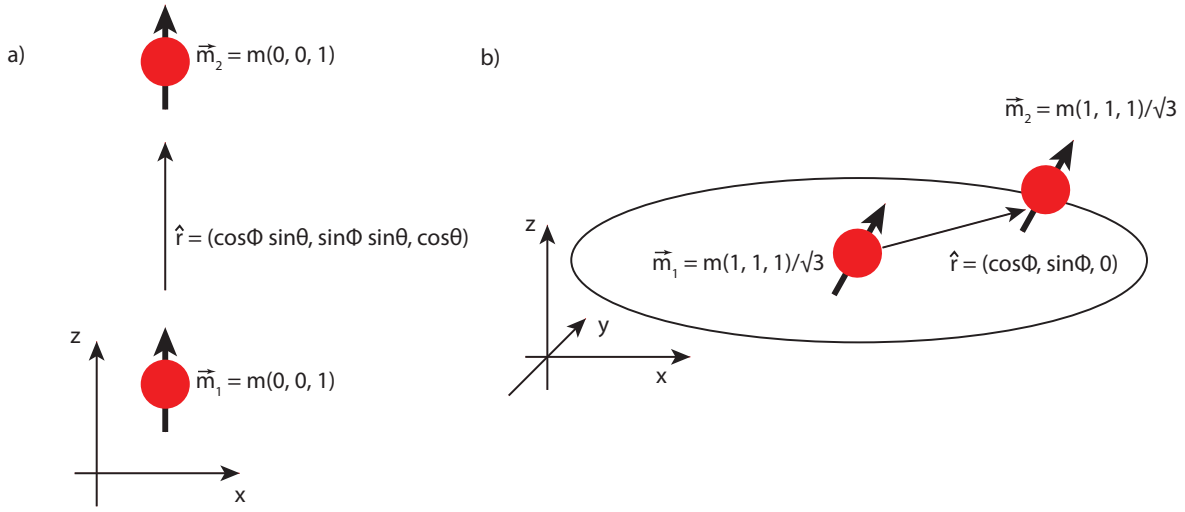

Figure 4.2: Schematic showing two different types of dipolar ensembles. a) The average value of J in a 3D ensemble can be found by integrating Eqn. 4
over 4π steradians. For a 3D ensemble, $\langle J \rangle = 0$. b) A two-dimensional ensemble may have non-zero or zero $\langle J \rangle$ depending on the orientation of the spins with respect to the plane. For 100 diamond, $\langle J \rangle = 0$, but for other orientations (such as 111), it is non-zero.

$$\begin{aligned}
&\int_0^{2\pi}\int_0^{\pi} f(r)((\cos\phi+\sin\phi)^2-1)\delta(\theta-\pi/2)\sin\theta\ d\theta d\phi,\\
&=\int_0^{2\pi} f(r)((\cos\phi+\sin\phi)^2-1)\ d\phi = 2f(r)\int_0^{2\pi}\cos\phi\sin\phi\ d\phi = 0,\\
&\Rightarrow \langle J_{i,j}\rangle = 0.
\end{aligned} \tag{4.5}$$

We understand the averaging here to be a configurational averaging over an isotropic and uniform density confined to the plane where the Dirac delta function $\delta(\theta)$ is included to account for the spins being confined to the xy-plane. In both the 3D isotropic case and the 2D 001 sample case, the dipolar interactions have a net zero value. Interactions averaging away in 2D is only true for the special case of 001 samples, where the NVs sit at a "magic angle" of 54.7356° with respect to the plane. For samples grown along the 111-axis, the interactions *do not* average away.

If we repeat the same calculation as Eqn. 4.5 but with the spins aligned along the plane normal (the z-axis), we get a dramatically different result. In this case, $\vec{m}_1 = \vec{m}_2 - m(0,0,1)$, and,

$$U(r) = f(r)(3\cos^2\theta - 1) = -f(r), \tag{4.6}$$

and when we integrate this,

$$\begin{aligned}
&\int_0^{2\pi}\int_0^{\pi} f(r)(3\cos\theta-1)\delta(\theta-\pi/2)\sin\theta\ d\theta d\phi,\\
&=-f(r)\int_0^{2\pi} d\phi = -2\pi f(r)\neq 0,\\
&\Rightarrow \langle J_{i,j}\rangle \neq 0.
\end{aligned} \tag{4.7}$$

Thus, for a 2D layer of spins, all of which are pointed along the plane normal, the spin-

spin interaction is not only on average non-zero but is also the same sign for every single pair of spins. The dramatic differences between these cases suggest using dimensionality as a tool to access radically different regimes of dipolar coupling.

This chapter will discuss two different (but closely related) methods of dimensional engineering: delta-doping and patterning via step bunches. The first part of this chapter will focus on 2D ensembles and the ways in which lower dimensional systems decohere differently than their higher dimensional counterparts. The second part of this chapter will focus on 1D ensembles. Here, I will propose a new method for achieving one-dimensional ensembles of dipolar coupled spins, and we will discuss the interesting new physics available for these 1D systems. Finally, we will use these 1D systems as a proof of concept for a new type of *in-situ* technique to measure morphology during growth.

4.1 Dimensional engineering via crystal growth

Dimensional engineering, as I use it in this thesis, refers to the deliberate patterning of systems of spins within confined geometries. In other words, while the spins occupy a 3D space, their density is a function of space in the following way,

$$\begin{aligned} &\text{3D} : \rho(x,y,z) = \rho_{0,\text{3D}} \\ &\text{2D} : \rho(x,y,z) = \delta(z)\rho_{0,\text{2D}} \\ &\text{1D} : \rho(x,y,z) = \delta(z)\delta(y)\rho_{0,\text{1D}}, \end{aligned} \tag{4.8}$$

where $\delta(x)$ is the Dirac delta function. Because the Dirac delta function is unitful, simple inspection here reveals that $\rho_{0,\text{1D}}, \rho_{0,\text{2D}}$, and $\rho_{0,\text{3D}}$ must all have different units. If we report our volume density[6] in terms of ppm, for 2D systems, the meaningful density

[6]The ppm unit is a strange one, so I will spend some time here discussing it. Strictly speaking, in

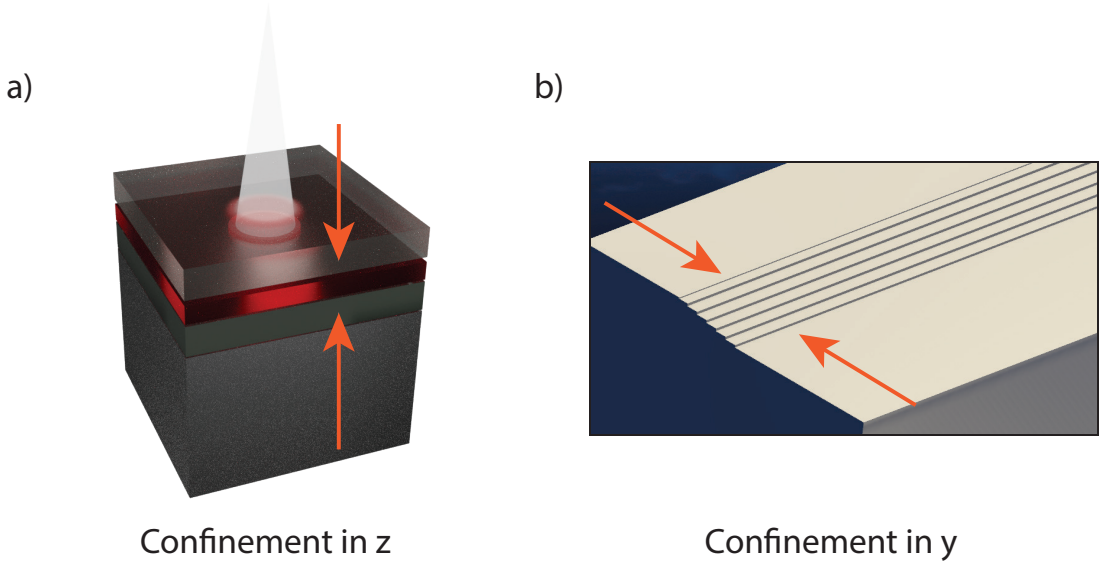

Figure 4.3: Two distinct methods for achieving dimensional confinement. a) Delta doping during growth can confine a spin ensemble in z. b) Preferential incorporation at 1-dimensional defects, such as step bunches, can allow for lateral confinement. Combining these two strategies can result in 1D ensembles of spins.

has units of ppm∗nm, and for 1D systems, ppm∗nm^2.

In this section, two different strategies will be discussed to realize 2D and 1D confinement in delta-doped, CVD-grown diamond. The method to realize a 2D system of spins is conceptually very simple: during the doping step, turn on the nitrogen for a very limited amount of time - this will give us confinement along the growth direction (z). Subsequent electron irradiation, as described in Chapter 3, can create dense ensembles of NVs within this doped layer. This z-confinement is illustrated in Figure 4.3

most contexts, parts-per-million is a dimensionless unit designating fractional constituency. However, in a doping context (especially in the NV literature), it is often treated as dimensionful number density (with units of 1/[L]). To convert between ppm (in the diamond literature) and volume density in SI units, one must know the lattice constant of diamond. In this context, ppm is defined as $1/V_{1e6}$, where V_{1e6} is the volume occupied by one million atoms. In this footnote, I will clarify conversions between the two units: $1\,\mathrm{nm}^{-3} = 5674.2$ ppm. The implication is we now have a rather strange unit of length, $\mathrm{ppm}^{-1/3} = 17.8\,\mathrm{nm}$. In this thesis (and elsewhere in the NV literature), people will commit the act of mixing both units together and report lower dimensional densities in terms of ppm nm (for 2D) and ppm nm^2 (for 1D). For completion: 1ppm nm $= 1.76 \times 10^{-4}\,\mathrm{nm}^{-2} = 0.0562\ \mathrm{ppm}^{2/3}$ and 1ppm nm^2 $= 3.106 \times 10^{-8}\,\mathrm{nm}^{-1} = 3.16\mathrm{E}{-3}\ \mathrm{ppm}^{1/3}$.

a). Confinement along the y-direction via a novel technique will be demonstrated later in this chapter. This technique relies on the preferential incorporation of nitrogen into step edges, as described in Chapter 2. We will use a heavily step-bunched sample as a template onto which we can pattern striations of nitrogen. An example of a step-bunch is shown in Figure 4.3 b). Combining both techniques will give confinement along y and z, resulting in the 1D density described in Eqn. 4.8.

4.1.1 Delta-doping for z-confinement

We will use delta-doping to create ensembles of 2D interacting dipoles. An example of a secondary ion mass spectroscopy (SIMS) data set demonstrating 2D confinement is shown in Figure 4.4. We grew this sample, S011, with isotopically purified methane (99.999% ^{12}C) as described in Chapter 2 and Refs [88, 139, 141]. For the delta-doping step, we introduced natural abundance nitrogen gas at 5 sccm and for 10 minutes. We chose relatively large buffer layers ($\sim 125\,\text{nm}$) and capping layers ($\sim 275\,\text{nm}$) to remove confounding effects from both the sample surface and the isotopically impure substrate. To create vacancies and NV centers, we used a transmission electron microscope (as described in Chapter 3 and Refs [211, 212] and an argon forming gas anneal at 850°C for 6 hours.

The SIMS data in Figure 4.4 shows an approximately Gaussian peak at the desired depth, whose width is found to be $\leq 8\,\text{nm}$. This width estimate is only an upper bound because SIMS cannot measure peaks that are narrower than the RMS roughness of the sample surface and is confounded by other effects related to the speed and energy of ablation - these two factors result in a SIMS resolution for this sample of $\sim 8\,\text{nm}$. To assess whether this is sufficiently narrow to produce confinement effects, it is useful to compare this measure to other geometric scales in the problem, for example, the mean

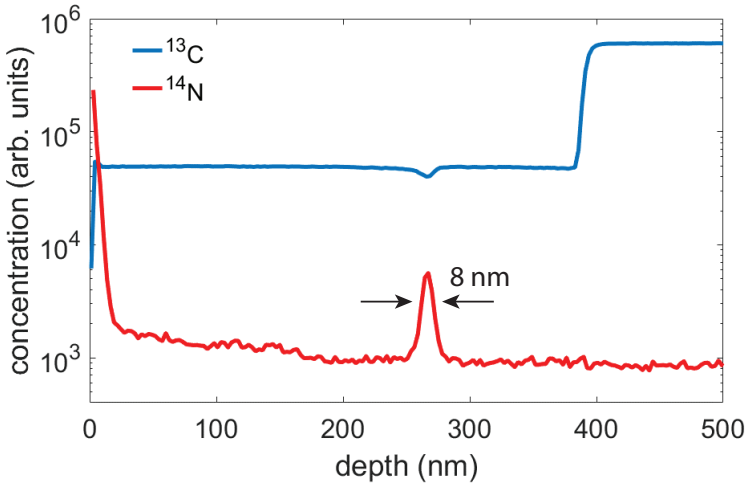

Figure 4.4: Secondary ion mass spectroscopy data for sample S011. The $\sim 275\,\text{nm}$ nitrogen peak is $< 8\,\text{nm}$ and is likely broadened from artificial broadening introduced by SIMS.

spin-spin spacing. For diamond, a useful number to remember is that for 1 ppm of dopants, the average spacing will be 17.8 nm, and the spacing will scale like the inverse cube-root of the density. The 3D NV density for sample S011 is 3.2 ppm[255], which results in a mean spacing of 12.1 nm - above the upper limit of the layer thickness and placing the NV ensemble well-within the 2D regime. The 3D P1 density for sample S011 is 14 ppm[255], resulting in a spin-spin spacing of 7.4 nm - this is on the border of what we can guarantee with the upper-bound given to us through SIMS, and so one might expect borderline behavior in the P1 ensemble. Nevertheless, we will find that the system of spins is likely narrower[7] than the SIMS estimate and the confined ensemble does, indeed, result in low-dimensional behavior.

[7]The densities and spacing estimates here assume a boxcar function for the density. This is almost certainly not the case; the density is probably closer to a Gaussian. The concentration of density close to the center tends to push the ensemble into a more 2D limit.

4.1.2 Patterning for y-confinement

Next, we will briefly discuss the method for confinement along y. This method, which I call patterning[8], relies on the preferential incorporation of nitrogen at specific sites along the lateral (xy-plane) diamond surface. A defect on that surface is required to break the symmetry and introduce some degree of inhomogeneous incorporation along the plane. In this section and the latter parts of the chapter, we will discuss step bunches as a novel means to achieve that goal.

Figure 4.5 a) shows a schematic of a step bunch. At early times, a perfectly ordered surface has each step uniformly spaced from every other. As the growth continues, steps will tend to "bunch" up, resulting in macroscopic ensembles of steps[9] that keep the overall miscut angle preserved but result in highly inhomogeneous surfaces. Many mechanisms have been proposed to explain why step edges bunch. For example, in growth modes where surface diffusion plays a large role, Ehrlich-Schwoebel[261, 262, 263] barriers (energy barriers that diffusing adatoms encounter at steps) will naturally produce step bunching. Entropic effects will also lead to some step bunching (though entropy arguments alone cannot fully explain the usual magnitude of step bunching). Additionally, elastic relaxation near steps can generate attractive interactions between steps[264] that will result in bunching. Chemical effects are also hypothesized to play a role in some types of growth[259, 260, 265]. I will quickly note here that many of these mechanisms rely on arguments based on adatom diffusion (in particular, the often-referenced Ehrlich-

[8]I call this section "patterning" even though the confinement evidenced through striated distributions of NVs presented throughout this chapter was obtained entirely by accident. Indeed, the word "patterning" seems to suggest some degree of intentionality. I use this word for two reasons: first, I anticipate that soon control over step bunching and the processes that govern it will advance to the point where more intentional creation of step bunches and the engineering of their parameters will be possible. Second, I wish to include other methods beyond step bunches into this method of dimensional engineering. These other methods could include hillocks or photolithographic patterning of masks and subsequent implantation.

[9]I highly recommend Guin *et al.*'s[259, 260] highly cogent multi-part discussion on step bunches.

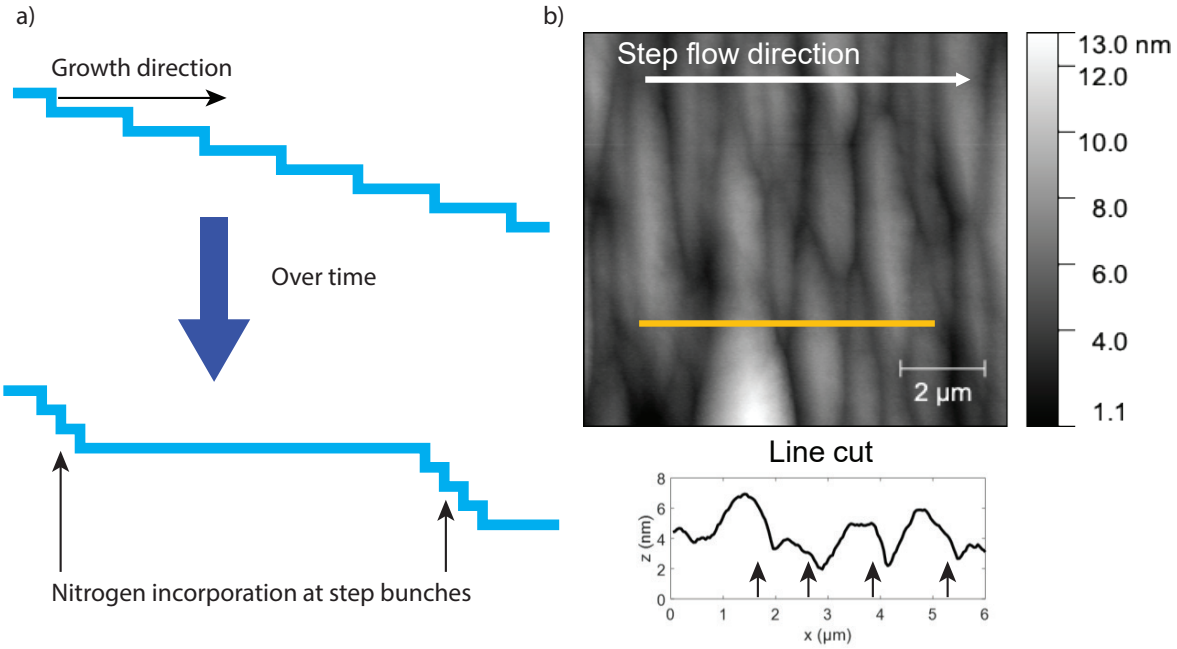

Figure 4.5: An illustration of step bunching. a) A schematic showing an initially uniformly spaced distribution of steps, aggregating into bunches over time during growth. Note that the overall step density (and miscut) remains constant. Because nitrogen tends to incorporate preferentially at steps[1] (see Chapter 2), step bunches will have an increased concentration of nitrogen. b) An atomic force microscopy (AFM) image showing a heavily step bunched sample (L043). A cross section taken at the orange line is plotted below. Arrows denote locations where nitrogen is likely to incorporate.

Schwoebel mechanism) - for diamond CVD growth, based on the arguments in Chapter 2, surface adatom diffusion is not dominant in growth and adatom diffusion lengths are very small. Regardless of the *exact* mechanism(s) responsible for step bunching in CVD diamond, it is sufficient for this chapter to state that steps do bunch and leave the determination of the mechanisms responsible as a project for future work. Figure 4.5 b) shows an atomic force microscopy (AFM) image of a highly step bunched sample. A linecut across the bunch is shown with arrows indicating locations with a high potential for nitrogen incorporation.

We justify the assumption that step bunches have an increased density of incorporated nitrogen via four complementary images taken on the same region of the sample. The images were colocalized with respect to each other using hillocks on the sample as coarse positioners. For sub-micron colocalization of the four distinct measurements, the step bunches themselves have sufficiently unique patterns that it is possible to find the same groups of bunches via inspection. Figure 4.6 a) shows a confocal PL image of sample L043[10]. The distinct striated features are NV centers that formed due to higher concentrations of nitrogen along the step bunches. The correspondence of NV features with nitrogen density is confirmed using nanoSIMS performed on a Cameca NanoSIMS 50L at Stanford University in collaboration with the Mukherjee group. This data is shown in Figure 4.6 b), which shows the lateral distribution of nitrogen integrated over the entire growth (for comparison to the PL, which is also necessarily integrated over the entire growth). Figure 4.6 c) shows NV ground state depletion (GSD) microscopy[266, 267] images of the same ensemble. GSD is a technique that uses a donut-shaped beam to achieve spatial resolution well beyond the optical diffraction limit for non-linear point emitters.

[10]Sample L043 is a trilayer sample grown by Lillian Hughes. There are three layers of intentionally doped nitrogen (which is the meaning of trilayer). The last (most shallow) layer is 10× higher density, and so the majority (90%) of the signal in Figures 4.6 a-c) is coming from this topmost layer. The AFM image is, of course, the surface of the diamond and, thus, represents the step bunches at the very end of the growth. See section 4.3.2 for more details.

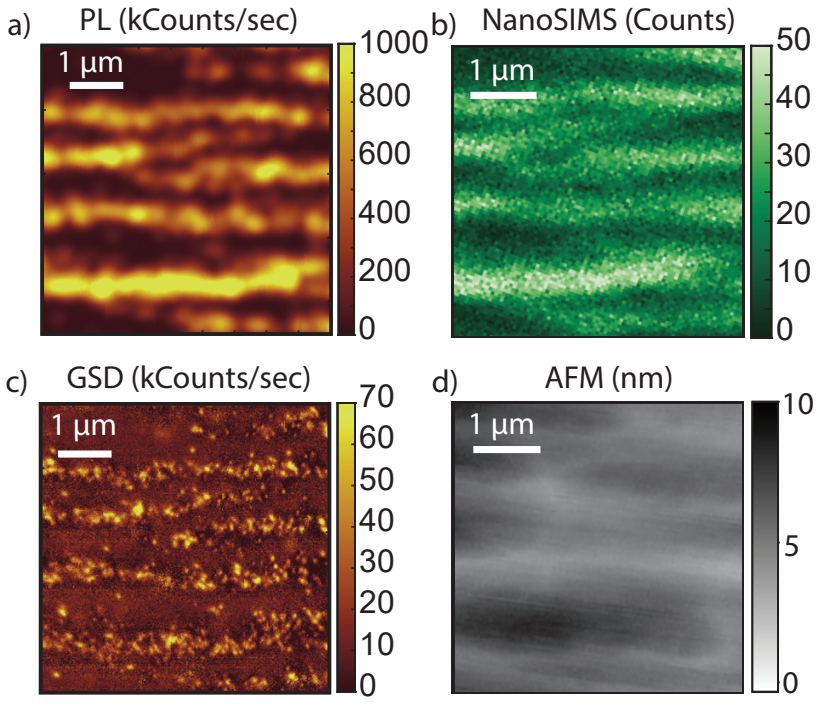

Figure 4.6: Four colocalized measurements of the same step bunched region on L043. a) A confocal PL measurement. Brighter regions indicate a higher density of NV centers. The NVs are organized along striations that correspond to step bunches. b) NanoSIMS data showing the distribution of nitrogen in this region. The strong similarity between this data and that shown in a) indicates that the striated NVs are due to preferential nitrogen incorporation rather than preferential formation dynamics related to the step bunching. c) Ground state depletion (GSD) microscopy image showing the fine structure of the NVs within the step bunch. d) Atomic force microscopy (AFM) image showing the topography of the sample. Common features demonstrate that the enhanced nitrogen incorporation occurs at the step bunches.

This allows us to gain insight into the spatial distributions of NVs within step bunches beyond what is accessible using conventional optical techniques. Finally, we compare all three images to an AFM image of the surface in Fig. 4.6 d). The correlations between these four images indicate a common cause: step bunching.

4.1.3 Measurement of dimensionality via coherence decay

Finally, we require some method of assessment for whether a system has met the requirements on a microscopic, inter-spin level of low-dimensionality. The method we will employ throughout the rest of the chapter is a careful analysis of the coherence decay under double electron-electron resonance (DEER).

DEER allows us to address specific species within the bath of spins. We will use the framework for measuring dimensionality detailed in Davis *et al.*[255]. The coherence, C, of an ensemble of NVs under DEER will decay as a function of time, t, like a stretched exponential,

$$C(t) = \exp\{-(t/T_2)^n\}. \tag{4.9}$$

The stretch power, n, depends on three important parameters:

- The power of the long-range interaction governing the dynamics, $\alpha \Rightarrow J \sim 1/r^\alpha$. For dipole interactions, we have $J \sim 1/r^3$.
- The dimensionality of the system, d.
- The correlation of the bath. The bath has a characteristic correlation timescale, τ_c. On timescales that are long with respect to the correlation time, the system behaves diffusively, and the phase accumulates like a random walk. At short timescales, the system is said to behave ballistically.

The stretch power will be given by,

$$\begin{aligned} &\text{Ballistic } (t < \tau_c) \ : \ n = \frac{d}{\alpha} \\ &\text{Diffusive } (t > \tau_c) \ : \ n = \frac{d}{2\alpha}, \end{aligned} \tag{4.10}$$

as described in Ref. [255].

Figure 4.7 shows an example of both regimes for 3D, 2D, and 1D. Small stretch powers (as in lower dimensional systems) result in fast decays with long tails, meaning that a semi-coherent ensemble can persist over much longer timescales relative to their higher dimensional counterparts. Plotted alongside (bottom) are the logarithms of the same functions on a log-log scale (called triple-log scale). These are plotted this way because taking the negative logarithm converts the function to a power law, which, when plotted on log-log axes, makes the change in power (via the change in slope) immediately apparent. During the next two sections, when we wish to highlight a change in the stretch power, the data will be plotted in this form.

4.2 Two-dimensional ensembles

In this section, we will discuss an ensemble of two-dimensional spins in sample S011. These systems, as described in Eqn. 4.5, have no net dipolar couplings after configurational averaging. In the rest of the Chapter, we will use the type B simulation scheme described in Chapter 3. Here, the NVs act as a probe of the external bath, whose properties we seek to investigate. One of the key conceptual differences between the type of schemes described in Chapter 3 and those in this Chapter is the recoupling pulse whose frequency is tuned to the P1 resonance (the spin defects responsible for the disorder term in Chapter 3). By selectively driving these defects in addition to driving the NV centers, we can enhance the importance of the disorder via recoupling, leading to NV ensembles whose dynamics are governed almost entirely by the P1 centers. A careful analysis of these dynamics, under the recoupling, reveals a wealth of information about the P1 bath[255].

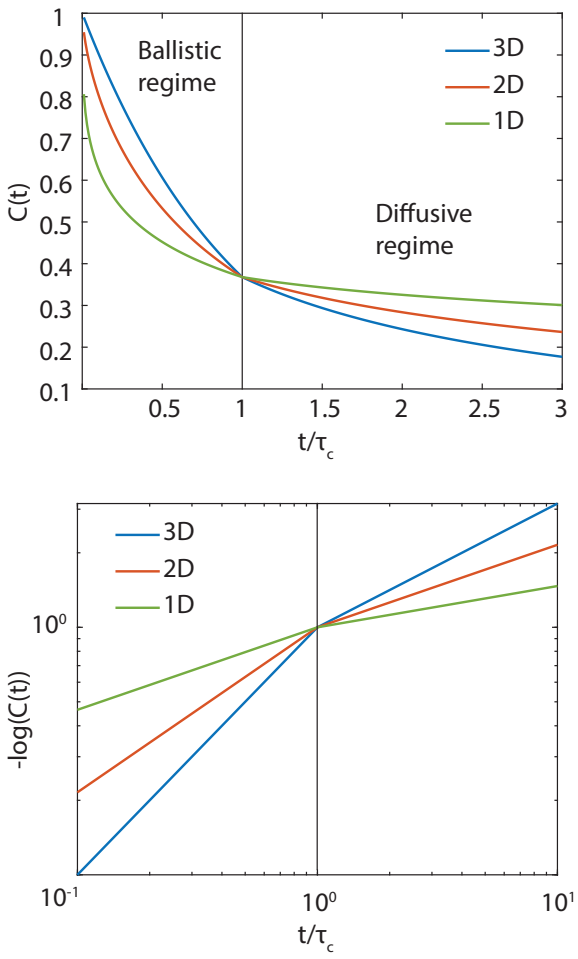

Figure 4.7: Theoretical decay profiles for various dimensionalities. a) Decays on a linear scale for 1D, 2D, and 3D. The verticle line indicates the crossover between a ballistic-type decay and a diffusive decay. For these examples, $\tau_c = T_2 = 1$. b) The same coherence decay on the triple-log scale. Here, the slope denotes a change in the stretch power, n.

4.2.1 Double electron-electron resonance

Double electron-electron resonance (DEER) has been used to study a wide variety of defects in diamond, including P1 centers[212, 255, 268], C centers[269], NVH[270], external spins[271], and other NV centers[272]. A DEER sequence consists of two different microwave tones, one of which drives the NV ensemble and another that drives the external spin species. The NV microwave tone will deliver a spin echo sequence consisting of an initial $\pi/2$-pulse to prepare the NVs into a collective state on the equator of the Bloch sphere, a subsequent π-pulse after a time, τ, and after a final period of time, τ, another $\pi/2$-pulse with a green readout measure the state of the ensemble. Where DEER differs from a traditional spin echo is that during the intermediary π-pulse, we apply another microwave tone for a fixed duration, τ_{P1} at a frequency of f_{P1}[11].

Figure 4.8 a) shows a DEER spectrum for S011, showing three distinct peaks. These three peaks are labeled 1/12, 1/4, and 1/3, where these labels indicate the fraction of total P1 centers contributing to each peak. There will be additional peaks (not pictured) to the right corresponding to an additional 1/4 and 1/12 peak, such that the total peaks sum to 1. The reasons for the splitting are two-fold. First, the nuclear state of the nitrogen in the P1 center gives rise to 3 possible hyperfine states. Second, the lattice gives rise to a Jahn-Teller[273] splitting. The substitutional nitrogen atom of the P1 has four nearly degenerate sites it can sit on, corresponding to each of the four directions in the $\langle 111 \rangle$ group. One of these sites will be aligned along the magnetic field, and the other three will be exactly degenerate. Thus, we have the following groups:

- $(-)1/12$: Corresponding to the distortion axis along the B-field and the nuclear state $I = -1$

[11] The labels, P1, are chosen here because for the rest of the Chapter, we will only address P1 centers. But other than the fact that we will choose the frequency to specifically address P1 centers, there is nothing else specific to P1 centers about this sequence.

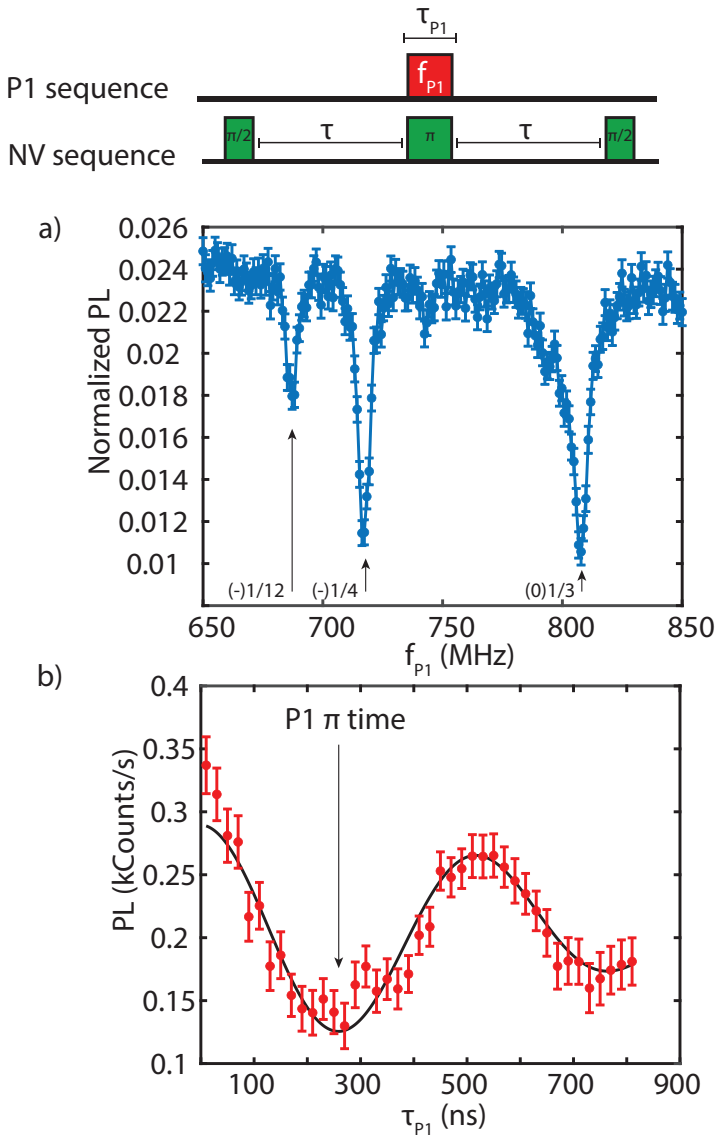

Figure 4.8: Double electron-electron resonance (DEER). a) Sweeping the frequency during a DEER measurement reveals a spectrum whose peaks indicate specific species of spins. b) Varying the length of the recoupling pulse results in Rabi oscillations. The first dip in these oscillations is the π-time.

- $(-)1/4$: Corresponding to a distortion axis along one of the three other $\langle 111 \rangle$ directions and the nuclear state $I = -1$
- $(0)1/3$: Corresponding to all of the four distortion axes and the nuclear state $I = 0$
- $(+)1/4$: Corresponding to a distortion axis along one of the three other $\langle 111 \rangle$ directions and the nuclear state $I = +1$
- $(+)1/12$: Corresponding to the distortion axis along the B-field and the nuclear state $I = -1$

We choose the $(-)1/4$ peak because it has a relatively high density (resulting in stronger J couplings) while being distinct from confounding species close to $g = 2$ such as NVH[12]. Driving other peaks, such as the 1/12 peaks, allows us to change the effective density of the recoupled spins. For optimal recoupling, we drive Rabi oscillations of the bath spins and look for the first dip, which corresponds to a complete π-pulse. A Rabi oscillation for the $(-)1/4$ peak is shown in Figure 4.8 b).

The decay for the two-dimensional spot is shown in Figure 4.9 a) on a linear scale. Figure 4.9 b) shows the same data on the triple-log scale described in Section 4.1.3. Power law guides to the eyes are plotted alongside the data for reference. We observe a crossover in the power law at $\tau_c \sim 3\,\mu s$. These stretch powers ($n = 2/3$ and $1/3$) are consistent with the expectation for a two-dimensional ensemble under dipolar interactions ($\alpha = 3$), and contrasts with the usual $n = 1$ observed for three-dimensional ensembles, as in Refs [222, 255]. The correlation time, τ_c, denotes the average time a spin in the bath retains memory of its initial orientation. Bauch *et al.*[222] provide a model for relating correlation times to other physical parameters (such as T_2^* and the density) for three-dimensional ensembles. Hughes *et al.*[90] provide a framework for relating this decay to

[12]Unlike, for example, the $(0)1/3$ peak, which is very close to $g = 2$.

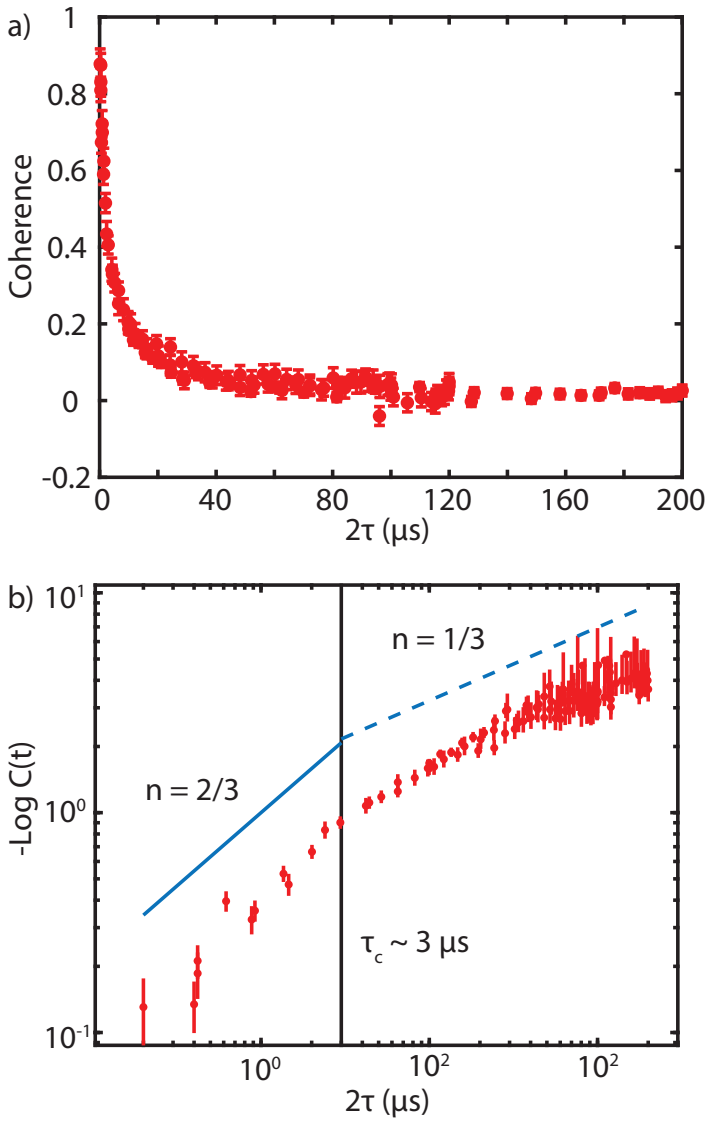

Figure 4.9: a) DEER decay for a 2D ensemble. b) On the triple-log scale, two distinct stretch powers are seen. These are the expected powers for a 2D ensemble. The vertical line denotes the transition from ballistic to diffusive transport and occurs at the bath correlation time, τ_c.

the density of the bath. We consider both frameworks as a function of the density of the recoupled group, ρ. The Bauch framework relates the timescale for the Ramsey-like decay of the ensemble to the density like $T_2^* = 1/(A\rho)$, where $1/A = 9.6\,\mu\text{s ppm}$. The Hughes framework relates the decoherence to the dimensional density as $T_2^* = 1/(\rho^{1/n} a J)$, where a is a dimensionless parameter that depends on the density such that $a_{2D} = 2.626$, and $a_{3D} = 3.318$, and J is the dipolar coupling strength, $J = 2\pi \times 10\,\text{kHz/ppm} = 2\pi \times 52\,\text{MHz nm}^3$. In the Hughes framework, the density, ρ is the dimensional density defined in Eqn. 4.8, and n is the stretch power as defined in Eqn. 4.1.3. The density estimated from the Bauch model is $\rho_{\text{B}} = 3.2$ ppm, leading to a total nitrogen density for all groups of ~ 13 ppm, which should be considered as a lower bound on the density. The 2D density estimated from the Hughes model is $\rho_{\text{H}} = \sim 28$ppm nm, for a total nitrogen density for all groups of ~ 110 ppm nm. For both estimates, we use a FID Ramsey timescale of $T_2^* \approx 3\,\mu\text{s}$.

4.3 One-dimensional ensembles

In this section, we will describe a one-dimensional system of spins realized through incorporation along step bunches. Using the dipolar coupling described in Eqn. 4.5, we write the dipolar strength as a function of the 1D axis in the xy-plane, ϕ_0. The dipolar energy will be,

$$\begin{aligned} &\int_0^{2\pi}\int_0^{\pi} f(r)((\cos\phi + \sin\phi)^2 - 1)\delta(\phi - \phi_0)\delta(\theta - \pi/2)\sin\theta \; d\theta d\phi, \\ &= f(r)\sin 2\phi_0. \end{aligned} \tag{4.11}$$

Thus, we find that in a 1D dipolar chain, the average coupling strength can be tuned

from positive to zero to negative simply by rotating the quantization axis with respect to the chain axis.

As discussed in Sections 4.1.2 and 4.1.1, we will achieve confinement along two axes using a combination of delta-doping (for z) and step bunching (for y). However, there are some length scales associated with the problem that are worth discussing. Because both the doped layer and the step bunches have a finite extent, we must consider what physical scales determine whether a system is 1D or not. These scales are shown schematically in Figure 4.10. First, the width, w, denotes the lateral extent of a single bunch and will be proportional to the number of aggregated step edges. Additionally, wider steps will accumulate more nitrogen such that $\rho_{0,1D} \propto w$. Another important length scale for one-dimensional physics is the distance between nearby step bunches, d. The thickness of the doped layer, t, is also critical, though we will assume this is small. Finally, there is a length scale, $r \sim (J\tau)^{1/3}$[256], which corresponds to the radius over which entanglement can have ballistically traveled since NV initialization. Intuitively, this can be understood via a light-cone-like picture where, at very short times, the NV has only information about the states of nearby spins. As time accumulates, the sphere over which the NV probes the environment grows.

The various limits are described below:

- $w > r$: 2D. The system resembles a flat plane, similar to the 2D system described in Section 4.2.
- $t > r$ and $w > r$: 3D
- $r > d$: 2D. The spins in adjacent step bunches begin to interact, resulting in a 2D ensemble
- $w < r < d$: 1D. In this case, the central spin (the NV) has begun to detect the

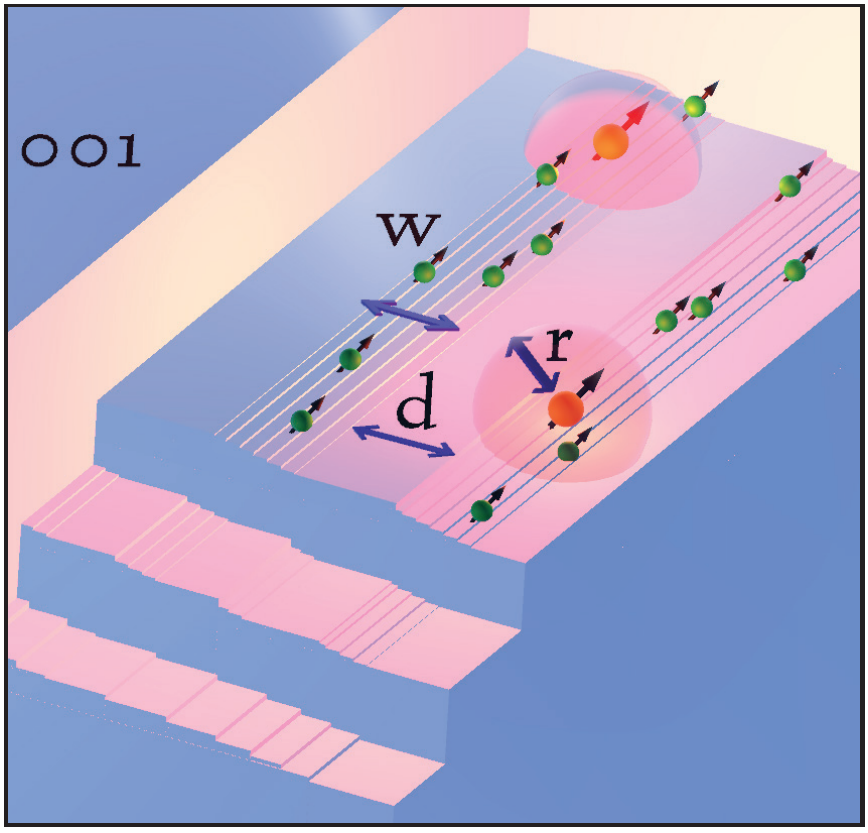

Figure 4.10: A schematic indicating three important length scales for engineered one-dimensional dipolar systems. The width of the one-dimensional chain, w, sets both the average coordination of a spin and the length scales over which entanglement must diffuse before one-dimensional behavior begins. The distance between chains, d, must be large to avoid cross-talk between chains (resulting in a 2D-type ensemble). Finally, the diffusion length, $r \sim (J\tau)^{1/3}$, is another important scale. If we satisfy the criterion, $w < r < d$, the system is expected to behave as a one-dimensional spin chain.

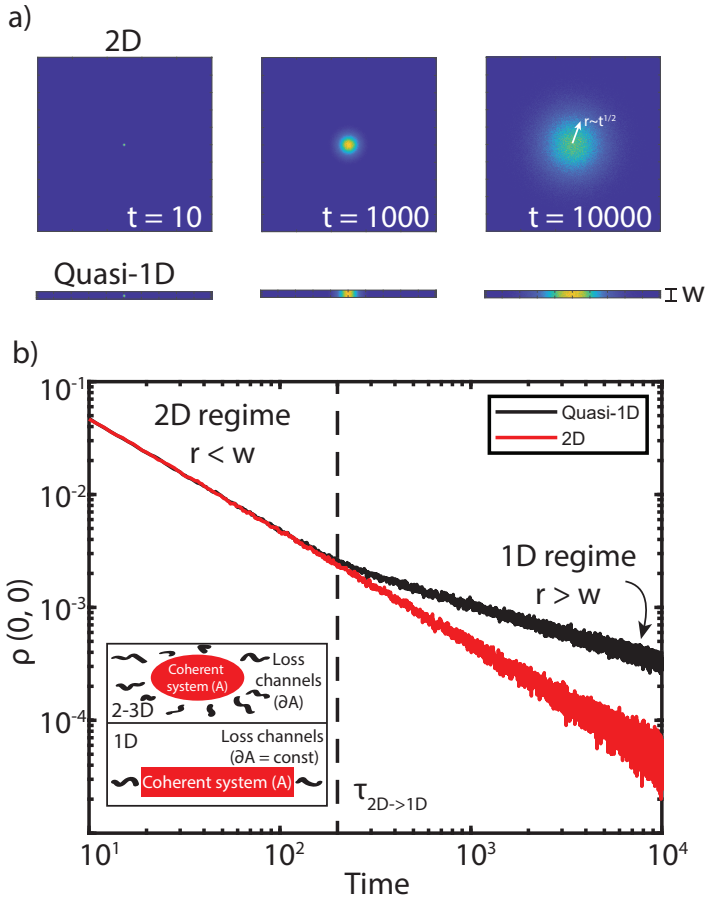

Figure 4.11: A numerical comparison between 2D and quasi-1D diffusion. a) Colormaps showing the density of particles as a function of time for 2D and quasi-1D systems. b) A plot of the density of particles as a function of time at the center of the system for both cases. Once the diffusion reaches the edges of the quasi-1D box, it begins to diverge from the 2D diffusion.

finite size of the bunch but has not started to detect adjacent step bunches. In this case, the system will be governed by one-dimensional decoherence.

The dependence of each of these criteria on the quantity r, which itself depends on time, results in the interesting fact that the dimensionality of the system can change as a function of time. As r increases over time, the system can change between different dimensionalities, resulting in a geometric crossover, as described in Ref. [256].

A diffusion analogy can help in gaining some intuition about the origin of the dimen-

sional crossover. Figure 4.11 a) presents numerical simulations of random walkers in a confined geometry. In this example, at each time step, each walker is allowed to move 1 space in one of the cardinal directions (up, down, left, right) or may not move with a probability (1/3). Boundary conditions of $\vec{j} \cdot \hat{n} = 0$ are enforced, where $\vec{j}$ is the particle current, and $\hat{n}$ is the boundary normal[13]. Histograms for 500e3 walkers over 10000 timesteps are shown for a system whose length, L, and width, w, are equal, $w = L = 501$ (called 2D), and another system with finite width, $w = 21$, such that $w \ll L = 501$ (called quasi-1D).

Because this is a diffusive system, we expect transport over a length scale that depends on time like $r \sim t^{1/2}$. Figure 4.11 b) shows the density of particles at the origin as a function of time for both systems. The vertical dashed line corresponds to a critical timescale, $\tau_{2D\to1D} \approx \frac{3}{4}r_c^2$, where the quasi-1D system begins to diverge from the 2D system. The critical length scale is the half-width of the quasi-1D strip. For decoherence along a quasi-1D strip of dipoles, a similar intuition holds, and we expect to observe a transition from 2D type decoherence to 1D type decoherence at timescales that are long compared to transport of entanglement compared to the width of the step bunch. The inset illustrates of Figure 4.11 illustrates the connection between the idea of diffusion and coherence loss in an ensemble of spins. Once the system reaches a low-dimensional limit, the channels available to decohere become radically reduced and, importantly, do not grow as the entangled volume grows. Once the system reaches this regime, we expect to observe a "coherence blockade" where the rate of decoherence becomes slower, and the state is preserved over a long period of time.

[13]I.e., particles are stopped if they attempt to cross the boundary.

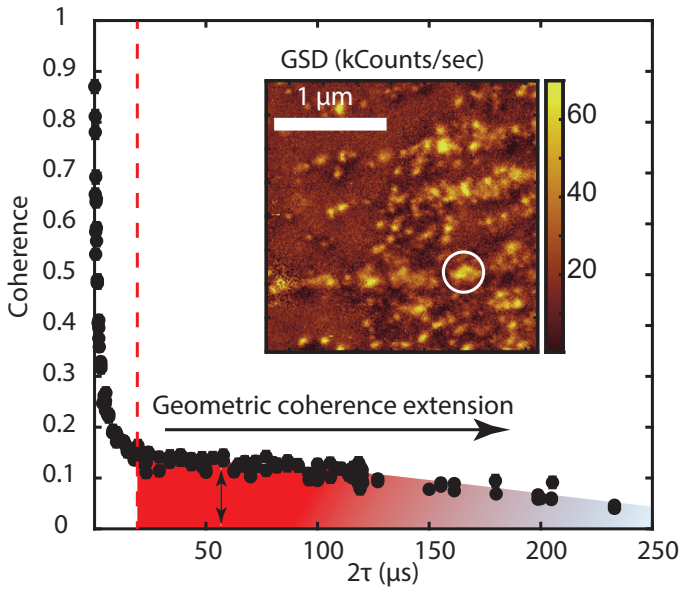

Figure 4.12: DEER decay for the 1/4 peak of a 1D ensemble. The region where this data was taken is shown in the inset. The shaded red region indicates the onset of a long-lived coherent state due to geometric confinement.

4.3.1 One-dimensional decoherence

Figure 4.12 shows the decoherence of a heavily striated ensemble of NVs, indicating a high degree of step bunching. A GSD image of the region studied is shown in the inset, where the white circle indicates the rough size of the confocal spot used to generate the data in the decay profile. The decoherence here is a DEER decay sequence as described in Section 4.2, and the red-shaded region indicates the onset of a geometric coherence extension due to one-dimensional confinement. While the $1/e$ time of this ensemble is roughly 2.2 μs, a substantial coherence above 10% persists for hundreds of μs.

We next examine the same data on the triple-log scale described in Section 4.1.3. On this scale, three distinct regimes of decoherence are made clear, each described by a different value of n, indicated by a different slope.

The first regime, called "2-D early decoherence" corresponds to a ballistic, 2D regime where the total free evolution time, $2\tau < \tau_c$. Here, τ_c is the correlation time of the

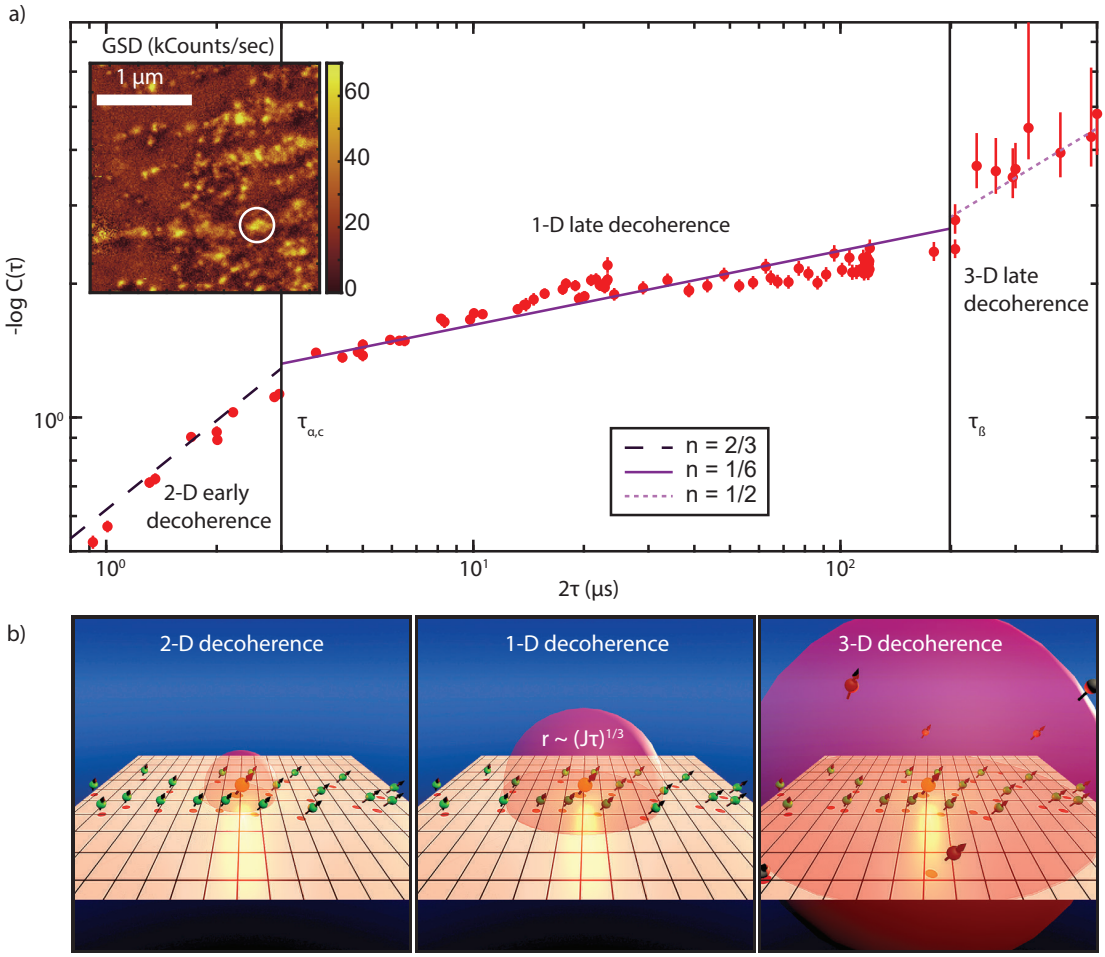

Figure 4.13: DEER decay for the 1/4 peak in a one-dimensional ensemble, plotted on a triple-log scale. We observe three distinct regimes of decoherence. The first regime corresponds to an early-time 2D decoherence resulting from the finite width of the nitrogen distributed within the step bunches. The next regime is the long-lived one-dimensional state. Here, the stretch power is $n = 1/6$ and persists over nearly two decades. Only a one-dimensional system results in a stretch power of 1/6, indicating that the step bunched nitrogen results in a 1D dipolar ensemble. The final regime is best fit by a 3D diffusive-type decoherence. This may be due to "dark" spins distributed throughout the diamond or additional decoherence from the diamond surface.

bath as described in Section 4.2. This regime has a slope of $n = 2/3$, consistent with the prediction for 2D. Figure 4.13 b) shows a schematic illustration of each of the three regimes, where the green spins represent surrounding P1 centers and the central orange spin represents the NV center. The semi-transparent sphere denotes the sphere of entanglement where the radius is given by $r \sim (J\tau)^{1/3}$. At a time of $\tau_{\alpha,c} = 3\,\mu s$, the system transitions to a late, one-dimensional regime. Two subscripts are used for this crossover time because this crossover corresponds to two distinct regime crossovers that occur close to each other in time. The first is the correlation time crossover, τ_c, denoting the transition from ballistic to diffusive transport, and the second is the dimensional crossover, denoting the change from 2D to 1D. We verify that these are two independent crossovers by changing the effective density of spins (which pushes the correlation time to longer values but does not affect the dimensional crossover). The verification that these are independent crossovers is described at the end of this section.

The one-dimensional regime of decoherence, characterized by a very small stretch power, persists over nearly two decades of free evolution. The exact value for the stretch power of $n = 1/6$ can only come about from late time, one-dimensional decoherence[255], and so we take this as very strong evidence that the system is behaving like a 1D spin chain. Curiously, the value of $\tau_{\alpha,c}$ corresponds to a length scale of roughly $r_{\alpha,c} \sim 10\,nm$, much smaller than the scales indicated by GSD. However, GSD has a minimum spatial resolution (in this image) of $\sim 70\,nm$, so there is no contradiction between the measurements. Instead, we take the small length scale revealed by the DEER decoherence to be evidence of features within the bunches below the resolution of GSD. This suggests that the incorporation of nitrogen due to the edges lays along fine features that have a width of 10 nm, within the larger, $\sim$200 nm confocally detectable bunches.

At very late times, the system eventually loses the properties associated with the coherence blockade, and the system rapidly decoheres to the thermal equilibrium. We

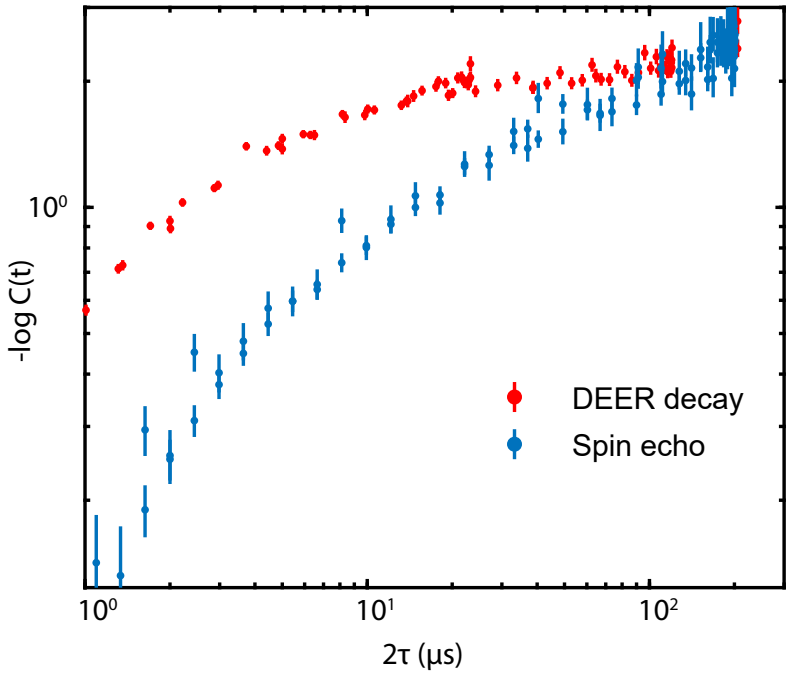

Figure 4.14: A comparison between DEER decoherence and spin echo decay for the 1/4 peak in a one-dimensional ensemble. At late times, the two datasets converge, indicating that the late time decoherence shown in Figure 4.13 is due to sources unrelated to the recoupling DEER pulse and is limited by incoherent noise unfiltered by the spin echo.

call this crossover time τ_β. At this time, the system is well-described by a stretch power of $n = 1/2$, corresponding to a late-time three-dimensional decoherence. Our hypothesis to explain this observation is that at late times, when the interaction radius becomes large, the ensemble becomes limited by incoherent spinful defects outside of the deliberately recoupled bath. This is supported by the fact that in this regime, the coherence is equal to the spin echo measurement.

A comparison of the DEER data to the spin echo data on the same spot is shown in Figure 4.14. Within the 3D late decoherence regime, the spin echo data is on top of the DEER decay, indicating that the recoupling pulse no longer has a substantial effect and other effects are dominating the decay. This can be due to other "dark" defects in the

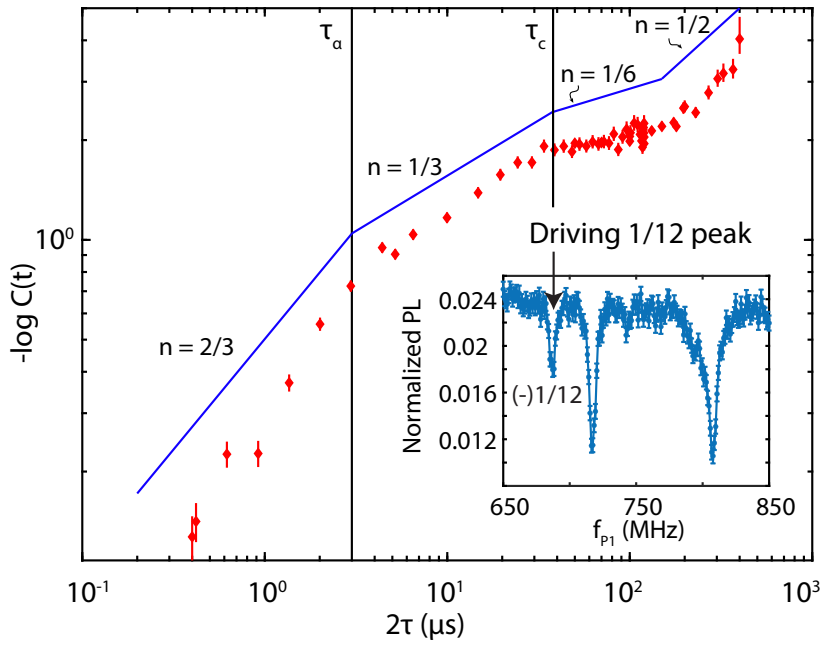

Figure 4.15: DEER decay for the 1/12 peak in the same region as Figure 4.13. Changing to the 1/12 peak results in a lower effective spin density. Lowering the spin density results in a longer correlation time but leaves the dimensional crossovers unchanged.

lattice or, potentially, effects from the noisy surface of the diamond.

We verify the hypothesis that there are two overlapping crossovers in Figure 4.13 a) at the time $\tau_{c,\alpha}$ corresponding to a dimensional crossover, τ_α and a ballistic to diffusive crossover, τ_c by varying the density of recoupled spins *in situ* by driving the $(-)1/12$ peak. The P1 centers associated with this peak are 1/3 as dense as the P1 centers driven in Figure 4.13 a). Reducing the density results in a longer correlation time, but the extent of the distribution of defects should be identical to the denser ensemble. Because the spatial extent of the distribution is identical between the two datasets, the dimensional crossovers τ_α are also identical. For the less dense data, the correlation time, τ_c, is significantly longer at nearly 38 µs. In the 1/12 dataset, we observe a new regime not clearly observable in the 1/4 dataset: a 1D ballistic regime of decoherence ($n = 1/3$).

4.3.2 Measurement of nitrogen incorporation in step bunches

In this final section, we discuss a new method of measuring morphological features as a function of time during CVD growth. We anticipate that this method can be extended to any crystal growth technique where dopants can be employed. The method discussed in this section uses a combination of tracer elements that preferentially incorporate along a step. In combination with a 3D elemental composition analysis tool, in this case, nanoSIMS, we can visualize the time evolution of morphologies after-the-fact. We will use this technique to image step bunch formation at three different times and track the evolution over the course of a growth. We use a Cameca NanoSIMS 50L at Stanford University in collaboration with the Mukherjee group for the nanoSIMS data presented in this section.

The sample we used for characterizing this technique is L043. L043 is a CVD grown sample (miscut $\theta = 0.646°$) with three spatially separated doped layers. The growth of L043 consisted of the following recipe:

- 0.4 sccm (^{12}C) methane, 1.5 hours
- 5 sccm (^{15}N) nitrogen, 20 min
- 0.4 sccm (^{12}C) methane, 2 hours
- 5 sccm (^{15}N) nitrogen, 10 min
- 0.4 sccm (^{12}C) methane, 2 hours
- 5 sccm (^{15}N) nitrogen, 30 min
- 0.4 sccm (^{12}C) methane, 1.5 hours

Conventional SIMS gives the concentration in the three layers as,

- Layer 1, Density: 36 ppm nm, depth: 129 nm, width 4.2 nm.
- Layer 2, Density: 46 ppm nm, depth: 90 nm, width 3.9 nm.
- Layer 3, Density: 617 ppm nm, depth: 43 nm, width 8.5 nm.

Interestingly, the incorporated nitrogen does not scale monotonically with doping time and instead seems to scale with time since the growth began. This could be due to enhanced step bunching resulting from nitrogen impurities[274] or a non-linear dependence of nitrogen incorporation with step density[1][14].

Figure 4.16 a) shows images of a large step bunch. Both topographic atomic force microscopy (AFM) and confocal microscopy data are shown for the same step bunch. The arrows indicate the phase component (i.e., the projection of the 001 axis along the surface plane) of the miscut and, thus, the growth direction. This is further confirmed in the nanoSIMS. Plotted in Figure 4.16 b) are the concentrations in detected counts for the three layers in the growth. These three images form three frames in a "movie" of the morphological evolution of the diamond surface over a growth. We anticipate extending this technique to many-layered samples and using a dopant that is guaranteed to not interfere with the chemistry of the growth[15]. We observe this large step bunch begins as a small aggregation of nitrogen in an otherwise quite featureless layer. As the growth proceeds, the step bunch travels across the sample, a distance of roughly $\sim 5\,\mu m$. Since these layers are separated by 5 hours in growth time, we can conclude that this step bunch traveled at a rate of $1\,\mu m/h$. If we compare this rate to the depth-wise growth rate ($17\,nm/h$), the ratio of the two will be equal to the miscut (in the case where the step bunch is traveling at the same rate as a single step). We obtain a value of $\arcsin(0.017) \approx$

[14]Since step bunches have a greater concentrated density of steps than single steps, and as the growth goes on, step bunches become larger and larger, the non-linear dependence of nitrogen incorporation on step density may result in higher nitrogen densities for later times in the growth.

[15]For example, ^{13}C is distinguishable from ^{12}C in nanoSIMS but is highly unlikely to be chemically distinct and so, will not interfere with the growth.

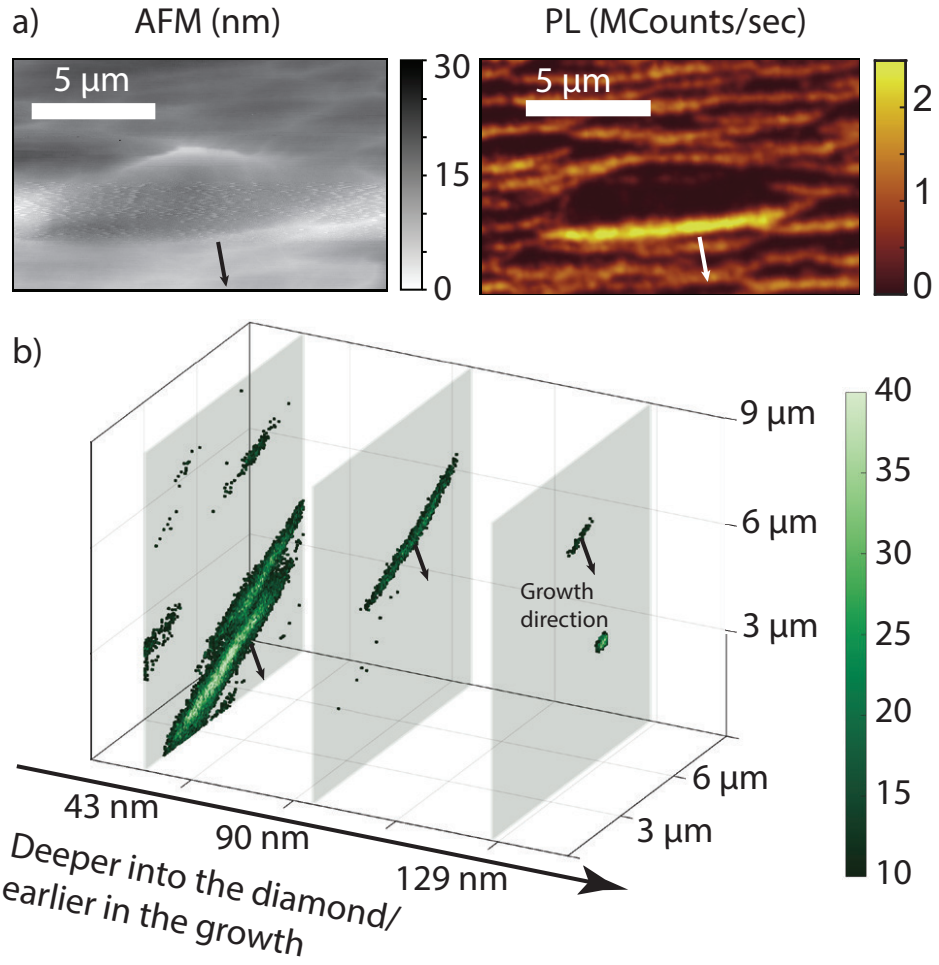

Figure 4.16: Imaging the evolution of a step bunch using nanoSIMS and nitrogen tracers. a) Atomic force microscopy and confocal photoluminescence (PL) measurements of a large step bunch in sample L043. The arrows indicate the direction of step flow during growth. b) NanoSIMS data for each of the three layers in L043, showing the evolution of the step bunch shown in a).

1°, indicating that the step bunch is actually traveling somewhat slower than a typical step edge. This technique gives a unique window into the evolution of step bunches and other morphological features during crystal growth that is otherwise inaccessible. Tracer-mediated nanoSIMS imaging could be extended to other kinds of morphological features, as well, such as the hillocks described in Chapter 2. Additionally, nothing about this technique is specific to CVD growth or diamond growth. These methods could be easily extended to any growth method where the introduction of isotopically distinct dopants is possible (such as MBE).

Tracer elements have been used before to track the evolution of step bunches in MBE-grown GaAs(110) as described in Ref. [275] using a combination of transmission electron microscopy (TEM) and AlAs marker layers. The nanoSIMS tracer method has a number of noteworthy advantages over the TEM tracer method. First, nanoSIMS gives both lateral and depth information (resulting in a fully 3D image of the crystal), whereas imaging via TEM tracers only gives a cross-sectional view of the growth. Secondly, nanoSIMS is sensitive to concentrations below ppm levels, whereas electronic imaging methods (like TEM) usually have a detection limit several orders of magnitude above that[276, 277]. The combination of nanoSIMS techniques with the decoherence probes into nanoscale distributions of spins described earlier in this chapter opens up new ways to probe the distributions of dopants incorporated during growth.

4.4 Conclusions

In this chapter, we have discussed methods to engineer lower-dimensional ensembles of NV centers and the resulting different decoherence profiles. In this final section, we will discuss possible future experiments using the low-dimensional ensembles of spins described in the previous sections.

One interesting possibility is using one-dimensional systems of spins in combination with super-resolution techniques such as GSD to visualize spin diffusion stroboscopically. At low temperatures, NV T_1 times can approach timescales as long as seconds or even minutes[105, 278, 279]. If we consider a spin chain whose spacing corresponds to the equivalent volume density for a 1 ppm ensemble ($\sim 17\,\mathrm{nm}$), we can calculate the ballistic travel distance for a spin excitation in a typical T_1 time. A 1 ppm ensemble has a spin flip rate of $2\pi \times 10\,\mathrm{kHz}$. In one second, this is a possible 66000 flips, resulting in a maximum ballistic travel distance of $\sim 1\,\mathrm{mm}$ between spins spaced 17 nm apart. The diffusive travel distance (the physics easier to study) will be closer to $4\,\mu\mathrm{m}$ (assuming one-dimensional random walk-like transport: $r \sim t^{1/2}$). These scales are easily accessible at low temperature even without super-resolution techniques. At elevated temperatures, where the T_1 is closer to 1 ms, the diffusion distance is $\sim 140\,\mathrm{nm}$ - substantially smaller, but still detectable with GSD techniques. A stroboscopic pump-probe experiment, where one initializes the spin state of a volume of spins and then generates a spin excitation via GSD, could be used to image the diffusion of spins in both space and time. Moreover, a disordered dipolar spin chain is a ripe environment for testing many-body localization. Preparing spin excitations in this manner may provide a clean platform for studying the diffusion of a spin excitation in a disordered dipolar landscape.

Additionally, the dipolar coupling can be manipulated by changing the quantization axis with respect to the chain axis, as described in Eqn. 4.11. Because the quantization axis for the P1 centers can be changed via the magnetic field axis, a variable magnetic field could be used to "turn off" or "turn on" interactions within the chain. A first step towards realizing this would be studying the correlation time of the ensemble as a function of the field angle with respect to the step bunch axis. If *in situ* control over the coupling strength were realized, it would be possible to design a spin-diffusion valve, where transport (and decoherence) along a line of spins could be halted through,

for example, current-controlled magnetic fields. A device such as this could act as a quantum information switch, allowing or disallowing entanglement diffusion along an "wire" of coupled qubits.

Solid-state spin systems provide a method to test the behavior of many-body quantum mechanics in the thermodynamic limit. Lower dimensional systems especially allow for new types of phenomena (such as localization) that can only occur with some amount of confinement. One-dimensional ensembles are attractive because transport occurs over longer length scales, and coherent states persist over longer time scales than similar higher-dimensional ensembles. The extension of scale can render certain experiments technically feasible that would never be for higher dimensional systems (such as the spin transport example above). The possibility of combining one-dimensional ensembles, a low-temperature vacuum chamber, and time-resolved stroboscopic measurements is an exciting one because it can provide a space-time resolved movie into physics otherwise only accessible through aggregate bulk observables.

Chapter 5

Conclusions

When we first decided to tackle the problem of optimizing miscut, it was not at all because we were looking to find a means of generating one-dimensional systems, but rather, we were only looking to optimize one (important) control parameter in an already established process. While we did accomplish our goal, we also unexpectedly found that the nitrogen in the hillocks was greatly enhanced and, not only that, formed very specific patterns determined by the shape of the hillocks. The unforeseen realization that the morphology of the diamond could be used to template specific, otherwise challenging-to-obtain systems of qubits was entirely unsought. Many important scientific results have been achieved via the familiar template of intense and creative theoretical work, followed by ingenious experimental design and much labor to finally realize whatever phenomenon the theorists originally predicted. However, there is a second kind of discovery where, while following the familiar template, the scientist encounters something strange - some result, feature, or conclusion that was not in any sense expected. It was this second kind of science that resulted in the one-dimensional work presented in Chapter 4. I think that it is exactly this capacity for nature to surprise that keeps me so intimately invested in the scientific endeavor.

The topics covered in this thesis have all centered around interactions in disordered dipolar systems. In particular, the discussion has revolved around how to *engineer* these systems at nearly every point. I hope that the work in this thesis forms a foundation for future investigations into the physics of low-dimensional many-body dipolar systems in diamond or other solid-state defects. While there are many concrete and testable experiments one can do with 1D and 2D systems of interacting spins, the real excitement, in my mind, is the possibility that while investigating physics in these systems (like MBL, spin diffusion, dipolar manipulation), something strange that at first, only serves to complicate what would otherwise be a very nice story - a discovery belonging to that second class of science - some piece of the puzzle that does not quite fit with the rest of the data or theory. My parting advice is to not brush that piece aside. In this final chapter, I will summarize the main results from this thesis and discuss their mutual relationship as well as possible future directions using some of these techniques.

In Chapter 2, we discussed CVD and the importance of managing the density of step edges (through control of the miscut). While these step edges control the growth rate, density of defects, and surface morphology, we have also shown how their natural symmetry breaking can lead to the patterning of specific, unusual geometries. The hillock, in particular, hosts an especially high density of nitrogen (owing to the high density of steps around the edge) and may be a compelling platform for exploring large number, quasi-one-dimensional many-body physics where periodic boundaries are desirable.

In Chapter 3, we discussed three-dimensional ensembles of NV centers and how to modify their Hamiltonian using a simple, sequence called ϵ-CPMG. Through careful analysis of the behavior under ϵ-CPMG, we deduce the importance of random on-site fields relative to dipolar interactions amongst the bath. This sequence also gives rise to long-lived coherent states that exhibit prethermal behavior, offering a probe into the thermodynamics of large N interacting systems of disordered spins. Periodic sequences

like ϵ-CPMG offer creative ways to introduce new Hamiltonians whose effects can give rise to unusual or unexplored physical regimes.

In Chapter 4, we tie the previous two chapters together. Using the analysis introduced through the study of 3D interacting systems, coupled with the dimensional control provided through CVD growth of diamond, we introduce novel types of systems for the exploration of topics in many-body physics. In this chapter, we have discussed ways of engineering two and one-dimensional ensembles of interacting spins and the possible physics one can explore using these systems. In particular, lower dimensional systems offer new routes for modifying the dipolar interaction.

While all of the results presented in this thesis use diamond-based qubits, the possibility for dimensional confinement in other solid-state platforms is quite realistic. None of the techniques or methods deployed here are necessarily specific to NV centers in diamond. With the possible exception of fundamentally 2D hosts (like hBN), delta-doping during growth is extendable to any grown solid-state system. Many of the engineering techniques presented in Chapter 2 and 4 are applicable to MBE[1] and the periodic drive presented in Chapter 3 is applicable to any system of disordered interacting dipoles. As other solid-state defects catch up to the NV, I suspect that, like with the NV, the need for precision spatial engineering in larger structures[2] will become as important as it has for NV centers. I rather expect that 2D layers made via doping will become a staple within the solid-state qubit community.

Two-dimensional layers of highly oriented coherent qubits, such as those in $\langle 111 \rangle$ diamond[3], offer new modes of sensing and access to fundamentally new physics, such as spin squeezing. One-dimensional systems offer the possibility of exploring either transport or

[1]Though, to be sure, there are important differences between the techniques, like the importance of adatom diffusion.

[2]For example, for probes or precise positioning within a waveguide

[3]Currently being pioneered by an especially talented researcher at UCSB.

many-body localization, as well as a variety of questions in quantum thermodynamics[4]. As my colleagues continue to investigate problems in many-body quantum mechanics, I am sure that they will make tremendous progress toward answering many of the unresolved questions in many-body quantum physics, but I must admit, I most eagerly anticipate that second class of discovery - those that are *unexpected*.

[4]These topics are being pursued by some equally talented researchers at UCSB.

Appendix A

Alternative approaches to understanding ϵ-CPMG

In this appendix, we will explore an alternative theoretical method for understanding the behavior of the system described in Chapter 3. While this alternative method has disadvantages compared to the method described in this thesis' main text, it offers some insight into the system for different limits. The method employed here may be more favorable for other sequences, so I include it here.

A.1 Magnus expansion analysis

Following Ref. [227], we use Average Hamiltonian Theory to derive the effective Hamiltonian used for the analytic fits shown in the main text. We use as our native Hamiltonian in the lab frame,

$$H = \sum_i B_i^z(t)\sigma_i^z + \sum_{i<j} J_{ij}\left(\sigma_i^x\sigma_j^x + \sigma_i^y\sigma_j^y - \sigma_i^z\sigma_j^z\right), \tag{A.1}$$

where the first summand is referred to as disorder or external interactions, the second summand contains the dipolar or internal interactions, B_i^z is the local onsite field at spin i, J_{ij} is the dipolar coupling between spins i and j, and $\sigma_i^{x,y,z}$ are the Pauli spin operators for the ith spin.

In the toggling frame that rotates with an angle $\pi + \epsilon$ at each pulse, the native Hamiltonian after the m^{th} pulse in this frame then becomes,

$$\begin{aligned} H_m = &\sum_i B_i^z(-1)^m[\sigma_i^z\cos(m\epsilon) + \sigma_i^x\sin(m\epsilon)] \\ &+ \sum_{i<j} J_{ij}[\sigma_i^y\sigma_j^y + \cos(2m\epsilon)(\sigma_i^x\sigma_j^x - \sigma_i^z\sigma_j^z) + \\ &+ \sin(2m\epsilon)(\sigma_i^x\sigma_j^z + \sigma_i^z\sigma_j^x)]. \end{aligned} \tag{A.2}$$

Now we consider the first two orders of corrections in the Mangus expansion for a total of N pulses,

$$\begin{aligned} \bar{H}^{(0)} &= \frac{1}{N}\sum_{m=0}^{N-1} H_m, \\ \bar{H}^{(1)} &= -\frac{\mathtt{i}\tau}{2N}\sum_{m<n}^{N-1}[H_m, H_n], \end{aligned} \tag{A.3}$$

where $\mathtt{i}$ is the imaginary unit.

In the following subsections we examine the 0^{th} order and 1^{st} order terms separately and examine the individual ϵ dependence of the disorder, dipolar and cross terms. We find that for large pulse number and finite ϵ, the 0^{th} order correction is only the $y-component$ of the dipolar part of the native Hamiltonian but for higher order corrections there is a non-trivial ϵ dependence.

A.1.1 0^{th} order terms

We will analyze these terms by examining the 0^{th} orders terms separated by disorder and dipolar contributions.

Disorder: 0^{th} order

The 0^{th} order terms for the disorder contribution take the form,

$$\begin{aligned}\bar{H}^{(0)}_{\text{disorder}} = \sum_i \{\sigma_i^z B_i^z \frac{1}{N}\sum_{n=0}^{N-1}(-1)^n \cos(n\epsilon) \\ +\sigma_i^x B_i^z \frac{1}{N}\sum_{n=0}^{N-1}(-1)^n \sin(n\epsilon)\}.\end{aligned} \tag{A.4}$$

Both terms oscillate quickly with epsilon and Eqn. A.4 approaches 0 as $N \to \infty$ for finite ϵ.

Dipolar: 0^{th} order

The 0^{th} order terms for the dipolar contribution take the form,

$$\begin{aligned}\bar{H}^{(0)}_{\text{dipolar}} = \sum_{j<i}\{J_{i,j}\sigma_i^y\sigma_j^y \\ +\frac{1}{N}[\sigma_i^x\sigma_j^x - \sigma_i^z\sigma_j^z]\sum_{n=0}^{N-1}\cos(2n\epsilon) \\ +\frac{1}{N}[\sigma_i^x\sigma_j^z - \sigma_i^z\sigma_j^x]\sum_{n=0}^{N-1}\sin(2n\epsilon)\}\end{aligned} \tag{A.5}$$

.

In the limit of $N \to \infty$, Eqn. A.5 approaches $\bar{H}^{(0)}_{\text{dipolar}} = \sum_{j<i} J_{i,j}\sigma_i^y\sigma_j^y$ for finite ϵ.

Thus we conclude that to 0^{th} order for large pulse number, the only term in the effective Hamiltonian is ϵ independent and is given by,

$$\bar{H}^{(0)} = \bar{H}^{(0)}_{\text{dipolar}} = \sum_{j<i} J_{i,j}\sigma_i^y\sigma_j^y \tag{A.6}$$

To understand the ϵ dependence in the pulse sequence we turn to the higher order terms in the Magnus expansion which do not vanish for large pulse numbers.

A.1.2 1^{st} order terms

We now calculate the first order terms in the Magnus expansion and separate them by the generating commutator.

For ease of readability, we introduce the following notation to describe two-body commutators. $[AB, CD]$ indicates all terms generated by

$$\bar{H}^{(1)}_{[\text{AB,CD}]} = [f(m,\epsilon)\sigma_i^A\sigma_j^B, f(n,\epsilon)\sigma_i^C\sigma_j^D] \tag{A.7}$$

, where $f(m,\epsilon)$ is a function that captures the ϵ dependence and A, B, C, D are arbitrary X, Y, Z coordinates. A slash in the commutator such as [YY/XX,YY/XX] indicates a sum over all possible permutations. Terms that follow $\sum_i B_i^z(-1)^m[\sigma_i^z\text{cos}(m\epsilon) + \sigma_i^x\text{sin}(m\epsilon)]$ will be denoted simply as 'disorder'. Three-body terms will be indexed explicitly with a subscript.

[Disorder, disorder]: 1^{st} order

We next evaluate the commutator between the disorder terms in the m^{th} and n^{th} cycles during the sequence. This correction is given by,

$$\bar{H}^{(1)}_{[\text{dis,dis}]} = \sum_i \frac{\tau}{2}(B_i^z)^2 \tan(\epsilon/2)\sigma_i^y \tag{A.8}$$

This term gives an effective field along the y-direction proportional to the variance of the onsite disorder field and the tangent of the rotation offset, ϵ.

[YY/XX/ZZ,YY/XX/ZZ]: 1st order

All terms of the form [YY,YY], [XX,XX] and [ZZ,ZZ] commute trivially and thus do not contribute first order corrections to the Mangus expansion. Terms of the form [YY,XX], [YY,ZZ] [XX,ZZ] result in expressions similar to,

$$\begin{aligned} \bar{H}^{(1)}_{[\text{YY,XX}]} = \\ \mathtt{i}\sum_{i<j}\frac{\tau}{2}(J_{i,j})^2\sum_{m<n}^{N-1}\cos(2m\epsilon)\cos(2n\epsilon)[\sigma_i^z\sigma_j^z - \sigma_j^z\sigma_i^z] \\ = 0. \end{aligned} \tag{A.9}$$

All terms of this form are zero and thus we conclude that all of the two-body [dipole, dipole] terms of the form [YY/XX/ZZ,YY/XX/ZZ] are zero and do not contribute first order corrections to the Magnus expansion.

[XX/ZZ,XZ/ZX] and [XZ/ZX,XX/ZZ]: 1st order

We examine those terms of the form [XX/ZZ,XZ/ZX] or [XZ/ZX,XX/ZZ]. Counter-intuitively, these two-body terms result in a sum of single-body expressions of the form $\sigma_i^y + \sigma_j^y$. Summing all of them, we arrive at the expression,

$$\bar{H}^{(1)}_{[\mathrm{XX/ZZ,XZ/ZX}]} + \bar{H}^{(1)}_{[\mathrm{XZ/ZX,XX/ZZ}]} = \sum_{i<j} \tau (J_{i,j})^2 \sum_{m<n}^{N-1} 4 \sin(2[m-n]\epsilon)(\sigma_i^y + \sigma_j^y). \tag{A.10}$$

In the limit of $N \to \infty$, this expression becomes,

$$\bar{H}^{(1)}_{[\mathrm{XX/ZZ,XZ/ZX}]} + \bar{H}^{(1)}_{[\mathrm{XZ/ZX,XX/ZZ}]} = \sum_{i<j} \tau (J_{i,j})^2 \cot(\epsilon)(\sigma_i^y + \sigma_j^y). \tag{A.11}$$

This term acts as another effective field that points along the y-direction with a strength proportional to the variance in the dipolar coupling constant and the cotangent of the rotation offset, ϵ.

$[XZ/ZX/YY, XZ/ZX]$: $1^{\mathbf{st}}$ order

These terms all commute with each other. The terms like [XZ,XZ] all commute with each other trivially. Terms like [XZ,ZX] result in expressions of the form

$$\begin{aligned} \bar{H}^{(1)}_{[\mathrm{XZ,ZX}]} = \\ \mathtt{i} \sum_{i<j} \frac{\tau}{2} (J_{i,j})^2 \sum_{m<n}^{N-1} \sin(2m\epsilon) \sin(2n\epsilon)[\sigma_i^y \sigma_j^y - \sigma_j^y \sigma_i^y] \\ = 0. \end{aligned} \tag{A.12}$$

Similarly, the [XZ,YY] term results in a similar expression proportional to $(\sigma_i^z \sigma_j^x - \sigma_j^x \sigma_i^z) = 0$. We conclude that all terms in this class commute and thus do not contribute

to first order corrections in the Magnus expansion. This conclude the examination of all two-body terms in the dipole-dipole commutator.

[Disorder,XX/YY/ZZ/XZ/ZX]: 1st order

We next discuss the effects of first-order corrections to the Magnus expansion involving the commutator of a disorder term with a dipolar term. An example of such a term is given by,

$$\bar{H}^{(1)}_{[\text{Disorder,YY}]} = \sum_{i<j} \frac{\tau}{2} J_{i,j} B_i \sum_{m<n}^{N-1} (-1)^m \cos(2m\epsilon) \sigma_i^x \sigma_j^y \neq 0. \tag{A.13}$$

Terms in this class do not go to zero even in the case of $N \to \infty$. We note that though these terms are non-zero, they will have zero mean and thus produce no net fields. Rather their effect will be decohering.

The first order average Hamiltonian resulting from these terms will be,

$$\bar{H}^{(1)}_{[\text{Disorder,YY}]} = \tau \tan(\epsilon/2) \sum_{i,j} B_i^z J_{ij} \sigma_i^z \sigma_j^y = \tan(\epsilon/2) \hat{A}. \tag{A.14}$$

We have grouped the spin operators, coupling terms and τ-dependence into the generic operator $\hat{A}$.

Three-body terms: 1^{st} order

Finally, we discuss terms in the dipole-dipole commutator that have only one overlapping site. Terms in this class constitute a three-body interaction. One such example would be the commutator of $[\mathrm{Y}_i\mathrm{Y}_j,\mathrm{X}_j\mathrm{X}_k]$. In this case, we would have,

$$\begin{aligned} \bar{H}^{(1)}_{[\mathrm{Y}_i\mathrm{Y}_j,\mathrm{X}_j\mathrm{X}_k]} = \\ \sum_{i<j} \frac{\tau}{2} J_{i,j}J_{j,k} \sum_{m<n}^{N-1} \cos(2n\epsilon)\sigma_i^y\sigma_j^z\sigma_k^x \neq 0. \end{aligned} \tag{A.15}$$

This term is not zero even in the limit as $N \to \infty$. Our treatment does not include three-body terms on the basis that the coefficients, $J_{i,j}J_{j,k}$, will have zero mean and so produce no net fields. While these terms produce no net fields, they still can result in decoherence. These terms result in,

$$\begin{aligned} \bar{H}^{(1)}_{[\mathrm{Y}_i\mathrm{Y}_j,\mathrm{X}_j\mathrm{X}_k]} = \\ \tau\cot(\epsilon)\{\sum_{i,j\neq q} J_{ij}J_{iq}\sigma_i^y(\sigma_i^{y+}\sigma_q^{y+} + \sigma_i^{y-}\sigma_q^{y-}) + \\ \sum_{i,j\neq q} J_{ij}J_{iq}(\sigma_i^x\sigma_j^y\sigma_q^x - \sigma_i^z\sigma_j^y\sigma_q^z)\} = \\ \cot(\epsilon)\hat{B}, \end{aligned} \tag{A.16}$$

where we have grouped the spin operators, coupling terms and τ-dependence into the generic operator $\hat{B}$.

A.1.3 Summary and resulting magnetization

Our final average Hamiltonian for the i^{th} spin, up to first order, will be,

$$\bar{H}_i = \sum_{j\neq i} \frac{1}{2}\{J_{i,j}\sigma_i^y\sigma_j^y + \frac{\tau}{2}[(B_i^z)^2\tan(\epsilon/2) + 2J_{i,j}^2\cot(\epsilon)]\ \sigma_i^y\} + \bar{H}_{\delta,i}. \tag{A.17}$$

We group the first order contribution from three-body interactions and [Disorder, dipolar] terms into $\bar{H}_{\delta,i}$,

$$\bar{H}_{\delta,i} = [\tan(\epsilon/2)\hat{A} + \cot(\epsilon)\hat{B}], \tag{A.18}$$

where $\hat{A}$ is the generic operator arising from the [Disorder, dipolar] terms and $\hat{B}$ is the operator arising from three-body dipolar interactions.

We note that $\bar{H}_i - \bar{H}_{\delta,i}$ is the Ising model with an epsilon-dependent effective field equal to $B_{eff} = \frac{\tau}{2}[(B_i^z)^2\tan(\epsilon/2) + 2J_{i,j}^2\cot(\epsilon)]$.

In this case, the equilibrium density matrix will be given by $\rho = e^{-\beta H}/Z$, where Z is the partition function. The average magnetization along y, will be given by,

$$\langle Y\rangle = \mathrm{Tr}\{\sum_i \sigma_i^y\rho\}. \tag{A.19}$$

Expanding this for $\beta H < 1$, $e^{-\beta H} \approx (1-\beta H)$ we arrive at,

$$\langle Y\rangle = -\beta\frac{\mathrm{Tr}\{\sum_i \sigma_i^y H\}}{Z}. \tag{A.20}$$

We also use,

$$\langle H\rangle = \mathrm{Tr}\{H\rho\} = \frac{\mathrm{Tr}\{H(1-\beta H)\}}{Z} = \\ -\frac{-\beta \mathrm{Tr}\{H^2\}}{Z} = \sum_i B_{eff,i} = N\langle B_{eff}\rangle \tag{A.21}$$

Using $\mathrm{Tr}\{\sum_i \sigma_i^y H\} = N\langle B_{eff}\rangle$ gives us the equation,

$$\langle Y\rangle = \frac{\langle B_{eff}\rangle^2}{\mathrm{Tr}\{H^2\}} \tag{A.22}$$

Using Eqn. A.17, the trace of H^2 will be given by $\mathrm{Tr}\{H^2\} = A^*\tan^2(\epsilon/2) + B^*\cot^2(\epsilon) + C^*\cot(\epsilon)\tan(\epsilon/2) + D^*$, where A^*, B^* and C^* include contributions from the effective field as well as those from $\bar{H}_{\delta,i}$. The D^* term is related to epsilon-independent dipolar coupling.

Using the effective field in Eqn. A.17 and the form of $\mathrm{Tr}\{H^2\}$, we arrive at the reduced expression,

$$\langle Y\rangle = \frac{[\tan(\epsilon/2) + \gamma\cot(\epsilon)]^2}{A\tan^2(\epsilon/2) + B\cot^2(\epsilon) + C\tan(\epsilon/2)\cot(\epsilon) + D}. \tag{A.23}$$

In this expression, $\gamma = \frac{\langle 2J_{i,j}^2\rangle}{\langle B_i^2\rangle}$ is a parameter that relates the relative strength of dipolar couplings within the system to on-site disordered fields, while A, B, C, and D are related to the strength of these interactions and the amount of decoherence the system has undergone.

Figure A.2 shows fits to the data in Chapter 3 using Eqn A.23. While the agreement between the data and this model is good, we ultimately abandoned this approach because we expect that the dipolar interactions have the most dramatic effect close to $\epsilon = 0°$ (and cause the pronounced dip). The expansion we used here requires periodicity; for small values of ϵ, this requirement cannot be met (since to be periodic, we require the number

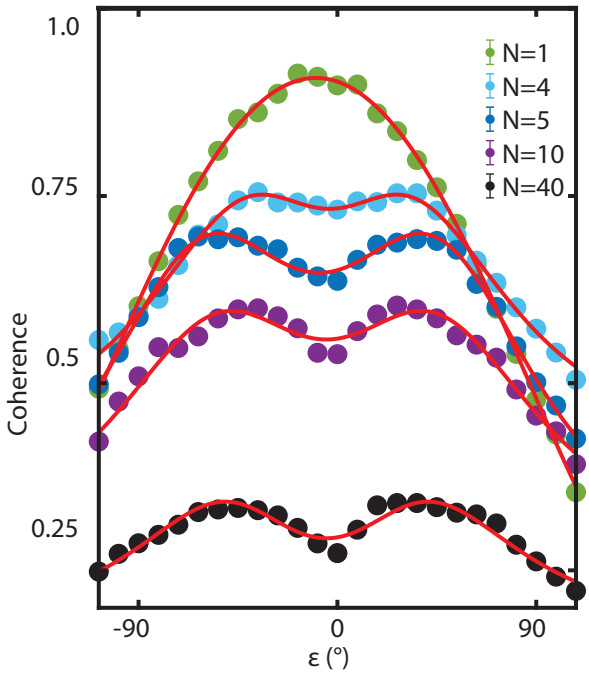

Figure A.1: Fits to the data in Chapter 3 using Eqn. A.23.

of pulses $N = 2\pi/\epsilon$). So, then, we expect this model to fail close to $\epsilon = 0$ where we find our most dramatic features. For other sequences where the periodic condition can be met, we expect that this model should have better validity.

A.2 Lindblad approach

While the thermodynamic approach employed thus far is compelling, there are certain assumptions in it whose validity may be in question. For example, the assumption of a spin temperature (and the additional assumption that this temperature is very high) may not be true for some systems. Another approach I want to briefly mention is the possibility of using a von Neumann[280] or Lindblad-type[228] approach.

While the von Neumann equation,

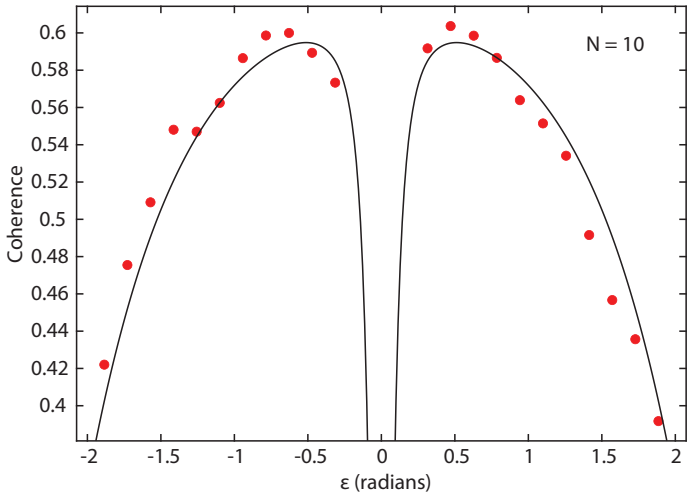

Figure A.2: Fits to the data in Chapter 3 using Eqn. A.27. Data close to $\epsilon = 0$ is removed because the Hamiltonian diverges at that point: we do not expect good agreement in the limit where $\epsilon \approx 0$ because $2\pi/\epsilon \gg N$.

$$\dot{\rho} = \frac{\mathtt{i}[\rho, \hat{H}]}{\hbar}, \tag{A.24}$$

is tractable for single-body (or two-body) problems, for large N problems, it requires solving a great many coupled differential equations.

However, we can map the many-body von Neumann approach onto a single-body Lindblad approach[229] using Lindblad's jump operators, $\hat{L}_i$, using the Lindblad equation,

$$\dot{\rho} = \frac{\mathtt{i}[\rho, \hat{H}_{\text{eff}}]}{\hbar} + \sum_i \gamma_i (\hat{L}_i \rho \hat{L}_i^\dagger - \frac{1}{2}\{\hat{L}_i^\dagger \hat{L}_i, \rho\}), \tag{A.25}$$

where the index i runs over the possible decoherence channels for the system (pathways for coherence to be lost to the environment) and $\{\hat{X}, \hat{Y}\}$ is the anticommutator between operators $\hat{X}$ and $\hat{Y}$. Starting with a fully $|\sigma^y\rangle$ state and inspecting the average Hamiltonian in Eqn. A.17, we can conclude that for short times, the only operators that

will decohere the state are the $\hat{A}$ and $\hat{B}$ operators. Thus, the Lindblad operators will have the corresponding coefficients ($\tan(\epsilon/2)$ and $\cot(\epsilon)$ respectively), and we expect for small times, the single-particle density matrix to evolve like,

$$\rho = \exp\{-(1 + A\tan^2(\epsilon/2) + B\cot^2(\epsilon))\tau/T_{1,\rho}\}\sigma^y, \tag{A.26}$$

leading then to a coherence of the form,

$$C = \exp\{-(1 + A\tan^2(\epsilon/2) + B\cot^2(\epsilon))\tau/T_{1,\rho}\}. \tag{A.27}$$

Ultimately, this approach suffers from the same problems as the previous approach (namely, it is not expected to fit well for $\epsilon \approx 0$). Nevertheless, there are cases where this approach might help to reduce the complexity of a many-body Hamiltonian and result in a solvable form.

Bibliography

[1] S. A. Meynell, C. A. McLellan, L. B. Hughes, W. Wang, T. E. Mates, K. Mukherjee, and A. C. Bleszynski Jayich, *Engineering quantum-coherent defects: The role of substrate miscut in chemical vapor deposition diamond growth*, *Applied Physics Letters* **117** (11, 2020) 194001, [https://pubs.aip.org/aip/apl/article-pdf/doi/10.1063/5.0029715/14540284/194001_1_online.pdf].

[2] W. K. Schenken, S. A. Meynell, F. Machado, B. Ye, C. A. McLellan, M. Joos, V. V. Dobrovitski, N. Y. Yao, and A. C. B. Jayich, *Long-lived coherences in strongly interacting spin ensembles*, 2023.

[3] "The Nobel Prize in Physics 1956, award ceremony speech — nobelprize.org nobel prize outreach ab." `https://www.nobelprize.org/prizes/physics/1956/ceremony-speech/`. [Accessed 03-12-2023].

[4] "The Nobel Prize in Physics 1966, award ceremony speech — nobelprize.org nobel prize outreach ab." `https://www.nobelprize.org/prizes/physics/1966/ceremony-speech/`. [Accessed 03-12-2023].

[5] "The Nobel Prize in Physics 2014, award ceremony speech — nobelprize.org nobel prize outreach ab." `https://www.nobelprize.org/prizes/physics/2014/ceremony-speech/`. [Accessed 03-12-2023].

[6] NIST, "The Second Quantum Revolution — nist.gov." `https://www.nist.gov/physics/introduction-new-quantum-revolution/second-quantum-revolution`, 2018, 2022. [Accessed 03-12-2023].

[7] M. Atzori and R. Sessoli, *The second quantum revolution: Role and challenges of molecular chemistry*, *Journal of the American Chemical Society* **141** (Jul, 2019) 11339–11352.

[8] D. Lu, B. Xu, N. Xu, Z. Li, H. Chen, X. Peng, R. Xu, and J. Du, *Quantum chemistry simulation on quantum computers: theories and experiments*, *Phys. Chem. Chem. Phys.* **14** (2012) 9411–9420.

[9] S. Wei, H. Li, and G. Long, *A full quantum eigensolver for quantum chemistry simulations*, *Research* **2020** (2020) [https://spj.science.org/doi/pdf/10.34133/2020/1486935].

[10] J. Argüello-Luengo, A. González-Tudela, T. Shi, P. Zoller, and J. I. Cirac, *Analogue quantum chemistry simulation*, *Nature* **574** (Oct, 2019) 215–218.

[11] J. R. Kirtley and J. P. Wikswo, *Scanning squid microscopy*, *Annual Review of Materials Science* **29** (1999), no. 1 117–148, [https://doi.org/10.1146/annurev.matsci.29.1.117].

[12] J. R. Maze, P. L. Stanwix, J. S. Hodges, S. Hong, J. M. Taylor, P. Cappellaro, L. Jiang, M. V. G. Dutt, E. Togan, A. S. Zibrov, A. Yacoby, R. L. Walsworth, and M. D. Lukin, *Nanoscale magnetic sensing with an individual electronic spin in diamond*, *Nature* **455** (Oct, 2008) 644–647.

[13] D. Vasyukov, Y. Anahory, L. Embon, D. Halbertal, J. Cuppens, L. Neeman, A. Finkler, Y. Segev, Y. Myasoedov, M. L. Rappaport, M. E. Huber, and E. Zeldov, *A scanning superconducting quantum interference device with single electron spin sensitivity*, *Nature Nanotechnology* **8** (Sep, 2013) 639–644.

[14] M. Pelliccione, A. Jenkins, P. Ovartchaiyapong, C. Reetz, E. Emmanouilidou, N. Ni, and A. C. Bleszynski Jayich, *Scanned probe imaging of nanoscale magnetism at cryogenic temperatures with a single-spin quantum sensor*, *Nature Nanotechnology* **11** (Aug, 2016) 700–705.

[15] F. Wolf and P. O. Schmidt, *Quantum sensing of oscillating electric fields with trapped ions*, *Measurement: Sensors* **18** (2021) 100271.

[16] M. T. Simons, A. B. Artusio-Glimpse, A. K. Robinson, N. Prajapati, and C. L. Holloway, *Rydberg atom-based sensors for radio-frequency electric field metrology, sensing, and communications*, *Measurement: Sensors* **18** (2021) 100273.

[17] C. L. Tschirhart, M. Serlin, H. Polshyn, A. Shragai, Z. Xia, J. Zhu, Y. Zhang, K. Watanabe, T. Taniguchi, M. E. Huber, and A. F. Young, *Imaging orbital ferromagnetism in a moiré chern insulator*, *Science* **372** (2021), no. 6548 1323–1327, [https://www.science.org/doi/pdf/10.1126/science.abd3190].

[18] F. Arute, K. Arya, R. Babbush, D. Bacon, J. C. Bardin, R. Barends, R. Biswas, S. Boixo, F. G. S. L. Brandao, D. A. Buell, B. Burkett, Y. Chen, Z. Chen, B. Chiaro, R. Collins, W. Courtney, A. Dunsworth, E. Farhi, B. Foxen, A. Fowler,

C. Gidney, M. Giustina, R. Graff, K. Guerin, S. Habegger, M. P. Harrigan, M. J. Hartmann, A. Ho, M. Hoffmann, T. Huang, T. S. Humble, S. V. Isakov, E. Jeffrey, Z. Jiang, D. Kafri, K. Kechedzhi, J. Kelly, P. V. Klimov, S. Knysh, A. Korotkov, F. Kostritsa, D. Landhuis, M. Lindmark, E. Lucero, D. Lyakh, S. Mandrà, J. R. McClean, M. McEwen, A. Megrant, X. Mi, K. Michielsen, M. Mohseni, J. Mutus, O. Naaman, M. Neeley, C. Neill, M. Y. Niu, E. Ostby, A. Petukhov, J. C. Platt, C. Quintana, E. G. Rieffel, P. Roushan, N. C. Rubin, D. Sank, K. J. Satzinger, V. Smelyanskiy, K. J. Sung, M. D. Trevithick, A. Vainsencher, B. Villalonga, T. White, Z. J. Yao, P. Yeh, A. Zalcman, H. Neven, and J. M. Martinis, *Quantum supremacy using a programmable superconducting processor*, *Nature* **574** (Oct, 2019) 505–510.

[19] M. A. Nielsen and I. L. Chuang, *Quantum computation and quantum information*. Cambridge university press, 2010.

[20] D. Bluvstein, A. Omran, H. Levine, A. Keesling, G. Semeghini, S. Ebadi, T. T. Wang, A. A. Michailidis, N. Maskara, W. W. Ho, S. Choi, M. Serbyn, M. Greiner, V. Vuletić, and M. D. Lukin, *Controlling quantum many-body dynamics in driven rydberg atom arrays*, *Science* **371** (2021), no. 6536 1355–1359, [https://www.science.org/doi/pdf/10.1126/science.abg2530].

[21] D. Bluvstein, H. Levine, G. Semeghini, T. T. Wang, S. Ebadi, M. Kalinowski, A. Keesling, N. Maskara, H. Pichler, M. Greiner, V. Vuletić, and M. D. Lukin, *A quantum processor based on coherent transport of entangled atom arrays*, *Nature* **604** (Apr, 2022) 451–456.

[22] M. Kim, J. Ahn, Y. Song, J. Moon, and H. Jeong, *Quantum computing with rydberg atom graphs*, *Journal of the Korean Physical Society* **82** (May, 2023) 827–840.

[23] E. L. Hahn, *Spin echoes*, *Phys. Rev.* **80** (Nov, 1950) 580–594.

[24] N. Kerker, R. Röpke, L. M. Steinert, A. Pooch, and A. Stibor, *Quantum decoherence by coulomb interaction*, *New Journal of Physics* **22** (jun, 2020) 063039.

[25] R. Konik, *Quantum coherence confined*, *Nature Physics* **17** (Jun, 2021) 669–670.

[26] J. M. Deutsch, *Eigenstate thermalization hypothesis*, *Reports on Progress in Physics* **81** (jul, 2018) 082001.

[27] V. M. Akulin, G. Kurizki, and D. A. Lidar, *How to control decoherence and entanglement in quantum complex systems?*, *Journal of Physics B: Atomic, Molecular and Optical Physics* **40** (may, 2007) E01.

[28] M. Schlosshauer, *Quantum decoherence*, *Physics Reports* **831** (2019) 1–57. Quantum decoherence.

[29] R. J. Glauber, *The quantum theory of optical coherence*, *Phys. Rev.* **130** (Jun, 1963) 2529–2539.

[30] G. Grynberg, A. Aspect, C. Fabre, and C. Cohen-Tannoudji, *Introduction to Quantum Optics: From the Semi-classical Approach to Quantized Light*. Cambridge University Press, 2010.

[31] M. Zhong, M. P. Hedges, R. L. Ahlefeldt, J. G. Bartholomew, S. E. Beavan, S. M. Wittig, J. J. Longdell, and M. J. Sellars, *Optically addressable nuclear spins in a solid with a six-hour coherence time*, *Nature* **517** (Jan, 2015) 177–180.

[32] P. Wang, C.-Y. Luan, M. Qiao, M. Um, J. Zhang, Y. Wang, X. Yuan, M. Gu, J. Zhang, and K. Kim, *Single ion qubit with estimated coherence time exceeding one hour*, *Nature Communications* **12** (Jan, 2021) 233.

[33] Y. Liu, W.-J. Zhang, C. Jiang, J.-P. Chen, C. Zhang, W.-X. Pan, D. Ma, H. Dong, J.-M. Xiong, C.-J. Zhang, H. Li, R.-C. Wang, J. Wu, T.-Y. Chen, L. You, X.-B. Wang, Q. Zhang, and J.-W. Pan, *Experimental twin-field quantum key distribution over 1000 km fiber distance*, *Phys. Rev. Lett.* **130** (May, 2023) 210801.

[34] E. Persky, I. Sochnikov, and B. Kalisky, *Studying quantum materials with scanning squid microscopy*, *Annual Review of Condensed Matter Physics* **13** (2022), no. 1 385–405, [https://doi.org/10.1146/annurev-conmatphys-031620-104226].

[35] S. Şahin, Özge Ergüder, L. Trabzon, and C. Ünlü, *16 - quantum dots for sensing applications*, in *Fundamentals of Sensor Technology* (A. Barhoum and Z. Altintas, eds.), Woodhead Publishing Series in Electronic and Optical Materials, pp. 443–473. Woodhead Publishing, 2023.

[36] L. T. Hall, J. H. Cole, C. D. Hill, and L. C. L. Hollenberg, *Sensing of fluctuating nanoscale magnetic fields using nitrogen-vacancy centers in diamond*, *Phys. Rev. Lett.* **103** (Nov, 2009) 220802.

[37] P. Maletinsky, S. Hong, M. S. Grinolds, B. Hausmann, M. D. Lukin, R. L. Walsworth, M. Loncar, and A. Yacoby, *A robust scanning diamond sensor for nanoscale imaging with single nitrogen-vacancy centres*, *Nature Nanotechnology* **7** (May, 2012) 320–324.

[38] S. Hong, M. S. Grinolds, L. M. Pham, D. Le Sage, L. Luan, R. L. Walsworth, and A. Yacoby, *Nanoscale magnetometry with nv centers in diamond*, *MRS Bulletin* **38** (Feb, 2013) 155–161.

[39] R. Schirhagl, K. Chang, M. Loretz, and C. L. Degen, *Nitrogen-vacancy centers in diamond: nanoscale sensors for physics and biology*, *Annu Rev Phys Chem* **65** (Nov., 2013) 83–105.

[40] N. Aslam, H. Zhou, E. K. Urbach, M. J. Turner, R. L. Walsworth, M. D. Lukin, and H. Park, *Quantum sensors for biomedical applications*, *Nature Reviews Physics* **5** (Mar, 2023) 157–169.

[41] "Quantum Design North America - Products - ProteusQ; Scanning NV Microscope - Quantum Magnetometry at Atomic Scale — qdusa.com." `https://qdusa.com/products/qnami_scanning_NV_microscope.html`. [Accessed 04-12-2023].

[42] "QSM - Quantum Scanning Microscope — qzabre.com." `https://qzabre.com/en/products/quantum-scanning-microscope`. [Accessed 04-12-2023].

[43] G. Wolfowicz, F. J. Heremans, C. P. Anderson, S. Kanai, H. Seo, A. Gali, G. Galli, and D. D. Awschalom, *Quantum guidelines for solid-state spin defects*, *Nature Reviews Materials* **6** (Oct, 2021) 906–925.

[44] F. J. Heremans, C. G. Yale, and D. D. Awschalom, *Control of spin defects in wide-bandgap semiconductors for quantum technologies*, *Proceedings of the IEEE* **104** (2016), no. 10 2009–2023.

[45] A. Dréau, M. Lesik, L. Rondin, P. Spinicelli, O. Arcizet, J.-F. Roch, and V. Jacques, *Avoiding power broadening in optically detected magnetic resonance of single nv defects for enhanced dc magnetic field sensitivity*, *Phys. Rev. B* **84** (Nov, 2011) 195204.

[46] D. Bluvstein, Z. Zhang, and A. C. B. Jayich, *Identifying and mitigating charge instabilities in shallow diamond nitrogen-vacancy centers*, *Phys. Rev. Lett.* **122** (Feb, 2019) 076101.

[47] N. Aslam, G. Waldherr, P. Neumann, F. Jelezko, and J. Wrachtrup, *Photo-induced ionization dynamics of the nitrogen vacancy defect in diamond investigated by single-shot charge state detection*, *New Journal of Physics* **15** (jan, 2013) 013064.

[48] V. Jacques, P. Neumann, J. Beck, M. Markham, D. Twitchen, J. Meijer, F. Kaiser, G. Balasubramanian, F. Jelezko, and J. Wrachtrup, *Dynamic polarization of single nuclear spins by optical pumping of nitrogen-vacancy color centers in diamond at room temperature*, *Phys. Rev. Lett.* **102** (Feb, 2009) 057403.

[49] T. Chakraborty, J. Zhang, and D. Suter, *Polarizing the electronic and nuclear spin of the nv-center in diamond in arbitrary magnetic fields: analysis of the optical pumping process*, *New Journal of Physics* **19** (jul, 2017) 073030.

[50] J. V. Cady, O. Michel, K. W. Lee, R. N. Patel, C. J. Sarabalis, A. H. Safavi-Naeini, and A. C. B. Jayich, *Diamond optomechanical crystals with embedded nitrogen-vacancy centers*, *Quantum Science and Technology* **4** (mar, 2019) 024009.

[51] M. Koppenhöfer, C. Padgett, J. V. Cady, V. Dharod, H. Oh, A. C. Bleszynski Jayich, and A. A. Clerk, *Single-spin readout and quantum sensing using optomechanically induced transparency*, *Phys. Rev. Lett.* **130** (Mar, 2023) 093603.

[52] P. Neumann, I. Jakobi, F. Dolde, C. Burk, R. Reuter, G. Waldherr, J. Honert, T. Wolf, A. Brunner, J. H. Shim, D. Suter, H. Sumiya, J. Isoya, and J. Wrachtrup, *High-precision nanoscale temperature sensing using single defects in diamond*, *Nano Letters* **13** (2013), no. 6 2738–2742, [https://doi.org/10.1021/nl401216y]. PMID: 23721106.

[53] A. Tchebotareva, S. L. N. Hermans, P. C. Humphreys, D. Voigt, P. J. Harmsma, L. K. Cheng, A. L. Verlaan, N. Dijkhuizen, W. de Jong, A. Dréau, and R. Hanson, *Entanglement between a diamond spin qubit and a photonic time-bin qubit at telecom wavelength*, *Phys. Rev. Lett.* **123** (Aug, 2019) 063601.

[54] C. J. Wort and R. S. Balmer, *Diamond as an electronic material*, *Materials Today* **11** (2008), no. 1 22–28.

[55] B. Mukherjee and A. J. F. Boyle, *On the debye characteristic temperature of diamond*, *physica status solidi (b)* **22** (1967), no. 2 K131–K134, [https://onlinelibrary.wiley.com/doi/pdf/10.1002/pssb.19670220259].

[56] C. M. Breeding, S. Eaton-Magaña, and J. E. Shigley, *Naturally colored yellow and orange gem diamonds: The nitrogen factor.*, *Gems & Gemology* **56** (2020), no. 2.

[57] E. Gaillou, J. E. Post, D. Rost, and J. E. Butler, *Boron in natural type IIb blue diamonds: Chemical and spectroscopic measurements*, *American Mineralogist* **97** (01, 2012) 1–18, [https://pubs.geoscienceworld.org/msa/ammin/article-pdf/97/1/1/3629994/1_3925GaillouC.pdf].

[58] E. Gaillou, J. Post, N. Bassim, A. Zaitsev, T. Rose, M. Fries, R. Stroud, A. Steele, and J. Butler, *Spectroscopic and microscopic characterizations of color lamellae in natural pink diamonds*, *Diamond and Related Materials* **19** (2010), no. 10 1207–1220.

[59] P. Scalisi, *The diamonds of india*, *Bridgewater Review* **10** (1992), no. 1 3–7.

[60] E. Gaillou and G. R. Rossman, *Color in natural diamonds: The beauty of defects*, *Rocks & Minerals* **89** (2014), no. 1 66–75, [https://doi.org/10.1080/00357529.2014.842839].

[61] A. Mzyk, Y. Ong, A. R. Ortiz Moreno, S. K. Padamati, Y. Zhang, C. A. Reyes-San-Martin, and R. Schirhagl, *Diamond color centers in diamonds for chemical and biochemical analysis and visualization*, *Analytical Chemistry* **94** (2022), no. 1 225–249, [https://doi.org/10.1021/acs.analchem.1c04536]. PMID: 34841868.

[62] G. Thiering and A. Gali, *Chapter one - color centers in diamond for quantum applications*, in *Diamond for Quantum Applications Part 1* (C. E. Nebel, I. Aharonovich, N. Mizuochi, and M. Hatano, eds.), vol. 103 of *Semiconductors and Semimetals*, pp. 1–36. Elsevier, 2020.

[63] K. D. Jahnke, A. Sipahigil, J. M. Binder, M. W. Doherty, M. Metsch, L. J. Rogers, N. B. Manson, M. D. Lukin, and F. Jelezko, *Electron–phonon processes of the silicon-vacancy centre in diamond*, *New Journal of Physics* **17** (apr, 2015) 043011.

[64] J. N. Becker and C. Becher, *Coherence properties and quantum control of silicon vacancy color centers in diamond*, *physica status solidi (a)* **214** (2017), no. 11 1700586, [https://onlinelibrary.wiley.com/doi/pdf/10.1002/pssa.201700586].

[65] D. D. Sukachev, A. Sipahigil, C. T. Nguyen, M. K. Bhaskar, R. E. Evans, F. Jelezko, and M. D. Lukin, *Silicon-vacancy spin qubit in diamond: A quantum memory exceeding 10 ms with single-shot state readout*, *Phys. Rev. Lett.* **119** (Nov, 2017) 223602.

[66] C. Bradac, W. Gao, J. Forneris, M. E. Trusheim, and I. Aharonovich, *Quantum nanophotonics with group iv defects in diamond*, *Nature Communications* **10** (Dec, 2019) 5625.

[67] U. Wahl, J. G. Correia, R. Villarreal, E. Bourgeois, M. Gulka, M. Nesládek, A. Vantomme, and L. M. C. Pereira, *Direct structural identification and quantification of the Split-Vacancy configuration for implanted sn in diamond*, *Phys Rev Lett* **125** (July, 2020) 045301.

[68] E. I. Rosenthal, C. P. Anderson, H. C. Kleidermacher, A. J. Stein, H. Lee, J. Grzesik, G. Scuri, A. E. Rugar, D. Riedel, S. Aghaeimeibodi, G. H. Ahn, K. Van Gasse, and J. Vučković, *Microwave spin control of a tin-vacancy qubit in diamond*, *Phys. Rev. X* **13** (Aug, 2023) 031022.

[69] T. Iwasaki, F. Ishibashi, Y. Miyamoto, Y. Doi, S. Kobayashi, T. Miyazaki, K. Tahara, K. D. Jahnke, L. J. Rogers, B. Naydenov, *et. al.*, *Germanium-vacancy single color centers in diamond*, *Scientific reports* **5** (2015), no. 1 12882.

[70] V. Nadolinny, A. Y. Komarovskikh, Y. N. Palyanov, I. Kupriyanov, Y. M. Borzdov, M. Rakhmanova, O. Yuryeva, and S. Veber, *Epr study of germanium-vacancy defects in diamonds*, *Journal of Structural Chemistry* **57** (2016) 1041–1043.

[71] S. Ditalia Tchernij, T. Luhmann, T. Herzig, J. Kupper, A. Damin, S. Santonocito, M. Signorile, P. Traina, E. Moreva, F. Celegato, *et. al.*, *Single-photon emitters in lead-implanted single-crystal diamond*, *Acs Photonics* **5** (2018), no. 12 4864–4871.

[72] M. E. Trusheim, N. H. Wan, K. C. Chen, C. J. Ciccarino, J. Flick, R. Sundararaman, G. Malladi, E. Bersin, M. Walsh, B. Lienhard, *et. al.*, *Lead-related quantum emitters in diamond*, *Physical Review B* **99** (2019), no. 7 075430.

[73] S. Simmons, *Scalable fault-tolerant quantum technologies with silicon colour centres*, 2023.

[74] D. B. Higginbottom, A. T. Kurkjian, C. Chartrand, M. Kazemi, N. A. Brunelle, E. R. MacQuarrie, J. R. Klein, N. R. Lee-Hone, J. Stacho, M. Ruether, *et. al.*, *Optical observation of single spins in silicon*, *Nature* **607** (2022), no. 7918 266–270.

[75] L. Bergeron, C. Chartrand, A. T. K. Kurkjian, K. J. Morse, H. Riemann, N. V. Abrosimov, P. Becker, H.-J. Pohl, M. L. W. Thewalt, and S. Simmons, *Silicon-integrated telecommunications photon-spin interface*, *PRX Quantum* **1** (Oct, 2020) 020301.

[76] E. R. MacQuarrie, C. Chartrand, D. B. Higginbottom, K. J. Morse, V. A. Karasyuk, S. Roorda, and S. Simmons, *Generating t centres in photonic silicon-on-insulator material by ion implantation*, *New Journal of Physics* **23** (oct, 2021) 103008.

[77] M. Prabhu, C. Errando-Herranz, L. De Santis, I. Christen, C. Chen, C. Gerlach, and D. Englund, *Individually addressable and spectrally programmable artificial atoms in silicon photonics*, *Nature Communications* **14** (Apr, 2023) 2380.

[78] L. Komza, P. Samutpraphoot, M. Odeh, Y.-L. Tang, M. Mathew, J. Chang, H. Song, M.-K. Kim, Y. Xiong, G. Hautier, and A. Sipahigil, *Indistinguishable photons from an artificial atom in silicon photonics*, 2022.

[79] Y. Baron, A. Durand, P. Udvarhelyi, T. Herzig, M. Khoury, S. Pezzagna, J. Meijer, I. Robert-Philip, M. Abbarchi, J.-M. Hartmann, V. Mazzocchi, J.-M. Gérard, A. Gali, V. Jacques, G. Cassabois, and A. Dréau, *Detection of single w-centers in silicon*, *ACS Photonics* **9** (Jul, 2022) 2337–2345.

[80] E. R. MacQuarrie, C. Simon, S. Simmons, and E. Maine, *The emerging commercial landscape of quantum computing*, *Nature Reviews Physics* **2** (Nov, 2020) 596–598.

[81] R. Gong, G. He, X. Gao, P. Ju, Z. Liu, B. Ye, E. A. Henriksen, T. Li, and C. Zu, *Coherent dynamics of strongly interacting electronic spin defects in hexagonal boron nitride*, *Nature Communications* **14** (Jun, 2023) 3299.

[82] W. Liu, N.-J. Guo, S. Yu, Y. Meng, Z.-P. Li, Y.-Z. Yang, Z.-A. Wang, X.-D. Zeng, L.-K. Xie, Q. Li, J.-F. Wang, J.-S. Xu, Y.-T. Wang, J.-S. Tang, C.-F. Li, and G.-C. Guo, *Spin-active defects in hexagonal boron nitride*, *Materials for Quantum Technology* **2** (jul, 2022) 032002.

[83] S. Castelletto and A. Boretti, *Silicon carbide color centers for quantum applications*, *Journal of Physics: Photonics* **2** (mar, 2020) 022001.

[84] M. Radulaski, M. Widmann, M. Niethammer, J. L. Zhang, S.-Y. Lee, T. Rendler, K. G. Lagoudakis, N. T. Son, E. Janzén, T. Ohshima, J. Wrachtrup, and J. Vučković, *Scalable quantum photonics with single color centers in silicon carbide*, *Nano Letters* **17** (2017), no. 3 1782–1786, [https://doi.org/10.1021/acs.nanolett.6b05102]. PMID: 28225630.

[85] K. Powell, L. Li, A. Shams-Ansari, J. Wang, D. Meng, N. Sinclair, J. Deng, M. Lončar, and X. Yi, *Integrated silicon carbide electro-optic modulator*, *Nature Communications* **13** (Apr, 2022) 1851.

[86] B. Lopez-Rodriguez, R. van der Kolk, S. Aggarwal, N. Sharma, Z. Li, D. van der Plaats, T. Scholte, J. Chang, S. Gröblacher, S. F. Pereira, H. Bhaskaran, and I. E. Zadeh, *High-quality amorphous silicon carbide for hybrid photonic integration deposited at a low temperature*, *ACS Photonics* **10** (2023), no. 10 3748–3754, [https://doi.org/10.1021/acsphotonics.3c00968].

[87] T. Ishikawa, K.-M. C. Fu, C. Santori, V. M. Acosta, R. G. Beausoleil, H. Watanabe, S. Shikata, and K. M. Itoh, *Optical and spin coherence properties of nitrogen-vacancy centers placed in a 100 nm thick isotopically purified diamond layer*, *Nano Letters* **12** (2012), no. 4 2083–2087, [https://doi.org/10.1021/nl300350r]. PMID: 22404419.

[88] K. Ohno, F. Joseph Heremans, L. C. Bassett, B. A. Myers, D. M. Toyli, A. C. Bleszynski Jayich, C. J. Palmstrøm, and D. D. Awschalom, *Engineering shallow spins in diamond with nitrogen delta-doping*, *Applied Physics Letters* **101** (08, 2012) 082413, [https://pubs.aip.org/aip/apl/article-pdf/doi/10.1063/1.4748280/14265520/082413_1_online.pdf].

[89] J. M. Smith, S. A. Meynell, A. C. B. Jayich, and J. Meijer, *Colour centre generation in diamond for quantum technologies*, *Nanophotonics* **8** (2019), no. 11 1889–1906.

[90] L. B. Hughes, Z. Zhang, C. Jin, S. A. Meynell, B. Ye, W. Wu, Z. Wang, E. J. Davis, T. E. Mates, N. Y. Yao, K. Mukherjee, and A. C. Bleszynski Jayich, *Two-dimensional spin systems in PECVD-grown diamond with tunable density and long coherence for enhanced quantum sensing and simulation*, *APL Materials* **11** (02, 2023) 021101, [https://pubs.aip.org/aip/apm/article-pdf/doi/10.1063/5.0133501/16695965/021101_1_online.pdf].

[91] M. V. Hauf, B. Grotz, B. Naydenov, M. Dankerl, S. Pezzagna, J. Meijer, F. Jelezko, J. Wrachtrup, M. Stutzmann, F. Reinhard, and J. A. Garrido, *Chemical control of the charge state of nitrogen-vacancy centers in diamond*, *Phys. Rev. B* **83** (Feb, 2011) 081304.

[92] M. Kaviani, P. Deák, B. Aradi, T. Frauenheim, J.-P. Chou, and A. Gali, *Proper surface termination for luminescent near-surface nv centers in diamond*, *Nano Letters* **14** (Aug, 2014) 4772–4777.

[93] V. Yurgens, J. A. Zuber, S. Flågan, M. De Luca, B. J. Shields, I. Zardo, P. Maletinsky, R. J. Warburton, and T. Jakubczyk, *Low-charge-noise nitrogen-vacancy centers in diamond created using laser writing with a solid-immersion lens*, *ACS Photonics* **8** (Jun, 2021) 1726–1734.

[94] S. Knauer, J. P. Hadden, and J. G. Rarity, *In-situ measurements of fabrication induced strain in diamond photonic-structures using intrinsic colour centres*, *npj Quantum Information* **6** (Jun, 2020) 50.

[95] L. Orphal-Kobin, K. Unterguggenberger, T. Pregnolato, N. Kemf, M. Matalla, R.-S. Unger, I. Ostermay, G. Pieplow, and T. Schröder, *Optically coherent nitrogen-vacancy defect centers in diamond nanostructures*, *Phys. Rev. X* **13** (Mar, 2023) 011042.

[96] D. P. L., *Electron paramagnetic resonance and optical investigations of defect centres in diamond*. PhD thesis, University of the Witwatersrand, Johannesburg, South Africa, 1965. 211 leaves.

[97] C. D. Clark and C. A. Norris, *Photoluminescence associated with the 1.673, 1.944 and 2.498 ev centres in diamond*, *Journal of Physics C: Solid State Physics* **4** (oct, 1971) 2223.

[98] G. Davies, *The effect of nitrogen impurity on the annealing of radiation damage in diamond*, *Journal of Physics C: Solid State Physics* **5** (sep, 1972) 2534.

[99] G. Davies, *Vibronic spectra in diamond*, *Journal of Physics C: Solid State Physics* **7** (1974) 3797–3809.

[100] G. Davies and M. F. Hamer, *Optical studies of the 1.945 ev vibronic band in diamond*, *Proceedings of the Royal Society of London. Series A, Mathematical and Physical Sciences* **348** (1976), no. 1653 285–298.

[101] L. V. H. Rodgers, L. B. Hughes, M. Xie, P. C. Maurer, S. Kolkowitz, A. C. Bleszynski Jayich, and N. P. de Leon, *Materials challenges for quantum technologies based on color centers in diamond*, *MRS Bulletin* **46** (Jul, 2021) 623–633.

[102] B. J. Shields, Q. P. Unterreithmeier, N. P. de Leon, H. Park, and M. D. Lukin, *Efficient readout of a single spin state in diamond via spin-to-charge conversion*, *Phys. Rev. Lett.* **114** (Mar, 2015) 136402.

[103] J. H. N. Loubser and J. A. van Wyk, *Electron spin resonance in the study of diamond*, *Reports on Progress in Physics* **41** (aug, 1978) 1201.

[104] A. T. Collins, M. F. Thomaz, and M. I. B. Jorge, *Luminescence decay time of the 1.945 ev centre in type ib diamond*, *Journal of Physics C: Solid State Physics* **16** (apr, 1983) 2177.

[105] D. A. Redman, S. Brown, R. H. Sands, and S. C. Rand, *Spin dynamics and electronic states of n-v centers in diamond by epr and four-wave-mixing spectroscopy*, *Phys. Rev. Lett.* **67** (Dec, 1991) 3420–3423.

[106] M. L. Goldman, M. W. Doherty, A. Sipahigil, N. Y. Yao, S. D. Bennett, N. B. Manson, A. Kubanek, and M. D. Lukin, *State-selective intersystem crossing in nitrogen-vacancy centers*, *Phys. Rev. B* **91** (Apr, 2015) 165201.

[107] G. D. Fuchs, V. V. Dobrovitski, R. Hanson, A. Batra, C. D. Weis, T. Schenkel, and D. D. Awschalom, *Excited-state spectroscopy using single spin manipulation in diamond*, *Phys. Rev. Lett.* **101** (Sep, 2008) 117601.

[108] E. V. Levine, M. J. Turner, P. Kehayias, C. A. Hart, N. Langellier, R. Trubko, D. R. Glenn, R. R. Fu, and R. L. Walsworth, *Principles and techniques of the quantum diamond microscope*, *Nanophotonics* **8** (2019), no. 11 1945–1973.

[109] J. R. Maze, A. Gali, E. Togan, Y. Chu, A. Trifonov, E. Kaxiras, and M. D. Lukin, *Properties of nitrogen-vacancy centers in diamond: the group theoretic approach*, *New Journal of Physics* **13** (feb, 2011) 025025.

[110] J. F. Barry, J. M. Schloss, E. Bauch, M. J. Turner, C. A. Hart, L. M. Pham, and R. L. Walsworth, *Sensitivity optimization for nv-diamond magnetometry*, *Rev. Mod. Phys.* **92** (Mar, 2020) 015004.

[111] A. Gruber, A. Dräbenstedt, C. Tietz, L. Fleury, J. Wrachtrup, and C. von Borczyskowski, *Scanning confocal optical microscopy and magnetic resonance on single defect centers*, *Science* **276** (1997), no. 5321 2012–2014, [https://www.science.org/doi/pdf/10.1126/science.276.5321.2012].

[112] F. Jelezko, T. Gaebel, I. Popa, M. Domhan, A. Gruber, and J. Wrachtrup, *Observation of coherent oscillation of a single nuclear spin and realization of a two-qubit conditional quantum gate*, *Phys. Rev. Lett.* **93** (Sep, 2004) 130501.

[113] L. Childress, M. V. G. Dutt, J. M. Taylor, A. S. Zibrov, F. Jelezko, J. Wrachtrup, P. R. Hemmer, and M. D. Lukin, *Coherent dynamics of coupled electron and nuclear spin qubits in diamond*, *Science* **314** (2006), no. 5797 281–285, [https://www.science.org/doi/pdf/10.1126/science.1131871].

[114] I. I. Rabi, *Space quantization in a gyrating magnetic field*, *Phys. Rev.* **51** (Apr, 1937) 652–654.

[115] P. Balasubramanian, C. Osterkamp, Y. Chen, X. Chen, T. Teraji, E. Wu, B. Naydenov, and F. Jelezko, *dc magnetometry with engineered nitrogen-vacancy spin ensembles in diamond*, *Nano Letters* **19** (2019), no. 9 6681–6686, [https://doi.org/10.1021/acs.nanolett.9b02993]. PMID: 31430171.

[116] S. Sengottuvel, M. Mrózek, M. Sawczak, M. J. Głowacki, M. Ficek, W. Gawlik, and A. M. Wojciechowski, *Wide-field magnetometry using nitrogen-vacancy color centers with randomly oriented micro-diamonds*, *Scientific Reports* **12** (Oct, 2022) 17997.

[117] M. S. Grinolds, P. Maletinsky, S. Hong, M. D. Lukin, R. L. Walsworth, and A. Yacoby, *Quantum control of proximal spins using nanoscale magnetic resonance imaging*, *Nature Physics* **7** (Sep, 2011) 687–692.

[118] P. J. Scheidegger, S. Diesch, M. L. Palm, and C. L. Degen, *Scanning nitrogen-vacancy magnetometry down to 350 mK*, *Applied Physics Letters* **120** (05, 2022) 224001, [https://pubs.aip.org/aip/apl/article-pdf/doi/10.1063/5.0093548/16449515/224001_1_online.pdf].

[119] S. Lin, C. Weng, Y. Yang, J. Zhao, Y. Guo, J. Zhang, L. Lou, W. Zhu, and G. Wang, *Temperature-dependent coherence properties of nv ensemble in diamond up to 600 k*, *Phys. Rev. B* **104** (Oct, 2021) 155430.

[120] S. Hsieh, P. Bhattacharyya, C. Zu, T. Mittiga, T. J. Smart, F. Machado, B. Kobrin, T. O. Höhn, N. Z. Rui, M. Kamrani, S. Chatterjee, S. Choi, M. Zaletel, V. V. Struzhkin, J. E. Moore, V. I. Levitas, R. Jeanloz, and N. Y. Yao, *Imaging stress and magnetism at high pressures using a nanoscale quantum sensor*, *Science* **366** (2019), no. 6471 1349–1354, [https://www.science.org/doi/pdf/10.1126/science.aaw4352].

[121] A. Jenkins, S. Baumann, H. Zhou, S. A. Meynell, Y. Daipeng, K. Watanabe, T. Taniguchi, A. Lucas, A. F. Young, and A. C. Bleszynski Jayich, *Imaging the breakdown of ohmic transport in graphene*, *Phys. Rev. Lett.* **129** (Aug, 2022) 087701.

[122] A. Hilberer, L. Toraille, C. Dailledouze, M.-P. Adam, L. Hanlon, G. Weck, M. Schmidt, P. Loubeyre, and J.-F. m. c. Roch, *Enabling quantum sensing under extreme pressure: Nitrogen-vacancy magnetometry up to 130 gpa*, *Phys. Rev. B* **107** (Jun, 2023) L220102.

[123] J. F. Barry, M. H. Steinecker, S. T. Alsid, J. Majumder, L. M. Pham, M. F. O'Keefe, and D. A. Braje, *Sensitive ac and dc magnetometry with nitrogen-vacancy center ensembles in diamond*, 2023.

[124] H. Zhou, J. Choi, S. Choi, R. Landig, A. M. Douglas, J. Isoya, F. Jelezko, S. Onoda, H. Sumiya, P. Cappellaro, H. S. Knowles, H. Park, and M. D. Lukin, *Quantum metrology with strongly interacting spin systems*, *Phys. Rev. X* **10** (Jul, 2020) 031003.

[125] D. Farfurnik, Y. Horowicz, N. Alfasi, S. Masis, Y. Kauffmann, E. Farchi, Y. Romach, Y. Hovav, E. Buks, and N. Bar-Gill, *Pursuing many-body dynamics of nv centers in diamond*, in *Frontiers in Optics 2017*, p. JW4A.17, Optica Publishing Group, 2017.

[126] J. Cai, A. Retzker, F. Jelezko, and M. B. Plenio, *A large-scale quantum simulator on a diamond surface at room temperature*, *Nature Physics* **9** (Mar, 2013) 168–173.

[127] C. Ju, C. Lei, X. Xu, D. Culcer, Z. Zhang, and J. Du, *Nv-center-based digital quantum simulation of a quantum phase transition in topological insulators*, *Phys. Rev. B* **89** (Jan, 2014) 045432.

[128] V. K. Sewani, H. H. Vallabhapurapu, Y. Yang, H. R. Firgau, C. Adambukulam, B. C. Johnson, J. J. Pla, and A. Laucht, *Coherent control of NV- centers in diamond in a quantum teaching lab*, *American Journal of Physics* **88** (12, 2020) 1156–1169, [https://pubs.aip.org/aapt/ajp/article-pdf/88/12/1156/13848918/1156_1_online.pdf].

[129] J. Stegemann, M. Peters, L. Horsthemke, N. Langels, P. Glösekötter, S. Heusler, and M. Gregor, *Modular low-cost 3d printed setup for experiments with nv centers in diamond*, *European Journal of Physics* **44** (apr, 2023) 035402.

[130] A. Lavoisier, *Premier memoire sur la destruction du diamant par le feu*, *Memoires de L'Academie Royale* (1772) 564.

[131] A. Lavoisier, *Second memoire sur la destruction du diamant par le feu*, *Memoires de L'Academie Royale* (1772) 591.

[132] S. Tennant, *Iv. on the nature of the diamond*, *Philosophical Transactions of the Royal Society of London* **87** (1797) 123–127, [https://royalsocietypublishing.org/doi/pdf/10.1098/rstl.1797.0005].

[133] T. H. M. II, *General electric chemist invented process for making diamonds in lab*, *Los Angeles Times* (2008).

[134] E. G. Lundblad, *High pressure synthesis of diamond in Sweden in 1953*, *AIP Conference Proceedings* **309** (07, 1994) 503–506, [https://pubs.aip.org/aip/acp/article-pdf/309/1/503/11885483/503_1_online.pdf].

[135] M. Werner and R. Locher, *Growth and application of undoped and doped diamond films*, *Reports on Progress in Physics* **61** (dec, 1998) 1665.

[136] W. G. Eversole, *Synthesis of diamond*, U.S. Patent US3030187A, 1958.

[137] A. Butcher, "A brief history of lab-grown diamonds." `https://www.gemsociety.org/article/brief-history-of-lab-grown-diamonds/`. Accessed: 2023-11-06.

[138] D. Araujo, M. Suzuki, F. Lloret, G. Alba, and P. Villar, *Diamond for electronics: Materials, processing and devices*, *Materials (Basel)* **14** (Nov., 2021).

[139] K. Ohno, *Nanometer-scale engineering of shallow spins in diamond*. PhD thesis, UCSB, 2014.

[140] B. A. Myers, *Quantum decoherence of near-surface nitrogen-vacancy centers in diamond and implications for nanoscale imaging*. PhD thesis, UCSB, 2016.

[141] C. A. McLellan, *Nitrogen-vacancy center ensembles in diamond: diamond growth and ensemble characterization for ensemble magnetometry*. PhD thesis, UCSB, 2018.

[142] F. P. Bundy, *The p, t phase and reaction diagram for elemental carbon, 1979*, *Journal of Geophysical Research: Solid Earth* **85** (1980), no. B12 6930–6936, [https://agupubs.onlinelibrary.wiley.com/doi/pdf/10.1029/JB085iB12p06930].

[143] F. Bundy, W. Bassett, M. Weathers, R. Hemley, H. Mao, and A. Goncharov, *The pressure-temperature phase and transformation diagram for carbon; updated through 1994*, *Carbon* **34** (1996), no. 2 141–153.

[144] Y.-Z. Wan, D. W. Zhang, Z.-J. Liu, and J.-T. Wang, *Effects of temperature and pressure on cvd diamond growth from the c-h-o system*, *Applied Physics A* **67** (Aug, 1998) 225–231.

[145] J. R. Petherbridge, P. W. May, S. R. J. Pearce, K. N. Rosser, and M. N. R. Ashfold, *Low temperature diamond growth using CO2/CH4 plasmas: Molecular beam mass spectrometry and computer simulation investigations*, *Journal of Applied Physics* **89** (01, 2001) 1484–1492, [https://pubs.aip.org/aip/jap/article-pdf/89/2/1484/10612526/1484_1_online.pdf].

[146] B. A. Reshi, S. Kumar, A. Misra, and R. Varma, *Multivariable study on growth of diamond on diamond substrates by microwave plasma chemical vapour deposition*, *Materials Research Express* **6** (jan, 2019) 046407.

[147] W. G. Leigh, J. A. Cuenca, E. L. Thomas, S. Mandal, and O. A. Williams, *Mapping the effect of substrate temperature inhomogeneity during microwave plasma-enhanced chemical vapour deposition nanocrystalline diamond growth*, *Carbon* **201** (2023) 328–337.

[148] X. Li, J. Perkins, R. Collazo, R. J. Nemanich, and Z. Sitar, *Investigation of the effect of the total pressure and methane concentration on the growth rate and quality of diamond thin films grown by mpcvd*, *Diamond and Related Materials* **15** (2006), no. 11 1784–1788. Proceedings of the joint 11th International Conference on New Diamond Science and Technology and the 9th Applied Diamond Conference 2006.

[149] C. Benndorf, I. Schmidt, and P. Joeris, *Fundamental gas processes for the cvd diamond growth from h2/c2/h2/o2 and ar/c2h2/o2 mixtures*, *physica status solidi (a)* **154** (1996), no. 1 5–21, [https://onlinelibrary.wiley.com/doi/pdf/10.1002/pssa.2211540103].

[150] V. Ralchenko, I. Sychov, I. Vlasov, A. Vlasov, V. Konov, A. Khomich, and S. Voronina, *Quality of diamond wafers grown by microwave plasma cvd: effects of gas flow rate*, *Diamond and Related Materials* **8** (1999), no. 2 189–193.

[151] J. Su, Y. Li, Y. Liu, M. Ding, and W. Tang, *Revisiting the gas flow rate effect on diamond films deposition with a new dome-shaped cavity type microwave plasma cvd reactor*, *Diamond and Related Materials* **73** (2017) 99–104. 10th International Conference on New Diamond and Nano Carbons – NDNC 2016.

[152] Y. V. Fedoseeva, D. V. Gorodetskiy, K. I. Baskakova, I. P. Asanov, L. G. Bulusheva, A. A. Makarova, I. B. Yudin, M. Y. Plotnikov, A. A. Emelyanov, A. K. Rebrov, and A. V. Okotrub, *Structure of diamond films grown using High-Speed flow of a thermally activated CH(4)-H(2) gas mixture*, *Materials (Basel)* **13** (Jan., 2020).

[153] Z. Yiming, F. Larsson, and K. Larsson, *Effect of cvd diamond growth by doping with nitrogen*, *Theoretical Chemistry Accounts* **133** (Dec, 2013) 1432.

[154] G. Wu, Q. Wang, Y. Wu, X. Sun, J. Liao, J. Pan, M. Chen, M. Kasu, and S. Liu, *Evolution of defects, morphologies and fundamental growth characteristics of cvd diamond films induced by nitrogen addition*, *Materials Today Communications* **25** (2020) 101504.

[155] T.-H. Chein, J. Wei, and Y. Tzeng, *Synthesis of diamond in high power-density microwave methane/hydrogen/oxygen plasmas at elevated substrate temperatures*, *Diamond and Related Materials* **8** (1999), no. 8 1686–1696.

[156] C. Lin, C. Su, C. Hung, C. Chang, and S.-H. Yan, *The effect of the substrate position on microwave plasma chemical vapor deposition of diamond films*, *Surface and Coatings Technology* **200** (2006), no. 10 3156–3159. Proceedings of The Third Asian Conference on Chemical Vapor Deposition (Third Asian-CVD).

[157] S. J. Harris and D. G. Goodwin, *Growth on the reconstructed diamond (100) surface*, *The Journal of Physical Chemistry* **97** (Jan, 1993) 23–28.

[158] M. Frenklach, S. Skokov, and B. Weiner, *An atomistic model for stepped diamond growth*, *Nature* **372** (Dec, 1994) 535–537.

[159] M. Frenklach and S. Skokov, *Surface migration in diamond growth*, *The Journal of Physical Chemistry B* **101** (Apr, 1997) 3025–3036.

[160] K. Hayashi, S. Yamanaka, H. Watanabe, T. Sekiguchi, H. Okushi, and K. Kajimura, *Diamond films epitaxially grown by step-flow mode*, *Journal of Crystal Growth* **183** (1998), no. 3 338–346.

[161] J. Y. Tsao, *Chapter 6 - surface morphology*, in *Materials Fundamentals of Molecular Beam Epitaxy* (J. Y. Tsao, ed.), pp. 201–257. Academic Press, San Diego, 1993.

[162] W. H. Bragg and W. L. Bragg, *The reflection of x-rays by crystals*, *Proceedings of the Royal Society of London. Series A, Containing Papers of a Mathematical and Physical Character* **88** (July, 1913) 428–438.

[163] L. D. Doucette, M. Pereira da Cunha, and R. J. Lad, *Precise orientation of single crystals by a simple x-ray diffraction rocking curve method*, Mar, 2005.

[164] "en-About Syntek — syntek.co.jp." `https://www.syntek.co.jp/en/about/`. [Accessed 05-12-2023].

[165] P. Udvarhelyi, V. O. Shkolnikov, A. Gali, G. Burkard, and A. Pályi, *Spin-strain interaction in nitrogen-vacancy centers in diamond*, *Phys. Rev. B* **98** (Aug, 2018) 075201.

[166] S. Dolabella, A. Borzì, A. Dommann, and A. Neels, *Lattice strain and defects analysis in nanostructured semiconductor materials and devices by high-resolution x-ray diffraction: Theoretical and practical aspects*, *Small Methods* **6** (2022), no. 2 2100932, [https://onlinelibrary.wiley.com/doi/pdf/10.1002/smtd.202100932].

[167] G. Nowak, K. Pakuła, I. Grzegory, J. Weyher, and S. Porowski, *Dislocation structure of growth hillocks in homoepitaxial gan*, *physica status solidi (b)* **216** (1999), no. 1 649–654.

[168] A. Tallaire, M. Kasu, K. Ueda, and T. Makimoto, *Origin of growth defects in cvd diamond epitaxial films*, *Diamond and Related Materials* **17** (2008), no. 1 60–65.

[169] A. J. Shahani, E. B. Gulsoy, S. O. Poulsen, X. Xiao, and P. W. Voorhees, *Twin-mediated crystal growth: an enigma resolved*, *Scientific Reports* **6** (Jun, 2016) 28651.

[170] R. Wagner, *On the growth of germanium dendrites*, *Acta metallurgica* **8** (1960), no. 1 57–60.

[171] D. Hamilton and R. Seidensticker, *Propagation mechanism of germanium dendrites*, *Journal of Applied Physics* **31** (1960), no. 7 1165–1168.

[172] A. HOLMES, *The giant's causeway*, *Nature* **156** (Oct, 1945) 425–426.

[173] "Saturn's Hexagon in Motion - NASA Science — science.nasa.gov." `https://science.nasa.gov/mission/cassini/science/saturn/hexagon-in-motion/`. [Accessed 10-11-2023].

[174] I. Newton, A. Motte, and J. Machin, *The Mathematical Principles of Natural Philosophy*. No. v. 1 in The Mathematical Principles of Natural Philosophy. B. Motte, 1729.

[175] "Ammonites - British Geological Survey — bgs.ac.uk." `https://www.bgs.ac.uk/discovering-geology/fossils-and-geological-time/ammonites/`. [Accessed 05-12-2023].

[176] J. Resag, *The Life and Science of an Extraordinary Man*. Springer Cham, Switzerland, 2018.

[177] R. P. Feynman, *Simulating physics with computers*, *International Journal of Theoretical Physics* **21** (Jun, 1982) 467–488.

[178] H. IT, "How big is the internet, and how do we measure it? — healthit.com.au." `https://healthit.com.au/how-big-is-the-internet-and-how-do-we-measure-it/#:~:text=Zetabytes,and%20consumed%20on%20the%20web.` [Accessed 12-11-2023].

[179] "How Big Is The Internet? Hint: Probably A Lot Bigger Than You Think — starry.com."
https://starry.com/blog/inside-the-internet/how-big-is-the-internet. [Accessed 12-11-2023].

[180] I. M. Georgescu, S. Ashhab, and F. Nori, *Quantum simulation*, *Rev. Mod. Phys.* **86** (Mar, 2014) 153–185.

[181] H. Weimer, M. Müller, I. Lesanovsky, P. Zoller, and H. P. Büchler, *A rydberg quantum simulator*, *Nature Physics* **6** (May, 2010) 382–388.

[182] R. Senaratne, S. V. Rajagopal, T. Shimasaki, P. E. Dotti, K. M. Fujiwara, K. Singh, Z. A. Geiger, and D. M. Weld, *Quantum simulation of ultrafast dynamics using trapped ultracold atoms*, *Nature Communications* **9** (May, 2018) 2065.

[183] J. Struck, C. Ölschläger, R. L. Targat, P. Soltan-Panahi, A. Eckardt, M. Lewenstein, P. Windpassinger, and K. Sengstock, *Quantum simulation of frustrated classical magnetism in triangular optical lattices*, *Science* **333** (2011), no. 6045 996–999, [https://www.science.org/doi/pdf/10.1126/science.1207239].

[184] R. Blatt and C. F. Roos, *Quantum simulations with trapped ions*, *Nature Physics* **8** (Apr, 2012) 277–284.

[185] C. Monroe, W. C. Campbell, L.-M. Duan, Z.-X. Gong, A. V. Gorshkov, P. W. Hess, R. Islam, K. Kim, N. M. Linke, G. Pagano, P. Richerme, C. Senko, and N. Y. Yao, *Programmable quantum simulations of spin systems with trapped ions*, *Rev. Mod. Phys.* **93** (Apr, 2021) 025001.

[186] X. Peng, J. Zhang, J. Du, and D. Suter, *Quantum simulation of a system with competing two- and three-body interactions*, *Phys. Rev. Lett.* **103** (Sep, 2009) 140501.

[187] R. Hanson and D. D. Awschalom, *Coherent manipulation of single spins in semiconductors*, *Nature* **453** (Jun, 2008) 1043–1049.

[188] A. A. Houck, H. E. Türeci, and J. Koch, *On-chip quantum simulation with superconducting circuits*, *Nature Physics* **8** (Apr, 2012) 292–299.

[189] S. A. Wilkinson and M. J. Hartmann, *Superconducting quantum many-body circuits for quantum simulation and computing*, *Applied Physics Letters* **116** (2020), no. 23.

[190] D. A. Lidar and O. Biham, *Simulating ising spin glasses on a quantum computer*, *Phys. Rev. E* **56** (Sep, 1997) 3661–3681.

[191] N. Roy, A. Sharma, and R. Mukherjee, *Quantum simulation of long-range xy quantum spin glass with strong area-law violation using trapped ions*, *Phys. Rev. A* **99** (May, 2019) 052342.

[192] F. Mei, V. M. Stojanović, I. Siddiqi, and L. Tian, *Analog superconducting quantum simulator for holstein polarons*, *Phys. Rev. B* **88** (Dec, 2013) 224502.

[193] W. Hofstetter and T. Qin, *Quantum simulation of strongly correlated condensed matter systems*, *Journal of Physics B: Atomic, Molecular and Optical Physics* **51** (mar, 2018) 082001.

[194] P. Scholl, M. Schuler, H. J. Williams, A. A. Eberharter, D. Barredo, K.-N. Schymik, V. Lienhard, L.-P. Henry, T. C. Lang, T. Lahaye, A. M. Läuchli, and A. Browaeys, *Quantum simulation of 2d antiferromagnets with hundreds of rydberg atoms*, *Nature* **595** (Jul, 2021) 233–238.

[195] S. Warren, L. M. Sager-Smith, and D. A. Mazziotti, *Quantum simulation of quantum phase transitions using the convex geometry of reduced density matrices*, *Phys. Rev. A* **106** (Jul, 2022) 012434.

[196] T. Hensgens, T. Fujita, L. Janssen, X. Li, C. J. Van Diepen, C. Reichl, W. Wegscheider, S. Das Sarma, and L. M. K. Vandersypen, *Quantum simulation of a fermi–hubbard model using a semiconductor quantum dot array*, *Nature* **548** (Aug, 2017) 70–73.

[197] H.-H. Lu, N. Klco, J. M. Lukens, T. D. Morris, A. Bansal, A. Ekström, G. Hagen, T. Papenbrock, A. M. Weiner, M. J. Savage, and P. Lougovski, *Simulations of subatomic many-body physics on a quantum frequency processor*, *Phys. Rev. A* **100** (Jul, 2019) 012320.

[198] W. A. de Jong, M. Metcalf, J. Mulligan, M. Płoskoń, F. Ringer, and X. Yao, *Quantum simulation of open quantum systems in heavy-ion collisions*, *Phys. Rev. D* **104** (Sep, 2021) L051501.

[199] N.-N. Zhang, M.-J. Tao, W.-T. He, X.-Y. Chen, X.-Y. Kong, F.-G. Deng, N. Lambert, and Q. Ai, *Efficient quantum simulation of open quantum dynamics at various hamiltonians and spectral densities*, *Frontiers of Physics* **16** (Mar, 2021) 51501.

[200] C. Lei, S. Peng, C. Ju, M.-H. Yung, and J. Du, *Decoherence control of nitrogen-vacancy centers*, *Scientific Reports* **7** (Sep, 2017) 11937.

[201] S. Hernández-Gómez, N. Staudenmaier, M. Campisi, and N. Fabbri, *Experimental test of fluctuation relations for driven open quantum systems with an nv center*, *New Journal of Physics* **23** (jun, 2021) 065004.

[202] I. V. Martynenko, V. Ruider, M. Dass, T. Liedl, and P. C. Nickels, *Dna origami meets bottom-up nanopatterning*, *ACS Nano* **15** (Jul, 2021) 10769–10774.

[203] S. Kogikoski, Jr, J. Ameixa, A. Mostafa, and I. Bald, *Lab-on-a-DNA origami: nanoengineered single-molecule platforms*, *Chem Commun (Camb)* **59** (Apr., 2023) 4726–4741.

[204] T. Mori, *Floquet states in open quantum systems*, *Annual Review of Condensed Matter Physics* **14** (2023), no. 1 35–56, [https://doi.org/10.1146/annurev-conmatphys-040721-015537].

[205] E. Fraczek, V. G. Savitski, M. Dale, B. G. Breeze, P. Diggle, M. Markham, A. Bennett, H. Dhillon, M. E. Newton, and A. J. Kemp, *Laser spectroscopy of nv- and nv0 colour centres in synthetic diamond*, *Opt. Mater. Express* **7** (Jul, 2017) 2571–2585.

[206] T. Wolf, P. Neumann, K. Nakamura, H. Sumiya, T. Ohshima, J. Isoya, and J. Wrachtrup, *Subpicotesla diamond magnetometry*, *Phys. Rev. X* **5** (Oct, 2015) 041001.

[207] H. Y. Carr and E. M. Purcell, *Effects of diffusion on free precession in nuclear magnetic resonance experiments*, *Phys. Rev.* **94** (May, 1954) 630–638.

[208] S. Meiboom and D. Gill, *Modified spin-echo method for measuring nuclear relaxation times*, *Review of Scientific Instruments* **29** (1958), no. 8 688–691, [https://doi.org/10.1063/1.1716296].

[209] E. D. Ostroff and J. S. Waugh, *Multiple spin echoes and spin locking in solids*, *Phys. Rev. Lett.* **16** (Jun, 1966) 1097–1098.

[210] J. S. Waugh, C. H. Wang, L. M. Huber, and R. L. Vold, *Multiple-pulse NMR experiments*, *The Journal of Chemical Physics* **48** (1968), no. 2 662–670, [https://doi.org/10.1063/1.1668698].

[211] C. A. McLellan, B. A. Myers, S. Kraemer, K. Ohno, D. D. Awschalom, and A. C. Bleszynski Jayich, *Patterned formation of highly coherent nitrogen-vacancy centers using a focused electron irradiation technique*, *Nano Letters* **16** (Apr, 2016) 2450–2454.

[212] T. R. Eichhorn, C. A. McLellan, and A. C. Bleszynski Jayich, *Optimizing the formation of depth-confined nitrogen vacancy center spin ensembles in diamond for quantum sensing*, *Phys. Rev. Mater.* **3** (Nov, 2019) 113802.

[213] B. Suh, F. Borsa, and D. Torgeson, *Use of an alternating-phase cpmg sequence to avoid spin-locking effects in t2 measurements in solids*, *Journal of Magnetic Resonance, Series A* **110** (1994), no. 1 58–61.

[214] M. J. Biercuk, A. C. Doherty, and H. Uys, *Dynamical decoupling sequence construction as a filter-design problem*, *Journal of Physics B: Atomic, Molecular and Optical Physics* **44** (jul, 2011) 154002.

[215] C. L. Degen, F. Reinhard, and P. Cappellaro, *Quantum sensing*, *Rev. Mod. Phys.* **89** (Jul, 2017) 035002.

[216] L. Cywiński, R. M. Lutchyn, C. P. Nave, and S. Das Sarma, *How to enhance dephasing time in superconducting qubits*, *Phys. Rev. B* **77** (May, 2008) 174509.

[217] A. Milov, K. Salikhov, and M. Shirov, *Application of eldor in electron-spin echo for paramagnetic center space distribution in solids*, *Fizika Tverdogo Tela* **23** (1981), no. 4 975–982.

[218] A. Milov, A. Ponomarev, and Y. Tsvetkov, *Electron-electron double resonance in electron spin echo: Model biradical systems and the sensitized photolysis of decalin*, *Chemical Physics Letters* **110** (1984), no. 1 67–72.

[219] H. J. Mamin, M. H. Sherwood, and D. Rugar, *Detecting external electron spins using nitrogen-vacancy centers*, *Phys. Rev. B* **86** (Nov, 2012) 195422.

[220] S. R. Sweger, V. P. Denysenkov, L. Maibaum, T. F. Prisner, and S. Stoll, *The effect of spin polarization on double electron–electron resonance (deer) spectroscopy*, *Magnetic Resonance* **3** (2022), no. 1 101–110.

[221] T. Mikawa, R. Okaniwa, Y. Matsuzaki, N. Tokuda, and J. Ishi-Hayase, *Electron-spin double resonance of nitrogen-vacancy centers in diamond under a strong driving field*, *Phys. Rev. A* **108** (Jul, 2023) 012610.

[222] E. Bauch, S. Singh, J. Lee, C. A. Hart, J. M. Schloss, M. J. Turner, J. F. Barry, L. M. Pham, N. Bar-Gill, S. F. Yelin, and R. L. Walsworth, *Decoherence of ensembles of nitrogen-vacancy centers in diamond*, *Phys. Rev. B* **102** (Oct, 2020) 134210.

[223] D. Li, *Unexpected spin echoes in dipolar solids: Intrinsic effects of finite pi pulses on quantum coherence*, 2007. Ph.d. thesis, Yale University.

[224] W. Hahn and V. V. Dobrovitski, *Long-lived coherence in driven many-spin systems: from two to infinite spatial dimensions*, *New Journal of Physics* **23** (jul, 2021) 073029.

[225] E. B. Fel'dman and S. Lacelle, *Configurational averaging of dipolar interactions in magnetically diluted spin networks*, *The Journal of Chemical Physics* **104** (1996), no. 5 2000–2009, [https://doi.org/10.1063/1.470956].

[226] W. Magnus, *On the exponential solution of differential equations for a linear operator*, *Communications on Pure and Applied Mathematics* **7** (1954), no. 4 649–673, [https://onlinelibrary.wiley.com/doi/pdf/10.1002/cpa.3160070404].

[227] C. P. Slichter, *Principles of Magnetic Resonance*. Springer-Verlag, Heidelberg, Germany, 3 ed., 1989.

[228] G. Lindblad, *On the generators of quantum dynamical semigroups*, *Communications in Mathematical Physics* **48** (1976), no. 2 119 – 130.

[229] D. Manzano, *A short introduction to the Lindblad master equation*, *AIP Advances* **10** (02, 2020) 025106, [https://pubs.aip.org/aip/adv/article-pdf/doi/10.1063/1.5115323/12881278/025106_1_online.pdf].

[230] J. R. Klauder and P. W. Anderson, *Spectral diffusion decay in spin resonance experiments*, *Phys. Rev.* **125** (Feb, 1962) 912–932.

[231] V. V. Dobrovitski, A. E. Feiguin, D. D. Awschalom, and R. Hanson, *Decoherence dynamics of a single spin versus spin ensemble*, *Phys. Rev. B* **77** (Jun, 2008) 245212.

[232] A. Eddington, *The nature of the physical world: THE GIFFORD LECTURES 1927*, vol. 23. BoD–Books on Demand, 2019,1927.

[233] H. Callen, *Thermodynamics and an Introduction to Thermostatistics*. Wiley, 1991.

[234] J. C. MAXWELL, *Clerk-maxwell's kinetic theory of gases*, *Nature* **8** (May, 1873) 85–85.

[235] J. C. Maxwell and P. Pesic, *Theory of heat*. Courier Corporation, 2001,1871.

[236] L. Boltzmann, *Lectures on Gas Theory*. University of California Press, Berkeley, 2023,1896.

[237] J. L. Lebowitz, *Boltzmann's entropy and time's arrow*, *Physics today* **46** (1993), no. 9 32–38.

[238] M. Srednicki, *Chaos and quantum thermalization*, *Phys. Rev. E* **50** (Aug, 1994) 888–901.

[239] M. Srednicki, *The approach to thermal equilibrium in quantized chaotic systems*, *Journal of Physics A: Mathematical and General* **32** (feb, 1999) 1163.

[240] S. Hortikar and M. Srednicki, *Random matrix elements and eigenfunctions in chaotic systems*, *Phys. Rev. E* **57** (Jun, 1998) 7313–7316.

[241] P. W. Anderson, *Absence of diffusion in certain random lattices*, *Phys. Rev.* **109** (Mar, 1958) 1492–1505.

[242] F. Bloch, *Über die quantenmechanik der elektronen in kristallgittern*, *Zeitschrift für Physik* **52** (Jul, 1929) 555–600.

[243] M. Serbyn, Z. Papić, and D. A. Abanin, *Local conservation laws and the structure of the many-body localized states*, *Phys. Rev. Lett.* **111** (Sep, 2013) 127201.

[244] M. Serbyn, M. Knap, S. Gopalakrishnan, Z. Papić, N. Y. Yao, C. R. Laumann, D. A. Abanin, M. D. Lukin, and E. A. Demler, *Interferometric probes of many-body localization*, *Phys. Rev. Lett.* **113** (Oct, 2014) 147204.

[245] N. Y. Yao, C. R. Laumann, S. Gopalakrishnan, M. Knap, M. Müller, E. A. Demler, and M. D. Lukin, *Many-body localization in dipolar systems*, *Phys. Rev. Lett.* **113** (Dec, 2014) 243002.

[246] R. Nandkishore and D. A. Huse, *Many-body localization and thermalization in quantum statistical mechanics*, *Annual Review of Condensed Matter Physics* **6** (2015), no. 1 15–38, [https://doi.org/10.1146/annurev-conmatphys-031214-014726].

[247] D. Hetterich, N. Y. Yao, M. Serbyn, F. Pollmann, and B. Trauzettel, *Detection and characterization of many-body localization in central spin models*, *Phys. Rev. B* **98** (Oct, 2018) 161122.

[248] D. A. Abanin, E. Altman, I. Bloch, and M. Serbyn, *Colloquium: Many-body localization, thermalization, and entanglement*, *Rev. Mod. Phys.* **91** (May, 2019) 021001.

[249] E. Altman, *Many-body localization and quantum thermalization*, *Nature Physics* **14** (Oct, 2018) 979–983.

[250] R. Nandkishore and S. Gopalakrishnan, *Lifetimes of local excitations in disordered dipolar quantum systems*, *Phys. Rev. B* **103** (Apr, 2021) 134423.

[251] Y. Cao and N. Wu, *Many-body localization in the random-field heisenberg chain with dzyaloshinskii-moriya interaction*, *Europhysics Letters* **141** (feb, 2023) 48001.

[252] E. Ising, *Beitrag zur theorie des ferromagnetismus*, *Zeitschrift für Physik* **31** (Feb, 1925) 253–258.

[253] L. Onsager, *Crystal statistics. i. a two-dimensional model with an order-disorder transition*, *Phys. Rev.* **65** (Feb, 1944) 117–149.

[254] D. Thouless, *Lower dimensionality and localization*, *Physica B+C* **109-110** (1982) 1523–1530. 16th International Conference on Low Temperature Physics, Part 3.

[255] E. J. Davis, B. Ye, F. Machado, S. A. Meynell, W. Wu, T. Mittiga, W. Schenken, M. Joos, B. Kobrin, Y. Lyu, Z. Wang, D. Bluvstein, S. Choi, C. Zu, A. C. B. Jayich, and N. Y. Yao, *Probing many-body dynamics in a two-dimensional dipolar spin ensemble*, *Nature Physics* **19** (Jun, 2023) 836–844.

[256] B. L. Dwyer, L. V. Rodgers, E. K. Urbach, D. Bluvstein, S. Sangtawesin, H. Zhou, Y. Nassab, M. Fitzpatrick, Z. Yuan, K. De Greve, E. L. Peterson, H. Knowles, T. Sumarac, J.-P. Chou, A. Gali, V. Dobrovitski, M. D. Lukin, and N. P. de Leon, *Probing spin dynamics on diamond surfaces using a single quantum sensor*, *PRX Quantum* **3** (Dec, 2022) 040328.

[257] A. Scheie, N. E. Sherman, M. Dupont, S. E. Nagler, M. B. Stone, G. E. Granroth, J. E. Moore, and D. A. Tennant, *Detection of kardar–parisi–zhang hydrodynamics in a quantum heisenberg spin-1/2 chain*, *Nature Physics* **17** (Jun, 2021) 726–730.

[258] S. A. Meynell, Y. M. Eggeler, J. D. Bocarsly, D. A. Kitchaev, B. E. Rhodes, T. M. Pollock, S. D. Wilson, A. Van der Ven, R. Seshadri, M. De Graef, A. B. Jayich, and D. S. Gianola, *Inducing skyrmion flop transitions in* $\mathrm{co_8zn_8mn_4}$ *at room temperature*, *Phys. Rev. Mater.* **7** (Apr, 2023) 044401.

[259] L. Guin, M. Jabbour, and N. Triantafyllidis, *Revisiting step instabilities on crystal surfaces. part i: The quasistatic approximation*, *Journal of the Mechanics and Physics of Solids* **156** (2021) 104574.

[260] L. Guin, M. Jabbour, L. Shaabani-Ardali, and N. Triantafyllidis, *Revisiting step instabilities on crystal surfaces. part ii: General theory*, *Journal of the Mechanics and Physics of Solids* **156** (2021) 104582.

[261] R. L. Schwoebel and E. J. Shipsey, *Step Motion on Crystal Surfaces*, *Journal of Applied Physics* **37** (06, 1966) 3682–3686, [https://pubs.aip.org/aip/jap/article-pdf/37/10/3682/7936850/3682_1_online.pdf].

[262] G. Ehrlich and F. G. Hudda, *Atomic View of Surface Self-Diffusion: Tungsten on Tungsten*, *The Journal of Chemical Physics* **44** (05, 1966) 1039–1049, [https://pubs.aip.org/aip/jcp/article-pdf/44/3/1039/11259582/1039_1_online.pdf].

[263] M. Xie, S. Leung, and S. Tong, *What causes step bunching––negative ehrlich–schwoebel barrier versus positive incorporation barrier*, *Surface Science* **515** (2002), no. 1 L459–L463.

[264] J. Tersoff, Y. H. Phang, Z. Zhang, and M. G. Lagally, *Step-bunching instability of vicinal surfaces under stress*, *Phys. Rev. Lett.* **75** (Oct, 1995) 2730–2733.

[265] T. Kimoto, A. Itoh, H. Matsunami, and T. Okano, *Step bunching mechanism in chemical vapor deposition of 6H– and 4H–SiC 0001*, *Journal of Applied Physics* **81** (04, 1997) 3494–3500, [https://pubs.aip.org/aip/jap/article-pdf/81/8/3494/10583906/3494_1_online.pdf].

[266] E. Rittweger, D. Wildanger, and S. W. Hell, *Far-field fluorescence nanoscopy of diamond color centers by ground state depletion*, *Europhysics Letters* **86** (apr, 2009) 14001.

[267] K. Y. Han, S. K. Kim, C. Eggeling, and S. W. Hell, *Metastable dark states enable ground state depletion microscopy of nitrogen vacancy centers in diamond with diffraction-unlimited resolution*, *Nano Letters* **10** (2010), no. 8 3199–3203, [https://doi.org/10.1021/nl102156m]. PMID: 20698637.

[268] B. Fortman and S. Takahashi, *Understanding the linewidth of the esr spectrum detected by a single nv center in diamond*, *The Journal of Physical Chemistry A* **123** (Jul, 2019) 6350–6355.

[269] O. R. Rubinas, V. V. Soshenko, S. V. Bolshedvorskii, I. S. Cojocaru, V. V. Vorobyov, V. N. Sorokin, V. G. Vins, A. P. Yeliseev, A. N. Smolyaninov, and A. V. Akimov, *Optimization of the double electron–electron resonance for c-centers in diamond*, *physica status solidi (RRL) – Rapid Research Letters* **16** (2022), no. 5 2100561, [https://onlinelibrary.wiley.com/doi/pdf/10.1002/pssr.202100561].

[270] G. Wang, C. Li, H. Tang, B. Li, F. Madonini, F. F. Alsallom, W. K. C. Sun, P. Peng, F. Villa, J. Li, and P. Cappellaro, *Manipulating solid-state spin concentration through charge transport*, *Proceedings of the National Academy of Sciences* **120** (2023), no. 32 e2305621120, [https://www.pnas.org/doi/pdf/10.1073/pnas.2305621120].

[271] C. Munuera-Javaloy, R. Puebla, B. D'Anjou, M. B. Plenio, and J. Casanova, *Detection of molecular transitions with nitrogen-vacancy centers and electron-spin labels*, *npj Quantum Information* **8** (Nov, 2022) 140.

[272] S. Li, H. Zheng, Z. Peng, M. Kamiya, T. Niki, V. Stepanov, A. Jarmola, Y. Shimizu, S. Takahashi, A. Wickenbrock, and D. Budker, *Determination of local defect density in diamond by double electron-electron resonance*, *Phys. Rev. B* **104** (Sep, 2021) 094307.

[273] X. Xiao and N. Zhao, *Proposal for observing dynamic jahn–teller effect by single solid-state defects*, *New Journal of Physics* **18** (Oct., 2016) 103022.

[274] F. de Theije, J. Schermer, and W. van Enckevort, *Effects of nitrogen impurities on the cvd growth of diamond: step bunching in theory and experiment*, *Diamond and Related Materials* **9** (2000), no. 8 1439–1449.

[275] M. Krishnamurthy, D. R. M. Williams, and P. M. Petroff, *Dynamics of periodic step-bunching during growth on vicinal gaas(110) surfaces: Computer simulations and experiments*, *MRS Online Proceedings Library* **312** (Dec, 1993) 327–332.

[276] E. Robin, N. Mollard, K. Guilloy, N. Pauc, P. Gentile, Z. Fang, B. Daudin, L. Amichi, P.-H. Jouneau, C. Bougerol, M. Delalande, and A.-L. Bavencove, *Quantification of dopants in nanomaterial by SEM/EDS*, pp. 380–381. John Wiley & Sons, Ltd, 2016. https://onlinelibrary.wiley.com/doi/pdf/10.1002/9783527808465.EMC2016.6335.

[277] K. Fukunaga, N. Endo, M. Suzuki, and Y. Kondo, *Concentration at Detection Limit of Dopant for Semiconductor Samples Using Dual SDD Analysis System*, *Microscopy and Microanalysis* **21** (09, 2015) 823–824, [https://academic.oup.com/mam/article-pdf/21/S3/823/48334691/mam0823.pdf].

[278] S. Takahashi, R. Hanson, J. van Tol, M. S. Sherwin, and D. D. Awschalom, *Quenching spin decoherence in diamond through spin bath polarization*, *Phys. Rev. Lett.* **101** (Jul, 2008) 047601.

[279] A. Jarmola, V. M. Acosta, K. Jensen, S. Chemerisov, and D. Budker, *Temperature- and magnetic-field-dependent longitudinal spin relaxation in nitrogen-vacancy ensembles in diamond*, *Phys. Rev. Lett.* **108** (May, 2012) 197601.

[280] J. von Neumann and R. T. BEYER, *Mathematical Foundations of Quantum Mechanics: New Edition*. Princeton University Press, ned - new edition ed., 2018, 1927.